Title
In Vivo Quantification of Cardiac Microstructure with Convex Optimized Diffusion Weighted MRI

Author
Aliotta, Eric

Publication Date
2017

Peer reviewed|Thesis/dissertation

UNIVERSITY OF CALIFORNIA

Los Angeles

In Vivo Quantification of Cardiac Microstructure with Convex Optimized Diffusion Weighted MRI

A dissertation submitted in partial satisfaction of the requirements for the degree Doctor of Philosophy in Biomedical Physics

by

Eric Aliotta

2017

ABSTRACT OF THE DISSERTATION

In Vivo Quantification of Cardiac Microstructure with Convex Optimized Diffusion Weighted MRI

by

Eric Aliotta

Doctor of Philosophy in Biomedical Physics

University of California, Los Angeles, 2017

Professor Daniel B. Ennis, Chair

Diffusion weighted imaging (DWI) is a powerful quantitative magnetic resonance imaging (MRI) technique that can probe tissues *in vivo* at the microscopic level and provide insight into cellular microstructural environment. Cardiac DWI has great potential value in its ability to answer open questions regarding myocardial structure, dynamics, and remodeling. Unfortunately, several technical limitations of current DWI techniques make its application in the beating heart very challenging, which leads to erroneous or inconsistent results. Amongst the challenges are an extreme sensitivity to bulk physiological motion, low signal to noise ratios (SNR), long scan times, and geometric image distortions. In this dissertation, these limitations are addressed with novel technical developments applied to the DWI pulse sequence including convex optimized diffusion gradient waveform design and multi-parametric tissue characterization.

A brief introduction to Nuclear Magnetic Resonance (NMR) and MRI is provided in Chapter 1. This leads into a description of the fundamental components of a DWI acquisition in Chapter 2 and an overview of the current state of cardiac DWI in Chapter 3.

In Chapter 4, a novel DWI strategy called Convex Optimized Diffusion Encoding (CODE) is described. CODE is a mathematical framework that formulates diffusion encoding gradient design as a convex optimization problem and automatically generates motion compensated (MOCO) waveforms that achieve the shortest possible echo times (TE) and thus improve SNR. First and second order moment nulled CODE (CODE-M_1M_2) permits DWI that is robust to cardiac motion with higher SNR than an existing MOCO technique. First order motion compensated CODE-M_1 also improves robustness to cardiac induced motion in liver DWI with higher SNR than M_1 nulled bipolar DWI. CODE can also be used for non-motion compensated DWI and improves SNR compared with traditional monopolar DWI in the brain.

In Chapter 5 we present a multi-parametric DWI strategy that simultaneously yields maps of the apparent diffusion coefficient (ADC) and T_2 relaxation time constant in the heart (T_2+ADC). Typically, DWI protocols include multiple acquisitions with a range of diffusion encoding strengths (b-value), but with constant TE to isolate the effect of diffusion of the signal. The joint T_2+ADC approach varies both b-value and TE within the acquisition to facilitate estimation of both ADC and T_2 relaxation. T_2+ADC permits joint reconstruction with no increase in scan time compared with DWI alone and no effect on ADC measurement.

In Chapter 6 we use CODE-M_1M_2 diffusion encoding to perform cardiac diffusion tensor imaging (cDTI) and generate maps of myocardial microstructure in healthy volunteers. cDTI can be used to map myocardial fiber and myolaminar sheetlet orientations, which can contribute to our understanding of ventricular microstructure in health and disease and facilitate sophisticated mechanical models of cardiac dynamics. However, it is important to understand the uncertainty underlying these measurements to inform interpretation and define acquisition limitations. We

apply a previously described bootstrap technique to measure the uncertainty in the diffusion tensors derived from CODE-M_1M_2 cDTI and establish achievable levels of precision in clinically feasible scan times.

In Chapter 7 the CODE framework is extended to compensate for the effect of eddy currents, which are a common cause of image distortions in DWI and DTI. Diffusion encoding gradients must be very strong to encode microscopic molecular displacements and these strong gradient pulses induce unwanted eddy currents in conductive MRI hardware components. If not addressed, eddy currents lead to distorted images and corrupted diffusion parameter estimates. We incorporate an eddy current model into the CODE optimization framework to develop eddy current nulled CODE (EN-CODE). EN-CODE accomplishes eddy current nulling with TEs that are comparable to traditional monopolar encoding and much shorter than the established twice refocused spin echo (TRSE) technique for eddy current nulling.

The developments described in this dissertation represent an improvement in the flexibility, efficiency, and robustness of diffusion encoding. The CODE framework can also be easily modified to address additional constraints and thus may prove useful in currently unforeseen applications.

The dissertation of Eric Aliotta is approved.

Peng Hu

Holden H. Wu

Alan Garfinkel

Daniel B. Ennis, Committee Chair

University of California, Los Angeles

2017

For Mom and Dad

CONTENTS

LIST OF FIGURES

LIST OF TABLES

ACKNOWLEDGEMENTS

The work described in this dissertation barely begins to describe all that I have learned from Daniel Ennis, who has been the best mentor that I could have possibly hoped for. Dan is a truly talented teacher and I will forever be thankful for his encouragement and enthusiasm every step of the way.

I would also like to thank all of the members of my committee: Peng Hu, Holden Wu, Alan Garfinkel, and Olujimi Ajijola, who have been a pleasure to work with and have been extremely generous with their expertise and unique perspectives.

Special thanks to Patrick, Kévin, Luigi, Mike, Jessica, Ilya, Stephanie, and the rest of the lab. Working with such a great group of people every day has truly made the years fly by. Our occasional treks to Southeast Asia or up mountains in the Sierras certainly didn't hurt either!

Thank you to Michael McNitt-Gray, Reth Thatch Im, Terry Moore, my fellow graduate students, and the rest of the Biomedical Physics family who have made my time at UCLA a blast.

Huge thank you to my mother, Randi, father, Tom, and sister, Jackie for their constant love and support over all of these years and who made me into the person I am today.

And finally, thank you to Michelle Kew, who is there for me no matter what. Thank you for your love and friendship and for putting up with my "quick" trip to California to get a PhD!

VITA

2012 BS Physics, University of Virginia, Charlottesville, VA

2015 MS Biomedical Physics, University of California, Los Angeles, CA

Peer Reviewed Publications

1. **Aliotta E**, Moulin K, Ennis DB. Eddy Current Nulled Convex Optimized Diffusion Encoding (EN-CODE) for Distortion Free Diffusion Tensor Imaging with Short Echo Times. Magnetic Resonance in Medicine. 2017; doi: 10.1002/mrm.26709.
2. **Aliotta E**, Moulin K, Zhang Z, Ennis DB. Simultaneous Measurement of T_2 and Apparent Diffusion Coefficient (T_2+ADC) in the Heart with Motion Compensated Spin Echo Diffusion Weighted Imaging. Magnetic Resonance in Medicine. 2017; doi: 10.1002/mrm.26705.
3. **Aliotta E**, Wu H, Ennis DB. Convex Optimized Diffusion Encoding (CODE) Gradient Waveforms for Minimum Echo Time and Bulk Motion Compensated Diffusion Weighted MRI. Magnetic Resonance in Medicine. 2017; 77: 717–729.
4. Ajijola O, Lux R, Khahera A, Kwon O, **Aliotta E**, Ennis DB, Fishbein M, Ardell J, Shivkumar K. Sympathetic Modulation of Electrical Activation In Normal and Infarcted Myocardium: Implications for Arrhythmogenesis. American Journal of Physiology-Heart and Circulatory Physiology. 2017; 312(3):H608-H621
5. Nielles-Vallespin S, Ferreira P, de Sivla R, Scott AD, Kilner P, McGill LA, Giannakidis A, Gatehouse PD, Ennis DB, **Aliotta E**, Mazilu D, Kellman P, Al-Khalil M, Balaban R, Firmin D, Arai A, Pennell D. Evaluation of microstructural dynamics underlying myocardial wall thickening in-vivo by diffusion tensor cardiac magnetic resonance: validation and clinical translation in human dilated cardiomyopathy. Journal of the American College of Cardiology. 2017; 69(6):661-676.
6. Nakamura K, Ajijola O, **Aliotta E**, Armour JA, Ardell JL, Shivkumar K. Pathological Effects of Chronic Myocardial Infarction on Peripheral Neurons Mediating Cardiac Neurotransmission. Autonomic Neuroscience: Basic and Clinical. 2016; 197:34-40.

7. Wijesooriya K, **Aliotta E,** Benedict S, Read P, Rich T, Larner J. RapidArc patient specific mechanical delivery accuracy under extreme mechanical limits using Linac log files. Medical Physics. 2012; 39(4):1846-53.

Peer Reviewed Conference Papers

1. Perotti L, Magrath R, Verzhbinsky I, **Aliotta E**, Moulin K, Ennis DB. *Microstructurally Anchored Cardiac Kinematics by Combining In Vivo DENSE MRI and cDTI.* Proceedings of the FIMH Conference. Toronto, ON, CA. 2017.

Patents

2. **Aliotta E**, Wu H, Ennis DB. Convex Optimized Diffusion Encoding (CODE) Gradient Waveforms for Minimum Echo Time and Bulk Motion Compensated Diffusion Weighted MRI. Disclosed: 09/20/2015, Provisional Filing: 01/25/2016 (#62/286,483)
3. **Aliotta E** and Ennis DB. Simultaneous Estimation of T_2 Relaxation and Apparent Diffusion Coefficient Maps with Magnetic Resonance Imaging. Disclosed: 09/04/2014, Provisional Filing: 01/28/2015 (#62/108,993)
4. **Aliotta E**, Moulin K and Ennis DB. *System and Method for Optimized Diffusion Weighted Imaging Without Eddy Currents.* Disclosed: 12/04/2016, Provisional Filing: 03/01/2017 (#62/465,517)

THESIS MOTIVATION

Diffusion weighted magnetic resonance imaging (DWI) is a powerful quantitative imaging technique that non-invasively probes the microstructure underlying biological tissues by measuring the diffusive mobility of water [1, 2]. For example, DWI is well established as a tool for the early detection of acute strokes because it is sensitive to local decreases in diffusivity that precede other detectable changes [3]. DWI is also a common oncological imaging technique because of its sensitivity to decreases in diffusivity that accompany increases in cellular density within malignant tumors [4]. Diffusion tensor imaging (DTI), an extension of DWI that can capture microstructural anisotropy and directionality, has also proven useful for improving our understanding of the structure of the brain in health and disease and by mapping the complex network of neuronal fibers [5].

In principle, cardiac DWI (cDWI) could provide substantially novel insight to cardiac microstructure and changes to microstructure in health and disease. For example, cDWI has potential value in its ability to detect myocardial infarction (MI) without the need for an injected contrast agent [6-8]. This could potentially enable detailed infarct characterization in patients who are precluded from contrast injections due to limited renal function a group that makes up nearly 1% of the adult population in the United States [9-13]. Furthermore, cardiac DTI (cDTI)

has demonstrated sensitivity to changes in cardiac microstructural organization that occur in hypertrophic and dilated cardiomyopathies [14-16]. Unfortunately, numerous challenges still exist in cDWI and cDTI that can confound measurement and have limited clinical adoption.

Unfortunately, the large gradients that are used to encode the diffusive motion of water molecules also make DWI highly sensitive to bulk physiological motion. This can lead to severe signal corruption when imaging the heart. One proposed solution is the use of motion compensated diffusion encoding gradient waveforms with nulled first (M_1) and second (M_2) order moments. Gradient waveforms designed with these constraints have no net effect on spins moving with linear velocities and accelerations during the diffusion encoding interval, thereby enabling diffusion encoding in the presence of cardiac motion [17-19]. Gradient moment nulling, however, necessarily increases the total diffusion encoding duration as compared to non-motion compensated waveforms. Consequently, conferring bulk motion insensitivity unavoidably increases the echo time (TE), which reduces signal to noise ratios (SNR).

This dissertation describes a novel approach called Convex Optimized Diffusion Encoding (CODE) [20]. CODE is a framework that automatically generates time-optimal diffusion encoding gradient waveforms subject to hardware constraints, pulse sequence timing constraints and gradient moment (i.e. motion compensation) constraints. Notably, CODE enables motion compensated diffusion encoding for cDWI with substantially shorter TEs (and thus higher SNR) than existing techniques. CODE enables robust mapping of myocardial ADC and local cardiomyocyte orientations and also facilitates a novel multi-parametric T_2 and ADC mapping strategy. The CODE framework has several applications and herein it will be shown that CODE also permits improvements in DWI of the brain and liver.

The ***objective*** of this dissertation was to develop and evaluate optimized cardiac DWI acquisition strategies and explore applications outside of the heart. The ***specific aims*** were to: 1) Develop convex optimized diffusion encoding (CODE) for robust DWI in the heart and explore

applications in the brain and liver (Chapter 4); 2) Demonstrate multi parametric T_2+ADC mapping in the heart using CODE cDWI (Chapter 5); 3) Acquire in vivo maps of cardiac microstructure using CODE cDTI and quantify the precision of the technique (Chapter 6); and 4) Modify the CODE framework to mitigate eddy current induced image distortions in DWI while maintaining temporal efficiency (Chapter 7).

SPECIFIC AIM #1 — *Develop the Convex Optimized Diffusion Encoding (CODE) framework for time-efficient and motion compensated DWI.* Most diffusion encoding gradient waveforms in spin echo EPI DWI are symmetric about the refocusing RF pulse, which simplifies design, but leads to inefficient dead-times within the pulse sequence and extends TE. This effect is amplified in multi-polar motion compensated gradient designs with nulled first and/or second order moments (M_1 and M_2). We ***hypothesized*** that we could remove all sequence dead time and shorten TEs by employing a convex optimized diffusion encoding gradient waveform design. In Chapter 4 we demonstrate through simulations, phantom imaging, and in vivo imaging that CODE can shorten TE and improve SNR in DWI of the brain, M_1 nulled DWI of the liver and M_1M_2 nulled DWI of the heart.

SPECIFIC AIM #2 — *Demonstrate a technique for multi-parametric T_2+ADC mapping in the heart using CODE cDWI.* ADC mapping has potential value in its ability to detect myocardial fibrosis without contrast injections and quantitative T_2 mapping can provide additional sensitivity to regions of edema (inflammation). While these techniques traditionally require two separate acquisitions, we ***hypothesized*** that quantitative T_2 maps can be extracted from a DWI acquisition by simply shifting the TE between measurements. In Chapter 5 we demonstrate through simulations, phantom imaging, and in vivo imaging that T_2+ADC mapping can accurately measure both parameters with no increase in scan time compared with DWI alone.

SPECIFIC AIM #3 — *Quantify the in vivo precision of cardiac microstructural maps using CODE cDTI.* cDTI provides a wealth of information regarding the microstructural organization of the myocardium and has promise in both clinical diagnosis and in improving our basic understanding of the heart. However, cDTI remains a challenging and low SNR technique and the achievable measurement precision is largely unknown. We ***hypothesized*** that a previously described bootstrapped method for measuring diffusion tensor uncertainty can be adapted and extended to quantify the overall precision of diffusion tensors derived parameters measured using in vivo cDTI with reasonable scan durations. In Chapter 6 we quantify the diffusion tensor uncertainty for CODE cDTI obtained in healthy volunteers and demonstrate that an acceptable degree of uncertainty can be achieved in five minute free breathing.

SPECIFIC AIM #4 — *Demonstrate eddy current nulled CODE for DTI with reduced image distortions.* The large diffusion encoding gradients required to sensitize the MRI signal to the diffusive motion also induce unwanted eddy currents in the MRI hardware that can distort images and confound reconstruction. Eddy currents can be nulled by using a twice refocused spin echo (TRSE) DWI pulse sequence, but this requires longer TEs and thus reduces SNR. We ***hypothesized*** that we could adapt the CODE framework to compensate for diffusion encoding gradient induced eddy currents, but with shorter TEs than TRSE. In Chapter 7 we demonstrate that eddy current nulled CODE (EN-CODE) virtually eliminates eddy current induced image distortions in phantoms and in vivo neuro DTI with shorter TEs than TRSE and monopolar DWI in most cases.

The developments described in these specific aims represent an improvement on the efficiency and robustness of diffusion weighted imaging with specific emphasis on implications for cardiac imaging. This work will facilitate the clinical translation of cDWI for the evaluation of myocardial infarcts in patients who cannot receive contrast injections and improve the capabilities of microstructural myofiber mapping in the beating heart. These developments will

also translate to improvements in motion robustness, SNR, and image distortion in DWI outside of the heart in organs such as the brain and liver.

1 Introduction to Magnetic Resonance Imaging

Proposed in 1973 [21] and brought to clinical practice in 1980 [22], magnetic resonance imaging (MRI) is a non-invasive medical imaging technique that utilizes the electromagnetic properties of water molecules in soft tissue to generate images of the human anatomy. MRI employs the phenomenon of nuclear magnetic resonance (NMR) to generate contrast between different tissues without the need for harmful ionizing radiation. This chapter will introduce several fundamental principles in MRI including signal generation, spatial localization, signal detection, and image reconstruction.

1.1 Nuclear Magnetic Resonance

Nuclei containing an odd number of protons and/or neutrons possess nuclear *spin* that, in turn produces a net *angular momentum*, $\vec{J}$. Because the nucleus also possesses a non-zero electric charge, this leads to a *magnetic moment*, $\vec{\mu}$ that is empirically described by: $\vec{\mu} = \gamma\vec{J}$, where γ is the *gyromagnetic ratio* and is unique to any particular isotope. The magnetic moment becomes useful when a large magnetic field ($\vec{B}$) is applied to the system, which causes magnetic moments to align preferentially along the direction of the field. In the presence of $\vec{B}$, the Zeeman effect [23] leads to two energetically favorable states: $\vec{\mu}$ aligned parallel to $\vec{B}$, denoted “spin up,”

the lowest energy state; and $\vec{\mu}$ aligned anti-parallel to $\vec{B}$, "spin down", a state with slightly higher energy. The energy difference between these states is given by:

$$\mathbf{\Delta E = \gamma h B_0} \tag{1.1}$$

Where h is Planck's constant (6.63×10^{-34} J•s) [24] and B_0 is the magnitude of $\vec{B}$. Thermodynamics dictates that the lower energy state results in a larger number of spins occupying the "spin up" ($N_\uparrow$) than "spin down" state ($N_\downarrow$) according to the Boltzmann relationship [25]:

$$\mathbf{\frac{N_\uparrow}{N_\downarrow} = exp\left(\frac{\Delta E}{KT}\right) = exp\left(\frac{\gamma h B_0}{KT}\right)} \tag{1.2}$$

Where K is Boltzmann's constant (1.38×10^{-23} J/Kelvin) and T is the system temperature (in Kelvin). A rough calculation [26] can show that in a 3.0T magnetic field at room temperature (300K), $N_\uparrow$ exceeds $N_\downarrow$ by approximately 9 parts per million (ppm). Fortunately, this small disparity is enough to generate a detectable NMR signal.

A fundamental concept in NMR is *excitation,* which describes the absorption of a photon with energy ΔE into the system that causes a spin to "jump" from the "spin up" state to the "spin down" state. The frequency of this photon can be determined using the Einstein-Planck relation [27]:

$$\mathbf{E = hf} \tag{1.3}$$

By combining equations 1.1 and 1.3, the resonant frequency, or *Larmor frequency*, f_0 of a system can be defined:

$$\mathbf{f_0 = \frac{\gamma}{2\pi} B_0} \tag{1.4}$$

The hydrogen nucleus (^{1}H) that exists in water molecules and makes up the majority of tissues in the human body has a gyromagnetic ratio, $\gamma/2\pi$ = 42.576 MHz/T. This results in a Larmor

frequency f_0=63.87MHz in a 1.5T magnetic field and 127.74MHz at 3.0T, the field strengths most commonly used in modern MRI. This is significant because photons at these frequencies have energies $<10^{-8}$ eV which is far below the threshold for *ionizing radiation*, which occurs at energies approximately >30eV and can free electrons from atomic orbitals and cause cancer. This comes in contrast to imaging modalities such as X-ray, computed tomography (CT) and positron emission tomography (PET), which rely on ionizing radiation to generate images and thus must be used sparingly to limit health risks.

If one considers an ensemble of N ^{1}H nuclei initially in the "spin up" configuration in a field, $\mathbf{B_0}$ oriented along the longitudinal axis (i.e. z direction), there will be a net ensemble magnetic moment, referred to as the *bulk magnetization,* described by:

$$\vec{\mathbf{M}} = \sum_{i=1}^{N} \vec{\boldsymbol{\mu}}_{\mathbf{i}} \qquad 1.5$$

When the magnetic moments of all N spins are oriented along z, this vector quantity adds constructively ($\vec{\mathrm{M}} = N\,\vec{\mu}$). However, if a radio frequency (RF) excitation pulse tuned to a frequency f_0 is applied, a portion of the magnetic moments will "flip" to the spin down energy state, which leads to destructive interference and a change in the bulk magnetization vector. Over time, the moments will revert back to the energetically favorable "spin up" state, which causes $\vec{\mathrm{M}}$ to approach its initial value in a process referred to as *relaxation,* which will be discussed further in the next section. The rate of relaxation is dependent on the molecular environment surrounding a given set of molecules and thus varies between different tissues in the human body. These subtle differences are exploited in MRI to generate differences in signal strength (i.e. *contrast*) between organs.

1.2 Bloch Equations

The temporal behavior of the bulk magnetization vector in the presence of an applied magnetic field can be described by the generalized *Bloch Equation*:

$$\frac{\mathbf{d}\vec{\mathbf{M}}}{\mathbf{dt}} = \boldsymbol{\gamma}\vec{\mathbf{M}}\,\mathbf{x}\,\vec{\mathbf{B}} - \frac{\mathbf{M_x}\vec{\mathbf{i}} + \mathbf{M_y}\vec{\mathbf{j}}}{\mathbf{T_2}} - \frac{(\mathbf{M_z} + \mathbf{M_z^0})\vec{\mathbf{k}}}{\mathbf{T_1}} \qquad 1.6$$

where M_x, M_y and M_z are components of the bulk magnetization vector, $M_z^0\vec{k}$ is the thermal equilibrium state of M, and $\vec{i}$, $\vec{j}$, and $\vec{k}$ are unit vectors along the x, y, and z directions, respectively. This vector equation can be written in terms of its three directional components:

$$\frac{\mathbf{dM_x}}{\mathbf{dt}} = \boldsymbol{\gamma}\left(\mathbf{M_y B_z} - \mathbf{M_z B_y}\right) - \frac{\mathbf{1}}{\mathbf{T_2}}\mathbf{M_x}$$

$$\frac{\mathbf{dM_y}}{\mathbf{dt}} = \boldsymbol{\gamma}\left(\mathbf{M_z B_x} - \mathbf{M_z B_y}\right) - \frac{\mathbf{1}}{\mathbf{T_2}}\mathbf{M_y}$$

$$\frac{\mathbf{dM_z}}{\mathbf{dt}} = \boldsymbol{\gamma}\left(\mathbf{M_x B_y} - \mathbf{M_y B_x}\right) - \frac{\mathbf{1}}{\mathbf{T_1}}(\mathbf{M_z} - \mathbf{M_0}) \qquad 1.7$$

These ordinary differential equations can be used to describe two processes: *precession* (the first terms of 1.7) and *relaxation* (the second terms of 1.7). Precession describes the rotation of the bulk magnetization about the z-axis at the Larmor frequency and can take two forms: *free precession* in the presence of the B_0 field only and *forced precession* in the presence of an excitation RF pulse. *Relaxation* describes the temporal behavior of the system after excitation as it returns to its initial state.

1.2.1 Free Precession

Let us first consider the behavior of the magnetization vector in a static field, $\vec{B} = B_0\vec{k}$ and ignore the effect of relaxation (i.e. only consider the first terms of the equations in 1.7). The Bloch equations now take the form:

$$\frac{\mathbf{dM_x}}{\mathbf{dt}} = \boldsymbol{\gamma \mathbf{M_y B_0}}$$

$$\frac{\mathbf{dM_y}}{\mathbf{dt}} = -\boldsymbol{\gamma \mathbf{M_x B_0}}$$

$$\frac{\mathbf{dM_z}}{\mathbf{dt}} = \mathbf{0} \qquad 1.8$$

If we consider an initial condition with longitudinal magnetization and transverse magnetization oriented in the x direction, $\vec{M}_0 = M_{xy,0}\vec{i} + M_{z,0}\vec{k}$, a closed form solution to this system of equations can be easily determined:

$$\mathbf{M}_x(\mathbf{t}) = \mathbf{M}_{xy,0}\mathbf{cos}(\boldsymbol{\gamma \mathbf{B_0 t}})$$

$$\mathbf{M}_y(\mathbf{t}) = \mathbf{M}_{xy,0}\mathbf{sin}(\boldsymbol{\gamma \mathbf{B_0 t}})$$

$$\mathbf{M}_z(\mathbf{t}) = \mathbf{M}_{z,0} \qquad 1.9$$

Thus, in the absence of relaxation, there is no temporal change to the longitudinal magnetization. However, the transverse magnetization rotates about the z-axis with frequency $\omega_0=\gamma B_0$. This rotation describes the process of *free precession*.

1.2.2 Forced Precession

The spin system can be excited through the use of an RF excitation pulse in the form of an additional, time-varying magnetic field, $\vec{B}_1$. In MRI experiments, $\vec{B}_1$ is tuned to oscillate with a *carrier frequency* $\omega_0 = 2\pi f_0$ (Eqn. 1.4) perpendicular to $\vec{B}_0$ (i.e. circularly polarized in the x-y

plane). It is worth noting that the magnitude of $\vec{B}_1$ is substantially lower than that of $\vec{B}_0$ (B_1 is typically ≤25μT whereas B_0 is typically 1.5-3.0T). In addition to oscillating with the carrier frequency, RF pulses are defined by an *envelope function*, B_1^e that defines its overall temporal modulation (i.e. shape). This shape, when combined with concurrent magnetic field *gradients* (which will be discussed in 1.3) can create a spatially dependent excitation profile, which is critical for imaging experiments.

In order to describe the behavior of $\vec{M}$ during excitation, it is useful to define the *rotating frame of reference* which rotates clockwise with an angular frequency defined by the Larmor frequency of the B_0 field, $\omega_0 = \gamma B_0$ (Eqn. 1.4). This is mathematically convenient because in this coordinate frame, the effective magnetic field experienced by an on-resonance spin (i.e. one precessing at angular frequency ω_0) is given by:

$$\vec{\mathbf{B}}_{\mathbf{eff}} = \vec{\mathbf{B}} - \frac{\boldsymbol{\omega_0}}{\boldsymbol{\gamma}}\vec{\mathbf{k}} \tag{1.10}$$

The B_0 field ($\vec{B} = B_0\vec{k}$) thus reduces to:

$$\vec{\mathbf{B}}_{\mathbf{eff,0}} = \mathbf{B_0}\vec{\mathbf{k}} - \frac{\boldsymbol{\omega_0}}{\boldsymbol{\gamma}}\vec{\mathbf{k}} = \mathbf{B_0}\vec{\mathbf{k}} - \mathbf{B_0}\vec{\mathbf{k}} = \mathbf{0} \tag{1.11}$$

This means that in the rotating frame, the B_0 field has no net effect on the magnetization. Similarly, the B_1 component of the field reduces to a simpler form in the rotating frame, if the carrier frequency is chosen to be ω_0:

$$\vec{\mathbf{B}}_{\mathbf{eff,1}} = \mathbf{B_1^e(t)e^{-i\varphi}} \tag{1.12}$$

Where φ is the phase of the RF pulse. If we assume φ=0, this reduces further to:

$$\vec{\mathbf{B}}_{\mathbf{eff,1}} = \mathbf{B_1^e(t)}\vec{\boldsymbol{\imath}} \tag{1.13}$$

We can now return to the Bloch equations to explore how the magnetization progresses during excitation. This can be simplified if we ignore the effects of relaxation (which will be discussed in 1.2.3). Note that this is a reasonable approximation provided the RF pulse duration, τ_{RF} is short with respect to T_1 and T_2 (typically τ_{RF}<5ms whereas T_1>200ms and T_2>20ms). In this case, Eqn. 1.6 becomes:

$$\frac{\mathbf{d}\vec{\mathbf{M}}}{\mathbf{dt}} = \boldsymbol{\gamma}\vec{\mathbf{M}}\,\mathbf{x}\,\mathbf{B}_1^{\mathbf{e}}(\mathbf{t})\vec{\boldsymbol{\imath}} \tag{1.14}$$

Note that here $\vec{\mathrm{M}}$ represents the magnetization vector in the rotating frame of reference (which will be implied for the remainder of this section). If we assume the initial configuration: $\vec{\mathrm{M}}_0 = \mathrm{M}_z^0\vec{\mathrm{k}}$, the following solution can be reached:

$$\vec{\mathbf{M}}(\mathbf{t}) = \mathbf{M}_\mathbf{z}^\mathbf{0}\mathbf{sin}\left(\boldsymbol{\gamma}\int_0^{\boldsymbol{\tau_{RF}}}\mathbf{B}_1^{\mathbf{e}}(\mathbf{t})\boldsymbol{dt}\right)\vec{\boldsymbol{j}} + \mathbf{M}_\mathbf{z}^\mathbf{0}\mathbf{cos}\left(\boldsymbol{\gamma}\int_0^{\boldsymbol{\tau_{RF}}}\mathbf{B}_1^{\mathbf{e}}(\mathbf{t})\boldsymbol{dt}\right)\vec{\boldsymbol{k}} \tag{1.15}$$

This behavior shows that in the rotating frame of reference, excitation manifests as a rotation of the magnetization vector. Note that the axis of rotation is determined by the phase of the RF pulse. Because the phase φ=0 was chosen for this example, the rotation occurs about the x-axis leading to a temporally increasing y component of the magnetization and a temporally decreasing z-component. It is convenient to describe this rotation by defining the *flip angle* of the RF pulse, α:

$$\boldsymbol{\alpha} = \boldsymbol{\gamma}\int_0^{\boldsymbol{\tau_{RF}}}\mathbf{B}_1^{\mathbf{e}}(\mathbf{t})\boldsymbol{dt} \tag{1.16}$$

Thus, after the completion of the RF pulse (in the absence of relaxation effects), the magnetization can be described by:

$$\begin{aligned}\mathbf{M}_{\boldsymbol{xy}}(\mathbf{t}) &= \mathbf{M}_\mathbf{z}^\mathbf{0}\mathbf{sin}(\boldsymbol{\alpha})\\ \mathbf{M}_{\boldsymbol{z}}(\mathbf{t}) &= \mathbf{M}_\mathbf{z}^\mathbf{0}\mathbf{cos}(\boldsymbol{\alpha})\end{aligned} \tag{1.17}$$

Where M_{xy} is the magnitude of both the x and y components of $\vec{M}$ and is typically referred to as the *transverse magnetization*. M_{xy} represents the available signal that can be measured in an MRI experiment because RF receivers are generally tuned to measure any on-resonance magnetization polarized perpendicular to the B_0 field. Note that absent an excitation pulse (i.e. α=0), there is no transverse magnetization and thus no available signal.

Equations **1.16** and **1.17** provide a compact description of the net effect of an arbitrary RF pulse. Two commonly used RF pulse types are *saturation pulses* where α=90° and *inversion pulses* where α=180°. Saturation pulses rotate the magnetization entirely into the transverse plane whereas inversion pulses flip the magnetization to the –z orientation. While low and intermediate flip angles make less transverse signal available, they are often also useful for facilitating rapid data acquisition [28, 29].

1.2.3 Relaxation

The second terms in the equations in 1.7 represent the return of the bulk magnetization vector to its initial state over time in a process called *relaxation*. Relaxation can be divided into two distinct processes: spin-lattice, or T_1 relaxation, and spin-spin, or T_2 relaxation.

T_1 relaxation describes the recovery of the longitudinal magnetization from some excited state back to its initial, equilibrium state. This occurs via a dispersion of thermal energy from the excited spin to the surrounding molecular lattice as it returns to the equilibrium condition. The temporal behavior of M_z according to T_1 relaxation can be described by the following equation:

$$\mathbf{M_z(t) = M_0(1 - e^{-\frac{t}{T1}}) - M_z^0 e^{-\frac{t}{T1}}} \quad 1.18$$

Following a saturation pulse (i.e. M_z=0 directly after the pulse), this becomes:

$$\mathbf{M_z(t) = M_0(1 - e^{-\frac{t}{T1}})} \quad 1.19$$

From equation 1.19, it can be seen that the time T_1 represents the amount of time needed for a spin with initial M_z=0 to recover to 1-1/e (or approximately 63%) of its equilibrium M_z. Similarly, following an inversion pulse (i.e. M_z=-M_0 directly after the pulse, also referred to as a *refocusing* pulse), this becomes:

$$\mathbf{M_z(t) = M_0(1 - 2e^{-\frac{t}{T1}})} \quad 1.20$$

T_2 relaxation describes the decay of the transverse magnetization of an excited system to its equilibrium value of zero. This occurs when independent spins in the system *dephase*, or lose directional coherence, which causes a decay of the magnitude of the transverse magnetization. Dephasing occurs when spins encounter sources of "off-resonance" that cause them to precess at different frequencies. Off-resonance can arise from two main sources: 1) variability in the field itself, ΔB_{field} which can stem from system imperfections or from the presence of field-distorting materials (e.g. air pockets or metallic implants); and 2) interactions with other nearby charged particles in the local molecular environment, ΔB_{mol}. The overall signal decay due to both ΔB_{field} and ΔB_{mol} is referred to as T_2* decay and obeys the following decay model:

$$\mathbf{M_{xy}(t) = M_{xy}^0 e^{-\frac{t}{T2*}}} \quad 1.21$$

Where:

$$\mathbf{\frac{1}{T_2^*} = \frac{1}{T_2} + \frac{1}{T_{field}}} \quad 1.22$$

Here T_2 and T_{field} represent the time constants of signal decay due to ΔB_{mol} and ΔB_{field}, respectively. Note that T_2* describes the decay caused by both off-resonance sources and is always shorter than T_2.

While the signal decay due to ΔB_{mol} (i.e. T_2* decay) is irreversible, the effect of ΔB_{field} can be removed by applying a refocusing pulse to the system by generating a *spin echo,* which will now be briefly described. The phase generated by ΔB_{field} after a time $t=t_a$ can be described by $\varphi_{field}=\gamma\Delta B_{field}t_a$. After the application of a refocusing pulse, this phase is inverted: $\varphi_{ref}=-\gamma\Delta B_{field}t_a$. After an equivalent interval t_a, the system will gain an additional, $\varphi_{field}=\gamma\Delta B_{field}t_a$ which leads to a final phase $\varphi_{final}= \varphi_{sys}+ \varphi_{ref}=0$ at time $t=2t_a$. This increase (relative to t<2a) in signal at $t=2t_a$ is referred to as the spin echo and the final time is known as the *echo time* (TE) where $TE=2t_a$. As a result, the signal decay observed at TE is governed only by ΔB_{mol} and thus T_2 (not T2*) decay:

$$\mathbf{M_{xy}(TE)} = \mathbf{M_{xy}^0 e^{-\frac{TE}{T2}}} \quad 1.23$$

Typically, a spin echo experiment involves a saturation pulse followed by the aforementioned refocusing pulse. In this case, equations **1.19** and **1.22** can be combined to produce the following signal equation:

$$\mathbf{M_{xy}(TE, TR)} = \mathbf{M_0(1 - e^{-\frac{TR}{T1}}) e^{-\frac{TE}{T2}}} \quad 1.24$$

Where TR is the repetition time of the pulse sequence, which represents the time between excitation pulses in a series of spin echo experiments (multiple echoes are generally required to generate an image, as will be discussed in 1.3.5).

Relaxation plays a key role in generating useful anatomical images with MRI. Different tissues within the human body have different T_1 and T_2 values which leads to signal differences and thus *contrast* between regions. For example, at 3.0T, myocardial tissue typically has a T_1~1200ms and a T_2~40ms [30] whereas blood has a T_1~2000ms and T_2~275ms [31]. Different imaging techniques can accentuate one form of contrast over another to produce the most useful images of a particular anatomy. For example, T_1-weighted or T_2-weighted imaging

techniques attempt to maximize contrast due to T_1 or T_2 differences (respectively) between tissues.

Additionally, quantitative imaging techniques leverage the exponential signal decay models to generate maps of measured T_1, T_2, or T_2* values across the anatomy. These techniques, typically referred to as T_1, T_2, or T_2* *mapping*, are useful for absolute quantification of tissue in a way that can be directly compared with reference values in healthy and diseased conditions. For example, T_2 mapping can be used to identify the presence of myocardial edema, which causes myocardial T_2 to increase to ~70ms [32]. These principles can also be applied to quantifying other sources of contrast in MRI such as molecular diffusion, which will be discussed further in Chapter 2. In providing this additional information, however, quantitative mapping techniques require sampling of multiple points on the signal decay curve which typically prolongs scan times. However, quantitative MRI can provide

1.3 Gradients and Spatial Localization

Up to this point, the description of MRI does not include any information that can differentiate between different points in space. This critical aspect of MRI is accomplished via the application of magnetic field *gradients*, which superpose with the static B_0 field. Gradients produce a magnetic field with carefully controlled spatial variations that are then used to localize portions of the received signal to distinct points in space.

1.3.1 Gradients

Contained within the MRI hardware are gradient coils that produce magnetic fields that act parallel to the B_0 field (i.e. in the z-direction) but vary linearly across space. Typically, a scanner has three separate gradient coils to produce magnetic field gradients along the x, y, and z directions that can be superposed in linear combinations to generate gradients along arbitrary

directions in space. The fields generated by the gradient coils are substantially lower than the B_0 field and are typically on the order of 10-40mT. Gradient fields are typically measured in units of mT/m, which describes the slope of the linear field variation in space. Clinical MRI hardware typically contains gradients that are capable of generating field variations up to 40-80mT/m and some specialized coils can achieve gradients as high as 300mT/m [5]. The "strength" (i.e. maximum gradient amplitude) of gradient hardware is linked to its ability to resolve small spatial scales and plays an important role in encoding diffusion (Chapter 2).

Gradients are used to spatially localize components of the acquired MRI signal and are thus critical components in the generation of images. To localize signals in three dimensions, gradients are used in three orthogonal processes: slice selection, frequency encoding, and phase encoding.

1.3.2 Slice Selection

Among the simplest examples of using the magnetic field gradients for spatial selectivity is the *slice selective gradient*, which is routinely used to isolate signal from a small portion (or "slice") of the anatomy. For the purposes of this description we assume the slice selective axis is along the z-direction. This is often the case in clinical imaging (as in scans of the brain, spinal cord, abdomen, etc.), but the slice orientation can in principle be arbitrarily defined. For example, cardiac imaging is frequently performed with slices defined by the local anatomy and corresponding to the ventricular short axis.

If we consider a gradient field played along the z-axis and centered at isocenter (z=0) with amplitude G_z we expect a magnetic field that is a linear function of z according to:

$$\vec{\mathbf{G}}(\mathbf{z}) = (\mathbf{B_0} + \mathbf{G_z z})\vec{\mathbf{k}} \quad 1.25$$

Where z represents the distance from isocenter along z and can be a positive or negative quantity. This leads to a corresponding spatial dependence on the precessional frequency (eqn. **1.4**):

$$\mathbf{f(z)} = \frac{\boldsymbol{\gamma}}{\mathbf{2\pi}}(\mathbf{B_0} + \mathbf{G_z z}) \tag{1.26}$$

It follows that an RF pulse tuned exactly to f_0 would now only excite spins that are located exactly at the position z=0. In practice, RF pulses are tuned to excite a range of frequencies which is referred to as the excitation pulse bandwidth. This bandwidth (Δf) can be tuned to excited a slice with thickness Δz according to:

$$\mathbf{\Delta f} = \frac{\boldsymbol{\gamma}}{\mathbf{2\pi}}\mathbf{G_z \Delta z} \tag{1.27}$$

Maintaining constant bandwidth, the slice thickness can be adjusted by simply modifying the gradient amplitude. Two example slice selection excitations are illustrated in Figure 1.1 with varying gradient amplitudes to excite a thicker (A) and thinner (B) slice for constant bandwidth.

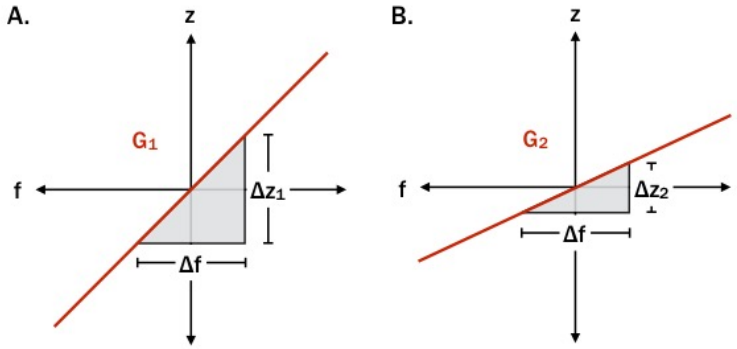

Figure 1.1: Example slice selective gradients played with a low (A) and high (B) gradient amplitude along z. For fixed excitation bandwidth, increasing G leads to a thinner excited slice.

1.3.3 Frequency Encoding

The second component of spatial encoding in MRI is accomplished using *frequency encoding* along the x direction. If we apply a gradient along the x-axis with amplitude G_x, the local precessional frequencies will vary according to the distance from isocenter along x in a form analogous to Equation **1.26**:

$$\mathbf{f(x)} = \frac{\boldsymbol{\gamma}}{\mathbf{2\pi}}(\mathbf{B_0} + \mathbf{G_x x}) \tag{1.28}$$

Thus, the MRI signal at a specific x location can be determined by measuring its frequency in the presence of the known gradient G_x. The interpretation and reconstruction of this information will be described in section 1.3.5.

1.3.4 Phase Encoding

With the x and z positions of the MRI signal determined by frequency encoding and slice selection, what remains is encoding y positions. This is accomplished using the process of *phase encoding*.

Phase encoding employs gradients that are limited in duration and played along the y direction and are turned off prior to the signal being read out (recorded). Let us consider this gradient with amplitude G_y played for a duration Δt. During the time Δt, the gradient produces a spatially varying frequency along y analogous to that described in equation **1.28**:

$$\mathbf{f(y)} = \frac{\boldsymbol{\gamma}}{\mathbf{2\pi}}(\mathbf{B_0} + \mathbf{G_y y}) \tag{1.29}$$

We cannot simply use frequency encoding along y because it would be impossible to distinguish frequency variations from the x and y gradients. However, the frequency differences produced by this gradient during Δt will lead to spatially dependent signal *phases*, φ (in radians) that will persist after the gradient is turned off according to:

$$\boldsymbol{\varphi(y) = 2\pi \cdot f(y) \cdot \Delta t} \quad 1.30$$

Thus, after the phase encode gradient is turned off, the y location of an MRI signal can be localized by its phase.

1.3.5 *k*-space

If a slice selective excitation is followed by a phase encode gradient "blip" and a frequency encoding readout gradient, the full x, y and z position of a signal can be determined. In practice this is recorded and analyzed using a theoretical formalism known as *k*-space which encodes an image in terms of *spatial frequencies* that can be converted to *image space* via the Fourier transformation. The orientation and frequency of an arbitrary two-dimensional spatial pattern can be described by the *k*-vector, $\vec{k}$ = (k_x, k_y). *k*-space describes the magnitude of each spatial frequency, $\vec{k}$ that is present in a particular image as illustrated in Figure 1.2.

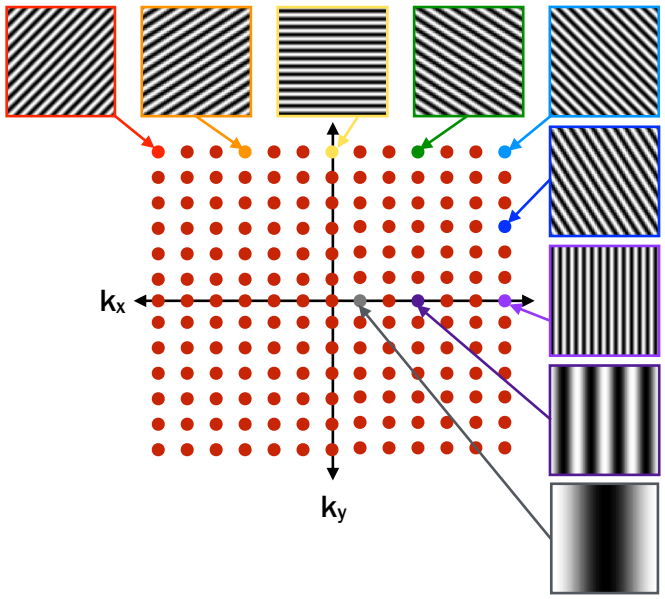

Figure 1.2: Illustration of the spatial frequency information contained in k-space. High spatial resolution information is contained near the edges of k-space while low spatial resolutions (i.e. contrast) information is contained near the center.

The *k*-vector is directly related to the applied gradients according to:

$$\vec{k}(t) = \frac{\gamma}{2\pi}\int_0^{\tau}\vec{G}(t)dt \quad (1.31)$$

Where τ is the duration of the gradient played. It follows that a frequency encode gradient along x allows us to "move" horizontally along k_x while it is being played:

$$k_x(t) = \frac{\gamma}{2\pi}G_x t \quad (1.32)$$

If the signal is read out discretely at time intervals, Δτ, the sampling density of k_x can be described by:

$$\Delta k_x = \frac{\gamma}{2\pi}G_x \Delta\tau \quad (1.33)$$

Similarly, a phase encode gradient "blip" with duration Δt allows us to jump from one k_y line to another:

$$\Delta k_y = \frac{\gamma}{2\pi}G_y \Delta t \quad (1.34)$$

An MRI image is acquired in this way by using frequency and phase encode gradients to move across *k*-space and sample the image signal (S) at each point, $S(k_x,k_y)$. Each point in S includes information from the entire imaged object and is related to the final image intensity by the MRI signal equation:

$$S(\vec{k}) = \int I(\vec{r})e^{-2\pi i \vec{k}\cdot\vec{r}}d\vec{r} \quad (1.35)$$

Where $I(\vec{r})$ is the image intensity at spatial position $\vec{r}$, i.e. the final image. $I(\vec{r})$ represents the available transverse magnetization at each point in space and is dictated by both the pulse sequence used and the properties of the tissue at a given position (i.e. T_1, T_2). It is worth noting

that S represents the Fourier transform of I. I can thus be recovered by taking the inverse Fourier transform of the acquired signal, S:

$$\mathbf{I}(\vec{\mathbf{r}}) = \int \boldsymbol{S}(\vec{\boldsymbol{k}})\, \mathbf{e}^{2\pi \mathbf{i}\, \vec{\mathbf{k}}\cdot\vec{\mathbf{r}}} \mathbf{d}\vec{\boldsymbol{k}} \qquad 1.36$$

Note that in Equation **1**.**35**, the integral is carried out over spatial position and the limits are characterized by the imaging field of view whereas in Equation **1**.**36**, the integral is carried out over *k*-space and the limits are set by the acquired spatial resolution. An example image and its corresponding magnitude *k*-space data are shown in Figure 1.3.

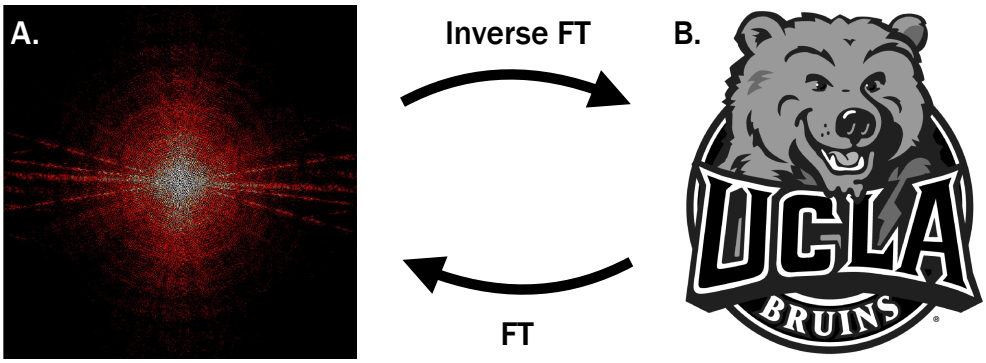

Figure 1.3: Illustration of the relationship between magnitude k-space (A) and image space (B). FT is the Fourier transform.

Several properties of acquired *k*-space data have important implications on a resultant image. The image field of view (FOV) is dictated by the spacing between *k*-space points, Δk_x and Δk_y where:

$$\mathbf{FOV_x} = \frac{\mathbf{1}}{\boldsymbol{\Delta k_x}}$$

$$\mathbf{FOV_y} = \frac{\mathbf{1}}{\boldsymbol{\Delta k_y}} \qquad 1.37$$

Furthermore, the *k*-space extent dictates the acquired spatial resolution:

$$\mathbf{\Delta x} = \frac{\mathbf{1}}{\boldsymbol{k}_{\boldsymbol{x},\mathbf{max}}}$$

$$\mathbf{\Delta y} = \frac{\mathbf{1}}{\boldsymbol{k}_{\boldsymbol{y},\mathbf{max}}} \qquad 1.38$$

Where:

$$\boldsymbol{k}_{\boldsymbol{x},\mathbf{max}} = \frac{\mathbf{N_x}}{\mathbf{2}}\mathbf{\Delta}\boldsymbol{k}_{\boldsymbol{x}}$$

$$\boldsymbol{k}_{\boldsymbol{y},\mathbf{max}} = \frac{\mathbf{N_y}}{\mathbf{2}}\mathbf{\Delta}\boldsymbol{k}_{\boldsymbol{y}} \qquad 1.39$$

And N_x and N_y are the number of k_x and k_y points acquired, respectively (assuming points are acquired symmetrically about the origin). This can be intuitively understand by considering that $k_{x,max}$ and $k_{y,max}$ represent the edges of the acquired *k*-space and thus the highest spatial frequencies sampled which dictates the finest structures that can be resolved in the resultant image. It follows that while Δk_x and Δk_y must be sufficiently small to accommodate a large enough FOV to cover an area of interest, N_x and N_y must be large to achieve high spatial resolutions (i.e. small Δx and Δy).

In most MRI imaging experiments, *k*-space data is acquired one k_y line per excitation and the imaging "sequence" (e.g. the spin echo sequence described in 1.2.3) is repeated many times to acquire all of the necessary *k*-space lines with time, TR between excitations. The scan duration to acquire a full image is thus given by $TR \cdot N_{ky}$ where N_y is the number of acquired k_y lines and dictates the spatial resolution (i.e. voxel size) of the image assuming fixed FOV. Depending on the application, TR can be as short as ~3-5ms or as long as 10s of seconds. As a result, MRI tends to be a very slow imaging modality, wherein the acquisition of a single image can take several minutes (X-ray and CT on the other hand can generate images in seconds).

1.3.6 Echo Planar Imaging

Imaging times can be substantially shortened by acquiring all of the necessary *k*-space data in a single excitation per TR using a technique called Echo Planar Imaging (EPI) [33]. EPI acquires all lines of *k*-space in one *shot* by playing a train of several frequency encoding gradients with alternating polarity separated by phase encoding gradient blips to move between k_y lines. This readout strategy and the resultant *k*-space trajectory are illustrated in Figure 1.4. EPI permits the acquisition of a full 2-dimensional image with only a single excitation, which accelerates the acquisition by a factor of N_y. This makes EPI useful in applications requiring multiple repeated acquisitions in the same spatial location such as diffusion weighting imaging, which is of particular interest in this thesis and will be described at length in Chapter 2.

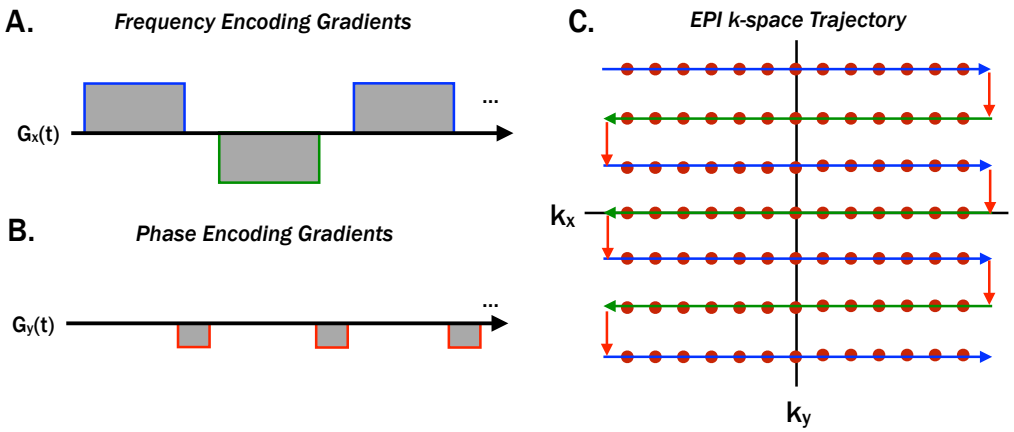

Figure 1.4: Illustration of the frequency encoding gradients (A), phase encoding gradient blips (B), and the resultant k-space trajectory used in echo planar imaging (EPI).

The acquisition efficiency gains made possible with EPI, however, do not come without any cost and there are several drawbacks that must be considered. First, because EPI readouts traverse the entirety of *k*-space, they impart a larger temporal footprint on the pulse sequence itself than traditional single-line readout schemes. Because the imaging echo must be timed to the center line of k-space (which falls in the middle of the EPI readout), this can extend the

minimum achievable echo time (TE) in spin echo based imaging techniques which limits image signal to noise ratios (SNR) due to T_2 decay. This effect becomes more dramatic as the spatial resolution is increased and more k_y lines must be acquired. This issue can be mitigated by shortening the time to *k*-space center using *k*-space undersampling strategies such as partial Fourier imaging [34], which exploits the Hermitian symmetry of *k*-space, or parallel imaging which uses the signal received by different MRI coils to solve for missing data [35].

Another drawback of EPI is an increased sensitivity to magnetic field inhomogeneity that can lead to geometric image distortions. This is because small persistent field errors that distort the *k*-space trajectory compound over time with each gradient that is played. This results in a mismatch between the expected and actual *k*-space positions that increases throughout the readout. As a result, EPI images tend to have substantial distortions in regions of the body with large magnetic susceptibility gradients that leads to an inhomogeneous B_0 field. These problem areas tend to be in regions that contain both water and air such as parts of the brain that are close to the sinus and nasal cavities and the lateral left ventricular wall of the heart which is adjacent to the left lung. These distortions can be mitigated by either reducing the duration of the EPI readout (using the same techniques described above) or by carefully tuning the magnetic field in the anatomical region of interest using a process called *shimming*.

Image *ghosting* is another artifact that tends to appear in EPI images and also stems from a mismatch between the expected and acquired *k*-space trajectory. Ghosting tends to appear as faint repetitions of the anatomy near the image edges and is caused by differences between readout gradients with opposite polarity (i.e. blue left-right gradients and green right-left gradients in Figure 1.4). Several sources of error can lead to ghosting, such as eddy currents (which will be discussed at length in Chapter 7), gradient delays, and field inhomogeneities. A common method for correcting this artifact is acquiring a few *reference lines* of *k*-space read out in each direction that can be used to correct the subsequently acquired imaging data.

2 DIFFUSION WEIGHTED MRI

Diffusion weighted imaging (DWI) is a quantitative MRI technique which encodes diffusion, the random Brownian motion, of water molecules into the MRI signal. DWI has profound clinical value because the diffusive properties of water molecules in soft tissues are affected by local cellular environments and can thus be used to characterize microstructural changes that occur in disease. This chapter will introduce the theoretical underpinnings of DWI and briefly describe the DWI acquisition.

2.1 Molecular Diffusion

The process of diffusion describes the random motion of molecules in a medium and is often referred to as *Brownian motion* in reference to the botanist, Robert Brown who observed (but did not explain) this process amongst pollen particles suspended in water [36]. While diffusion is a random process and thus cannot be described mechanistically on the single particle level, it was described statistically by Albert Einstein in 1905 [37]. In this description, a large system of particles is described by a density function, ρ that varies over space and time according to the molecular diffusion coefficient, D and the following diffusion equation:

$$\frac{\partial \rho(\vec{r}, t)}{\partial t} = D\nabla^2 \rho(\vec{r}, t) \quad (2.1)$$

Roughly, this equation states that the first temporal derivative of the density function is equivalent to its second spatial derivative scaled by D. If we only consider motion along the x-direction, this equation simplifies to:

$$\frac{\partial \rho(x, t)}{\partial t} = D\frac{\partial^2 \rho(x, t)}{\partial x^2} \quad (2.2)$$

If we consider a system of N molecules starting from a common position x=0, the following solution to this equation can be reached:

$$\rho(x, t) = \frac{N}{\sqrt{4\pi Dt}} e^{-\frac{x^2}{4Dt}} \quad (2.3)$$

This solution describes the probability density function of a normal distribution with a mean of 0 and a variance, $\sigma^2=2Dt$. This one-dimensional solution can be extended to three-dimensions and illustrates that diffusion causes the molecules in a system to spread out over time and take the form of a normal distribution in space. The diffusion coefficient describes the variance of the resultant distribution according to:

$$D = \frac{\sigma^2}{2t} \quad (2.4)$$

Where D has the units of position squared over time and is commonly measured in mm^2/s or mm^2/ms.

2.1.1 Restricted Diffusion

On a fundamental level, the diffusion coefficient of a system of molecules in a gas or liquid is related to the surrounding temperature, pressure and viscosity. However, water molecules in a structured environment tend to encounter boundaries that restrict their free motion. This is the

case for water contained in human tissue, which interacts constantly with cell walls. This restriction of motion can have a measurable impact on the effective diffusion coefficient of these water molecules in certain experimental conditions.

Consider a set of water molecules diffusing in two-dimensions with some diffusion coefficient, D, from a common point of origin (x=y=0) with no structure restricting their motion in either direction. If we measure the variance of their spatial distribution at two time points, t_1 and t_2 (where $t_2>t_1$), Equation **2.4** says that we will recover: $\sigma_1^2=2t_1D_1$ and $\sigma_2^2=2t_2D_2$ where $D_1=D_2=D$.

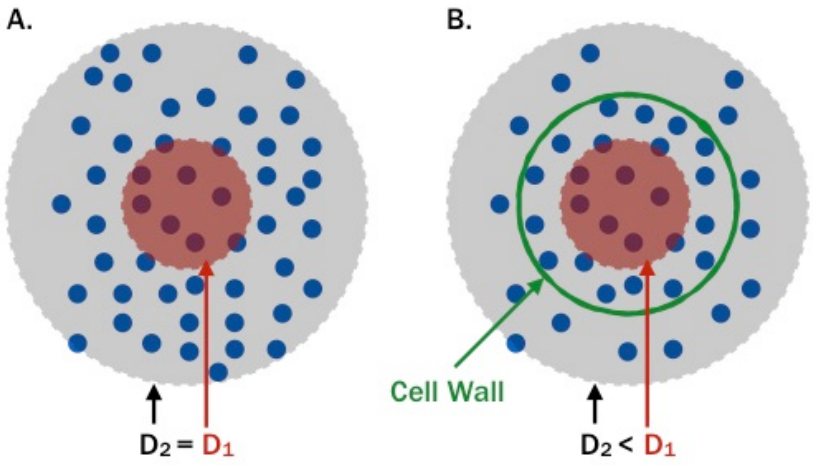

Figure 2.1: Illustration of unrestricted (A) and restricted diffusion (B) as measured over a short distance scale (red circle) and long distance scale (grey circle). In the unrestricted case, both experiments yield identical measures of diffusivity ($D_1=D_2$), but in the restricted case, the longer timescale experiment yields a lower effective diffusion coefficient ($D_2<D_1$).

Consider, however, a circular cell wall surrounding the origin with a diameter between σ_1 and σ_2 and some permeability factor <1 (i.e. molecules that come in contact with the wall have some probability of reflecting off the wall and back towards the origin). The measurement made at t_1 are unaffected by this boundary and will still report $\sigma_1^2=2t_1D_1$ where $D_1=D$, but the measurement made at t_2 will reflect both the underlying diffusivity, D and the probability of molecules reflecting

off of the wall. Thus, this measurement will yield $\sigma'^2_2=2t_2D'_2$ where $D'_2<D$. The molecules in this case are thus undergoing *restricted diffusion*.

Measurements of diffusivity made using DWI typically operate on a time scale (and thus spatial scale) where cell boundaries significantly restrict diffusion. In fact, this is what makes quantifying diffusion in human tissue a useful endeavor, as it permits the observation of changes in cellular structure that affect the diffusive process. For example, the breakdown of cell walls that occur after cell death can be observed via an increase in diffusivity that can provide valuable insight into the progression of disease.

2.1.2 Diffusion Anisotropy

Section 2.1.1 addressed the behavior of diffusing molecules in the presence of *isotropic* boundaries that restrict diffusion equivalently in all directions. However, many biological tissues are made up of cells with distinctly anisotropic structure that do not behave in this manner. Two examples that are of particular interest in this thesis are neurons, which make up much of the structure of the brain and cardiomyocytes, which comprise the heart, both of which have distinct long and short axes.

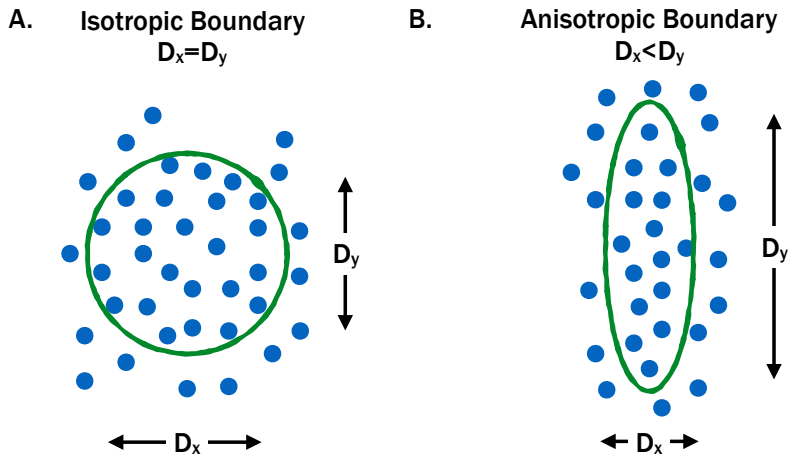

Figure 2.2: Diffusion of water molecules as restricted by an isotropic (A) and anisotropic boundary (B). Anisotropic boundaries restrict diffusion to varying

degrees along different orientations, resulting in direction-dependent measures of diffusivity. In this case, a cell boundary aligned preferentially in the y direction results in a higher effective diffusivity along the y orientation than along the x orientation.

In the case of anisotropic restriction, measures of diffusivity have an additional dependence on measurement orientation as illustrated in Figure 2.2. If we consider a cell with a long axis aligned along the y direction (Figure 2.2B), water molecules are more likely to encounter boundaries when travelling along the x direction than along the y direction. This results in a higher spatial variance along y and thus a higher effective diffusivity along y.

The implications of diffusion anisotropy are twofold. First, this means multiple measurements of diffusivity are required to accurately capture the full picture of the diffusion underlying a tissue in question. A measurement made along a single direction can be highly dependent on a cells orientation in space and thus risk being substantially biased. Second, we can use measurements of diffusion in several directions to actually capture the orientations of the cells that make up human tissue. This opens up a fascinating field of quantitative microstructural mapping that permits the visualization of neuronal fiber tracts in the brain and of the complex organization of myocardial microstructure. Techniques that employ this phenomenon will be discussed in 2.4.

2.2 Diffusion Encoding Gradients

The basic premise of DWI is that MRI gradients can impart decays in image intensity that are directly related to the diffusion coefficient of the water molecules underlying the tissue being imaged. The gradient pulses used to encode diffusion are technically no different from those used for spatial encoding, but they tend to require substantially larger amplitudes (40-80mT/m) and/or longer durations in order to sufficiently encode diffusive motion into the MRI signal. In

fact, because DWI frequently utilizes the maximum capabilities of the gradient coils it is a major driver behind the development of new gradient hardware [5].

Just as the spatial encoding gradients discussed in Chapters 1.3.2-1.3.4 impart a spatially dependent frequency variation on image that allows us to resolve signals from discrete image voxels, these gradients also produce a gradient of frequencies within each voxel. As discussed in the context of T_2 decay in Chapter 1.2.3, any frequency variability within a voxel leads to a range of phases and thus a loss of signal coherence referred to as *intravoxel dephasing*. The result of this is a reduction of signal amplitude and is typically an undesirable phenomenon. This phenomenon is exploited in DWI, however, and is central to generating diffusivity-based contrast.

2.2.1 Intra-voxel Dephasing

Let us first consider the simplest and earliest form of the DWI experiment that was proposed by Stejskal and Tanner in 1964 [1] and is still widely used today. This acquisition is based on a spin-echo pulse sequence (as discussed in chapter 1.2.3), but with two identical diffusion encoding gradients along the x-axis, G_1 and G_2, placed before and after the refocusing pulse. Following G_1, spins within a voxel will accumulate a phase, $\varphi=\varphi_1(x)$ that is dependent on their x-position within the voxel. This phase is then flipped 180° after the refocusing pulse resulting in $\varphi=-\varphi_1(x)$. Then, provided the spins do not move at any point, G_2 will impart the same phase, $\varphi_2(x)=\varphi_1(x)$ and cancel the phase from the first gradient pulse, regardless of position, resulting in a fully refocused signal: $\varphi=\varphi_1(x)+\varphi_2(x)=\varphi_1(x)-\varphi_1(x)=0$. This process is illustrated in Figure 2.3A.

However, if any motion occurs at any point in this sequence, the phase accumulated from G_1 and G_2 will no longer cancel each other out. If we consider the simple case of two spins with differing x-positions, we see that after G_1, they accrue distinct phases: φ_{11} and φ_{12} that are

flipped after the refocusing pulse to $-\varphi_{11}$ and $-\varphi_{12}$. If the spins exchange positions between G_1 and G_2, G_2 will impart the phase that the *other* spin accrued from G_1: $\varphi_{21}=\varphi_{12}$ and $\varphi_{22}=\varphi_{11}$. This results in a net, non-zero and non-equivalent phase for the two spins: $\varphi_1=\varphi_{12}-\varphi_{11}\neq 0$ and $\varphi_2=\varphi_{11}-\varphi_{12}\neq 0$. The difference in phases, $\Delta\varphi=|\varphi_2-\varphi_1|$ dictates the degree of dephasing and thus the magnitude of the signal loss. This process is illustrated in Figure 2.3B.

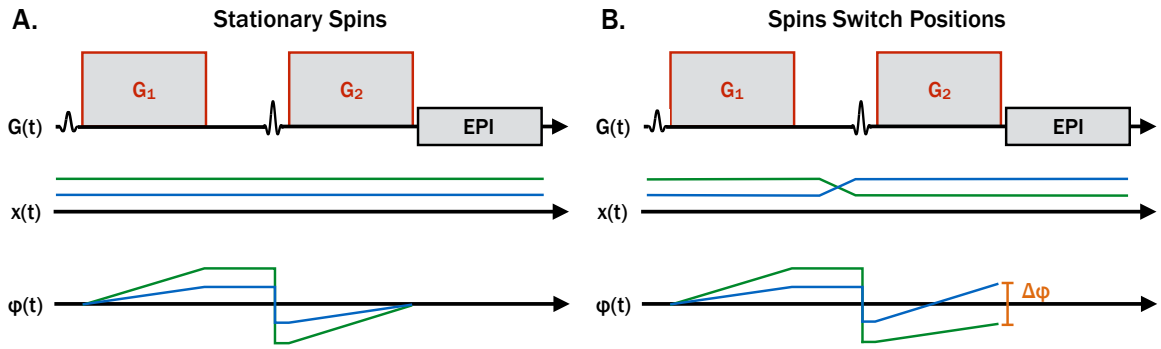

Figure 2.3: Illustration of intra-voxel dephasing in a basic Stejskal-Tanner DWI acquisition. Stationary spins (A) at two different locations (green and blue curves) are imparted with equal and opposite signal phases from identical gradients G_1 and G_2 before and after a refocusing pulse, which results in a net phase of 0. However, if the spins exchange locations (B), the phases accrued from G_1 and G_2 no longer cancel, resulting in a net phase, $\Delta\varphi$, which attenuates the MRI signal. Larger displacements and/or larger gradient pulses will result in larger phase dispersion and thus a greater decay of the MRI signal.

In the case of randomly diffusing spins, the system becomes significantly more complicated, but the principle remains the same. In the case of a large system of diffusing spins constituting an imaging voxel, a statistical description relating the MRI signal to the underlying diffusion coefficient, D becomes particularly useful and will be described in the following section.

2.2.2 Diffusion Encoding Factors

As described in Section 2.1, the diffusion of molecules with diffusion coefficient, D will generate a density function over time that can be described by a normal distribution with variance $\sigma^2=2Dt$

(Eqn. **2.4**). In the presence of a diffusion encoding gradient, this motion will lead to signal dephasing as described in section 2.2.1. The magnitude of this dephasing and the resultant signal decay is dictated by the diffusion encoding *strength* (i.e. magnitude and duration) of the applied gradient pulse and is typically referred to as the sequence b-value (or simply, b). The diffusion weighted signal magnitude can be described according to b and D using a mono-exponential decay model:

$$\mathbf{S(b)} = \mathbf{S_0 e^{-bD}} \tag{2.5}$$

Here S_0 represents the signal without diffusion encoding gradients (i.e. b=0) and is typically T_2 weighted (in the case of a spin echo DWI pulse sequence). D can thus be calculated from a DWI signal provided b and S_0 are known. Fortunately, b can be calculated directly from the applied diffusion encoding gradient waveform and thus known ahead of time. For an arbitrary gradient waveform G(t) defined over time, the phase offset, F can be defined:

$$\mathbf{F(t)} = \boldsymbol{\gamma} \int_0^{\mathbf{t}} \mathbf{G}(\boldsymbol{\tau})\, \mathbf{d}\boldsymbol{\tau} \tag{2.6}$$

F(t) has units of inverse distance and represents the k-space offset caused by G(t). Note that in this description, G(t) must be inverted after any refocusing pulse, which could alternately be described using a Heaviside function. The b-value can then be defined as a function of time by integrating the square of F:

$$\mathbf{b(t)} = \int_0^{\mathbf{t}} \mathbf{F}(\boldsymbol{\tau})^2\, \mathbf{d}\boldsymbol{\tau} \tag{2.7}$$

The pulse sequence b-value is then defined by $b(T_{Diff})$ where T_{Diff} is the time of the end of diffusion encoding gradient waveforms and has units of inverse diffusivity (i.e. s/mm^2). Typical b-values can range from 300-2000s/mm^2 and vary depending on application. Higher b-values

generate greater diffusion contrast, but result in lower image SNR and tend to be more sensitive to corruption due to bulk physiological motion.

While presented as a scalar quantity in Equation **2**.**7**, b is truly a vector quantity with directionality that is dictated by the orientation of the diffusion encoding gradient pulse. That is, a gradient waveform played along x has a non-zero b-value along x, b_x, but has no b-value along y or z (b_y=b_z=0). Furthermore, by simultaneously playing gradients along different combinations of x, y, and z, b-values with arbitrary orientations can be achieved.

2.3 DWI Acquisition and Reconstruction

The basic goal of a DWI experiment is to determine the diffusivity, D underlying the tissue of interest. Once the b-value of a pulse sequence is determined, the DWI signal (equation **2**.**5**) has two remaining unknowns: D and S_0 (the non-diffusion weighted reference signal). D can thus be determined by performing two experiments with different b-values: b_1 and b_2. In this case, two signals, S_1 and S_2 are generated:

$$\mathbf{S_1 = S_0 e^{-b_1 D}}$$
$$\mathbf{S_2 = S_0 e^{-b_2 D}} \qquad 2.8$$

We can now easily solve for D:

$$\mathbf{D = \frac{\ln(S_1/S_2)}{b_2 - b_1}} \qquad 2.9$$

A typical DWI acquisition uses one high b-value, b_2=b and one reference image with b_1=0.

Because diffusion anisotropy typically exists (to varying degrees) in biological tissues, this process must be performed with diffusion encoding along multiple directions to determine an overall measure of net diffusivity. For example, diffusion encoding gradients applied perpendicular to a neuronal fiber axis will yield lower measures of D than gradients applied

parallel to the fiber. To ensure unbiased measurement, DWI are typically acquired with diffusion encoding along three orthogonal directions (i.e. x, y and z). Note that because there is no directionality associated with a b=0 reference image, only images with b>0 need to be acquired along multiple directions. The resulting measure of D from all acquired directions is typically referred to as the *apparent diffusion coefficient* (ADC) as it reflects an ensemble estimate of the underlying diffusivity as quantifiable from the experiment performed.

Tissue ADC has proven to be a useful biomarker for several pathologies. The most widely employed application of ADC is the diagnosis of stroke, which is characterized by an acute decrease in ADC in affected regions of the brain, followed by a increase in ADC in the chronic stage. Tumors also tend to exhibit a decrease in ADC, which reflects an increase in cell proliferation that is characteristic of many cancers and has made DWI a useful technique in treatment planning for radiation therapy. Increases in ADC also indicate the presence of fibrosis in myocardial infarction (MI), which will be discussed later in this thesis.

2.4 Diffusion Tensor Imaging

The mathematics described in Section 2.3 can be extended to quantify the diffusivity within a complex system, including the extent and orientation of diffusion anisotropy. If diffusivity is independently measured along several orientations, it stands to reason that the shape of the molecular environment can come into view (i.e. directions with high and low degrees of restriction can be determined). A convenient framework for understanding the shape and orientation of this restricted environment is the second order diffusion tensor, which models the system's diffusivity as a three-dimensional ellipsoid. The acquisition and reconstruction of the diffusion tensor with diffusion weighted MRI is referred to as Diffusion Tensor Imaging (DTI).

2.4.1 Acquisition and Reconstruction

We can model the overall diffusivity within a system with a diffusion tensor that takes the form:

$$\mathbf{D} = \begin{bmatrix} \mathbf{D_{11}} & \mathbf{D_{12}} & \mathbf{D_{13}} \\ \mathbf{D_{21}} & \mathbf{D_{22}} & \mathbf{D_{23}} \\ \mathbf{D_{31}} & \mathbf{D_{32}} & \mathbf{D_{33}} \end{bmatrix} \quad 2.10$$

Because diffusion is a bi-directional process (i.e. the rates of diffusivity along antiparallel directions must be equivalent), this tensor must be symmetric (i.e. D_{12}=D_{21}, D_{13}=D_{31} and D_{23}=D_{32}). Consequently, the tensor contains only six unique quantities.

By performing the DWI experiment described in section 2.3 with diffusion encoding gradients played along some arbitrary direction, $\vec{r}$, with b-value, b we can measure the signal weighted by the diffusivity along $\vec{r}$:

$$\mathbf{S_r} = \mathbf{S_0 e^{-b_r D_r}} \quad 2.11$$

Where D_r represents the projection of the diffusion tensor, **D** along $\vec{r}$:

$$\mathbf{D_r} = \vec{\mathbf{r}} \cdot \mathbf{D}\vec{\mathbf{r}} \quad 2.12$$

Considering the six unique elements of **D** and the reference signal S_0, this leaves a system of equations with seven unknowns. **D** can thus be fully determined from a set of seven measurements including measures of diffusivity along at least six unique directions. It is also sometimes useful to acquire greater than the minimum six directions and generate an overdetermined system of equations that can mitigate the effects of measurement noise. In practice DTI experiments are often performed with 10-30 distinct diffusion encoding directions.

To effectively measure the diffusion tensor, it is important to carefully choose the set of diffusion encoding directions. Because tissues in the human body tend to contain cellular structures with a wide range of orientations, it is important to choose a set of directions that are

widely spaced and thus fully cover the range of possible tensor orientations. This is commonly achieved using regular polyhedra with varying numbers of vertices that can represent gradient orientation vectors [38]. These include the octahedron (six vertices), icosahedron (12 vertices) and the dodechahedron (20 vertices). Another technique for designing a well-spaced gradient vector set is modelling the electrostatic repulsion of point particles on the surface of a unit sphere [39].

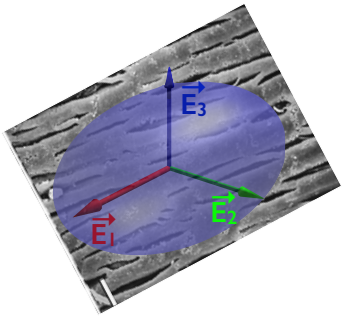

Figure 2.4: Visualization of a diffusion tensor, which represents the diffusivity within in each image voxel as an ellipsoid with three orthogonal principal directions of diffusion ($\vec{E}_1$, $\vec{E}_2$, and $\vec{E}_3$). $\vec{E}_1$ corresponds, for example, with the orientations of fibers present in the human brain and heart.

2.4.2 Properties of the Diffusion Tensor

A useful way to describe the diffusion tensor is to decompose it into its principal axes and its diffusive magnitude along each of those axes. This can be easily done by determining the three eigenvectors ($\vec{E}_1$, $\vec{E}_2$, and $\vec{E}_3$) and eigenvalues (λ_1, λ_2 and λ_3) of the diffusion tensor via the following equation:

$$\mathbf{D}\mathbf{E}_\mathbf{j} = \boldsymbol{\lambda}_\mathbf{j}\mathbf{E}_\mathbf{j} \qquad 2.13$$

Where j = 1, 2 or 3. $\vec{E}_1$, $\vec{E}_2$, and $\vec{E}_3$ represent the principal directions of diffusion and give a full description of the orientation of the tensor. $\vec{E}_1$ is particularly significant as it has been well

correlated with histological measurements of tissue fiber orientation in the brain [40] and heart [41, 42].

The size and shape of the diffusion tensor are contained in the three eigenvalues, λ_1, λ_2 and λ_3, which describe the magnitude of diffusivity along $\vec{E}_1$, $\vec{E}_2$, and $\vec{E}_3$. For example, highly anisotropic systems may contain very disparate eigenvalues (e.g. $\lambda_1 >> \lambda_2$ and $\lambda_1 >> \lambda_3$) whereas more isotropic systems will have less eigenvalue disparity (e.g. $\lambda_1 \sim \lambda_2 \sim \lambda_3$). Tensor shape is commonly described using tensor *invariants*, which describe the tensor in a rotationally invariant manner. The most commonly used invariants are: mean diffusivity (MD), which describes the overall magnitude of diffusion and is an analog to the ADC; fractional anisotropy (FA), which describes the degree of anisotropy in the tensor; and tensor mode, which describes the shape of the anisotropy. These invariants are described by the following equations:

$$\mathbf{MD} = \frac{\boldsymbol{\lambda_1} + \boldsymbol{\lambda_2} + \boldsymbol{\lambda_3}}{\mathbf{3}} \tag{2.14}$$

$$\mathbf{FA} = \sqrt{\frac{\mathbf{3}(\,(\boldsymbol{\lambda_1} - \mathbf{MD})^{\mathbf{2}} + (\boldsymbol{\lambda_2} - \mathbf{MD})^{\mathbf{2}} + (\boldsymbol{\lambda_3} - \mathbf{MD})^{\mathbf{2}})}{\mathbf{2}(\boldsymbol{\lambda_1^2} + \boldsymbol{\lambda_2^2} + \boldsymbol{\lambda_3^2})}} \tag{2.15}$$

$$\mathbf{Mode} = \frac{\boldsymbol{\lambda_1}\boldsymbol{\lambda_2}\boldsymbol{\lambda_3}}{\mathbf{norm}(\mathbf{D} - \mathbf{MD} \cdot \mathbf{I})^{\mathbf{3}}} \tag{2.16}$$

Where I is the 3x3 identity matrix. MD has the same units as ADC (typically mm^2/s or mm^2/ms) and is always greater than 0. While there is no mathematical limit on the maximum MD, it is not expected to exceed the rate of diffusivity for free water (i.e. unrestricted) at 37° C (human body temperature): $3mm^2/ms$. FA is a unitless quantity that can range from 0, which indicates perfectly isotropic (spherical) diffusion and 1 indicates highly anisotropic diffusion (i.e. large disparity between eigenvalues). Mode is also unitless and can range from -1 to 1. Mode values close to 1 indicate a high degree of linear anisotropy (i.e. $\lambda 1 >> \lambda 2 \sim \lambda 3$) whereas modes close to -1 indicate a high degree of planar anisotropy (i.e. $\lambda 1 \sim \lambda 2 >> \lambda 3$).

2.5 Higher Order Diffusion Imaging Techniques

While DTI provides a wealth of information about the microstructure underlying human tissue, it is clear even from the simple example provided in Section 2.1.1 that it is insufficient for a full description. Because DTI only considers angular deviation of the underlying diffusivity, it does not incorporate any information regarding different length scales. For example, if the timescale of the diffusion measurement is sufficiently short such that diffusing molecules do not have time to interact with any structures that restrict their motion, the measured diffusion tensor will take an isotropic, spherical shape that provides little information about the micro-environment. In some cases, it may be useful to probe the diffusive system at multiple length scales to provide a more nuanced picture. Furthermore, the DTI model can be confounded simply by the presence of crossing fibers, which occur in several regions of the brain.

Higher order diffusion imaging techniques have been developed to overcome these limitations. These techniques, in general add to the DTI model by incorporating an additional degree of freedom that varies the length scales of diffusion encoding measurements in addition to their orientations. They also generally sample at a much higher angular density (sampling hundreds of unique directions) and use more sophisticated models to describe the diffusivity in terms of a probability distribution. Some notable higher order techniques are Diffusion Spectrum Imaging (DSI) [43], Q-ball imaging [44] and Generalized Q-sampling Imaging (GQI) [45]. Of course, the additional information required for these techniques results in substantially longer scan times which makes them unlikely candidates for any wide-scale clinical adoption.

2.6 Common Problems with DWI

While DWI is a well-established method with a robust clinical track record, it remains a fairly challenging and time consuming technique. There are several potential sources of error in DWI

that, while not unique to DWI, are accentuated by specific aspects of the acquisition. First, because DWI and DTI reconstructions require several matched acquisitions with varying diffusing weightings, it is important to employ a very fast acquisition strategy in order to keep scan times reasonable. For this reason, EPI is the most common readout used in DWI because it permits reconstruction of a full two-dimensional image in every TR. Consequently, DWI inherits all of the drawbacks associated with EPI that were discussed in section 1.3.6 including geometric distortions, ghosting artifacts, and a large temporal footprint in the spin echo pulse sequence.

The remainder of this section will discuss some additional limitations of the DWI acquisitions. Each of these issues is addressed to some extent by the developments described in this thesis and will thus be discussed at greater length in later chapters.

2.6.1 Bulk Motion

There are two ways in which bulk tissue motion can adversely affect a DWI experiment: *inter-shot motion* and *intra-shot motion*.

Inter-shot motion describes displacements that occur between TRs and thus between the acquisition of different diffusion encoding measurements. If uncorrected, this results in mis-registration between DWI images that confounds reconstruction. Common sources of this error are a subject shifting or turning in the scanner as well as respiratory induced organ displacements. Fortunately, these displacements can be easily corrected by performing image registration between all acquired DWI prior to reconstruction [46].

Intra-shot motion describes displacements that occur within a single TR including, most critically, during the application of the diffusion encoding gradients. Although diffusion encoding gradients are designed to encode diffusive motion, there is nothing inherent in their sensitivity to this specific source of motion. In fact, because bulk motion (e.g. respiratory motion, cardiac

motion, a restless subject moving in the scanner) is typically several orders of magnitude larger than diffusive motion, it can even eliminate the entire available DWI signal. This source of error is challenging, if not impossible to correct retrospectively and can be associated with cardiac motion either in DWI in the heart itself or in regions of the liver close to the heart. Intra-shot motion is best dealt with prospectively by careful design of the diffusion encoding gradient itself. This strategy will be discussed at length in Chapters 3 and 4.

2.6.2 SNR

DWI suffers from very low SNR for two separate, but related reasons: diffusion-based signal decay and long TEs. Because diffusion is encoded as a decay in the MRI signal (Eqn. **2.5**) this necessarily reduces the SNR of images with b>0. Therefore, for a given b=0 reference image SNR, the corresponding diffusion weighted images will have substantially lower SNR, particularly for high b-values. This can be mitigated with judicious signal averaging (i.e. several repeated acquisitions), but this obviously increases the overall scan duration.

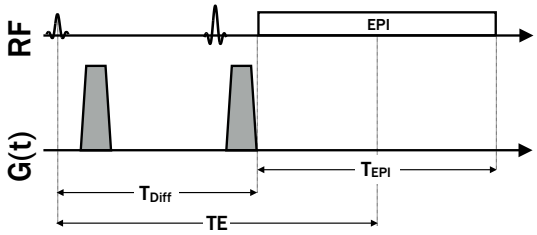

Figure 2.5: Pulse sequence diagram showing a spin echo EPI DWI acquisition with a traditional monopolar (i.e. Stejskal-Tanner) diffusion encoding strategy. The minimum TE (which dictates image SNR) is limited by both the duration of the EPI readout and the diffusion encoding gradients.

DWI acquisitions typically require a relatively long TE (typically greater than 50ms and sometimes as long as 100ms) due to the temporal footprint of the EPI readout and the need for long diffusion encoding gradients to achieve a sufficient b-value (Figure 2.5). This leads to

substantial T_2 signal decay and thus a reduction in SNR. One way to reduce the TE is to shorten the EPI readout by either reducing the acquired spatial resolution or undersampling *k*-space (i.e. parallel imaging or partial Fourier imaging). However, both coarse spatial resolution and *k*-space undersampling can result in reduced image quality and increased sensitivity to intra-shot bulk motion artifacts. Additionally, because *k*-space undersampling itself unavoidably reduces SNR, the trade-offs between shorter TEs and fully sampled acquisitions can be situation-dependent and are not always obvious.

TE can also be shortened by increasing the amplitude of the diffusion encoding gradients, which can shorten the time needed to achieve a given b-value. However, diffusion encoding gradients already tend to utilize the maximum gradient amplitudes achievable on clinical systems. The technique described in chapter 4 presents an alternative method for shortening TE by optimizing the diffusion encoding gradient waveform for optimal echo time efficiency. This permits a reduction of TE without shortening the EPI readout duration or developing improved gradient hardware.

2.6.3 Eddy Currents

The time varying magnetic fields generated by gradient pulses produce unwanted eddy currents in MRI hardware components, which generates background magnetic fields that superpose and distort the shapes of the applied gradient waveforms. One commonly used measure to deal with eddy currents is the use of *shielded gradient coils* which compensate for the eddy currents from the primary gradient coil by playing an opposed gradient field with a secondary outer coil. Another approach is *gradient pre-emphasis*, which accounts for the expected gradient distortion from eddy currents by playing a waveform that is intentionally distorted in the opposite direction. This results in a final waveform that more closely resembles the targeted gradient waveform design.

Despite these routine correction strategies, eddy currents persist as a source of error in DWI and DTI due to the need for gradient pulses with particularly large amplitudes and long durations. Eddy currents produced by diffusion encoding gradients can lead to severe image distortions that are highly dependent on the diffusion encoding direction. This leads to mis-registration between DWI measurements and can corrupt the reconstructed diffusion tensor, particularly near anatomical boundaries. These artifacts can be corrected by applying an affine transformation to co-register all DWI prior to tensor reconstruction, but this requires an additional post-processing step and tends to be sensitive to the choice of registration technique. Another approach is to redesign the diffusion encoding gradient waveform to nullify the effects of eddy currents and prevent the distortions from occurring in the first place. One such approach is the twice refocused spin echo (TRSE) sequence which uses a multipolar gradient scheme and an additional refocusing pulse to virtually eliminate eddy current induced image distortions. However, this approach further increases TE and reduces SNR compared with conventional monopolar (i.e. Stejskal Tanner) DWI. In Chapter 7 we further discuss this phenomenon and present an alternative approach using a convex optimized diffusion encoding scheme that nullifies the effects of eddy currents without increasing TE compared with monopolar encoding (and even reduces TE in many cases).

3 IMAGING CARDIAC MICROSTRUCTURE WITH DWI

Cardiac diffusion weighted imaging (cDWI) is an emerging diagnostic technique due to its ability to quantify microstructrual changes in diseased myocardium without the injection of a gadolinium based contrast agent. Despite its value, cDWI has not gained widespread adoption due to several technical challenges that have limited its robustness as a clinical tool. This chapter will outline the clinical value of cDWI as well that the technical challenges facing the technique and current approaches for overcoming them.

3.1 Cardiac Microstructure

3.1.1 Structure of the Healthy Myocardium

The heart is a muscular organ that facilitates the circulation of blood throughout the body. The heart consists of four chambers: the right atrium (RA), which receives deoxygenated blood from the venous system; the right ventricle (RV), which pumps this blood to the lungs to be oxygenated via the pulmonary artery; the left atrium (LA), which receives oxygenated blood from the lungs via the pulmonary veins; and the left ventricle (LV), which pumps oxygenated blood through the aorta to be circulated throughout the body. The heart beats in a fairly regular pattern

in a cardiac cycle that includes two main phases: diastole, or the relaxing of myocardial muscle while blood enters and fills the ventricles; and systole, the contraction of the ventricles and outward propulsion of blood. The LV plays a particularly critical role in the circulatory system as its contraction provides cells throughout the body with the oxygen necessary to function and will be the focus of the remainder of this chapter.

The LV is comprised by a continuously branching syncytium of cardiomyocytes (muscle cells) that are predominantly oriented circumferentially about the cavity at the mid-wall, but with a helical pitch that varies transmurally from approximately +60° at the endocardial surface to -60° at the epicardial surface [47]. These myocytes shorten along their long axis by a factor of 10-15% and thicken by about 8% during cardiac contraction, which in part facilitates the thickening of the LV wall and the expulsion of blood from the LV cavity. However, 8% fiber thickening is insufficient to explain the >25% wall thickening that is observed during contraction and thus another mechanism must contribute [48]. This disparity can be explained by the organization of myocyte subgroups into laminar sheets or “sheetlets.” Sheetlets are aligned in two dominant groups that are predominantly oriented orthogonal to each other and to the local fiber orientation [49]. Adjacent sheets are separated by cleavage planes that facilitate shearing and reorientation during contraction. This dynamic can explain the observed degree of LV wall thickening [50] and has been observed *in vivo* with cardiac DTI [16]. The combined effect of fiber thickening and sheetlet reorientation (shearing) leads to sufficient LV contraction to facilitate ejection fractions (the fraction of blood in the LV cavity that is expelled during a single contraction) of 50-70% and facilitates the efficient circulation of blood throughout the body.

3.1.2 Myocardial Infarction

Heart disease is a serious and growing health concern in the western world and is the leading cause of death in the United States [51]. Heart disease can take many forms and describes

anything that prevents the heart from effectively circulating blood, but approximately half of the approximately 6 million cases of heart failure in the United States are caused by LV contractile dysfunction [52]. For the purpose of this thesis, one particular cause of LV dysfunction, Myocardial Infarction (MI) will be described, particularly in the context of its detection and evaluation with MRI.

Myocardial Infarction describes the temporary loss of blood flow to myocardial tissue that is generally caused by blockages in the coronary arteries by atherosclerotic plaque. In the acute stage, MI is marked by severely compromised cardiac function and inflammation. Even after blood flow is restored via surgical or medicinal intervention, MI typically results in the death of myocytes in the affected area. The space previously occupied by healthy myocytes is eventually filled with collagen, resulting in myocardial scar tissue, or fibrosis.

In the chronic stage of MI, fibrotic regions can be identified by observing abnormalities in wall motion using ultrasound imaging [53] or dynamic MRI [54]. However, the ability to fully characterize the size and shape of an infarct can be valuable for clinical management, which motivates the use of specialized imaging techniques. An effective method for visualizing an infarct is an MRI technique called Late Gadolinium Enhancement (LGE) [55] which leverages contrast generated subsequent to the injection of a gadolinium based contrast agent (GBCA) that shortens T_1 in proportion to the local proportion of extracellular space. Unfortunately, LGE MRI cannot be used in the large cohort of patients with limited renal function due to a risk for developing Nephrogenic Systemic Fibrosis (NSF), an incurable and potentially fatal condition [56]. As such, MRI techniques that can detect MI without the need for contrast injections are of potentially high diagnostic value.

Among these potential techniques is DWI wherein increases in ADC have been correlated with the presence of fibrosis [7, 8]. This is due to the increase in extracellular volume (ECV) in fibrosis compared with healthy myocardial tissue, which reduces the restriction of diffusive

motion. This mirrors the appearance of high ADC regions in the brain in the chronic stage of ischemic stroke.

Despite its potential value, cardiac DWI (cDWI) has not been widely adopted clinically. This is due in large part to the technical challenge associated with measuring diffusion in the presence of bulk physiological motion (as discussed in chapter 2.6.1). However, recent developments in cDWI pulse sequence design (including the technique described in Chapter 4) have improved the robustness of the technique and show promise in the clinical viability of cDWI.

3.2 Motion Induced Errors in Cardiac DWI

Bulk physiological motion can corrupt cDWI measurements (as mentioned in Chapter 2.6.1) and is particularly troublesome in cardiac applications for several reasons. First, because myocardial tissue is constantly displaced by both respiratory and cardiac motion, changes in position between paired cDWI acquisitions (i.e. inter-shot motion) can lead to mis-registration between measurements. However, this problem can be corrected or avoided by using image registration and/or by timing the imaging to occur at a fixed phase in both the cardiac and respiratory cycles. The cardiac phase can be fixed by monitoring an electrocardiogram (ECG) and timing the onset of imaging with a fixed trigger delay (TD) from the QRS complex. The respiratory phase can be fixed by either instructing the subject to hold their breath during the acquisition or by triggering the acquisition based on a semi-continuous image navigator (NAV) that monitors the position of the diaphragm using a short, one-dimensional view of the liver-lung interface. Other novel approaches have emerged for dealing with respiratory motion in cDWI including respiratory motion tracking with real time adjustments to the imaging location (slice following) [57] and retrospective image selection based on a quantitative similarity metric between images from the same respiratory phase [58].

Notably, intershot motion can be mitigated or corrected without modifying the DWI pulse sequence itself. However, intra-shot bulk motion induced errors in the acquired cDWI and presents a more challenging imaging problem. In the Stejskal-Tanner DWI experiment described in Figure 2.3, it is assumed that any spin displacement and subsequent signal phase is caused by diffusive motion. However, bulk physiological motion serves as an additional source of phase that can impact the DWI signal. This manifests as additional signal decay in images with b>0 which leads to overestimates of ADC. Furthermore, because bulk motion tends to greatly exceed diffusive motion in magnitude, this can result in unrecoverable signal saturation (i.e. drops to 0) particularly with moderate to high b-values (b>200s/mm^2).

The problem of intra-shot motion has spurred many technical developments in cDWI acquisition and reconstruction. The following section describes several previously described approaches that have inspired and enabled the novel approach described in this thesis.

3.3 Previous cDWI Approaches

3.3.1 Imaging During Cardiac Quiescence

Cardiac motion can be avoided entirely if the cDWI acquisition is timed precisely to a cardiac phase in which the LV remains stationary. This can occur to some degree at two points in the cardiac cycle: 1) at peak contraction (peak systole); and 2) at the end of passive left ventricular filling in late diastole (i.e. diastasis). While the peak systolic quiescent phase is typically <50ms, late diastolic quiescence can at times last over 100ms and thus theoretically accommodate a cDWI acquisition [59]. The timing of the diastolic quiescent period can be determined by acquiring a balanced steady state free precession (bSSFP) cine image set and visually determining the phase at which LV motion is minimized. This phase can inform the choice of ECG trigger delay to be used in the cDWI acquisition.

Unfortunately, in reality, the entire myocardium is seldom completely still during any single portion of diastasis and subtle, localized ventricular motion tends to persist in most, if not all time points. As a result, selecting a single phase that can accommodate a fully uncorrupted cDWI acquisition tends to be at best, challenging and at worst, impossible. Furthermore, diastolic timing is highly sensitive to changes in heart rate and thus can change over the course of a cDWI acquisition. Even subtle changes in heart rate can thus lead to changes that can impact a cDWI acquisition.

An approach called the temporal maximum intensity projection (TMIP) was proposed to combat the sensitivity of a cDWI acquisition to the ECG trigger delay [60]. While cDWI frequently includes signal averaging across multiple identical repetitions to improve SNR (Chapter 2.6.2), TMIP includes multiple repetitions with slight adjustments to the ECG trigger delay ($\Delta TD=10ms$) to acquire images with a range of trigger delays (~10 trigger delays). Instead of averaging the repeated acquisitions, a maximum intensity projection is performed at each voxel to remove the contribution of motion corrupted measurements that are necessarily lower in intensity. Principal component analysis (PCA) is then performed to improve image SNR in the absence of signal averaging. This approach is valuable in its simplicity and does not require any modification to the spin echo EPI DWI pulse sequence with monopolar diffusion encoding. However, it relies on the presence of a diastolic quiescent window that is large enough to accommodate the cDWI acquisition (even if the timing is not precisely known) and performs best in subjects with low and relatively stable heart rates. This approach is likely to face challenges in patients with high heart rates and arrhythmias and requires lengthy scans.

3.3.2 Constrained Reconstruction

Rather than performing a MIP, which discards all data at each voxel aside from the one with maximum signal intensity, a more judicious approach may conserve more of the acquired data

without including motion corrupted signals. We developed a Biophysically Constrained Reconstruction Algorithm (BCRA) that automatically detects and removes motion corrupted measurements [61]. This algorithm, which is depicted in Figure 3.1, measures a projection of the ADC along each acquired diffusion encoding direction (using a reference b0 image) and compares this value with the free diffusivity of water at human body temperatures (37°C), D_0=3mm^2/ms. D_0 reflects the diffusivity of totally unrestricted water molecules and thus should never be exceeded by water diffusing within human tissue. Any measurements yielding ADC>D_0 can be assumed to be corrupted by bulk motion and thus discarded from the reconstruction. We found that the use of this algorithm eliminated 44% of signals in cDTI acquisitions in healthy volunteers and dramatically reduced the resultant myocardial ADC values indicating improved bulk motion robustness (Figure 3.2).

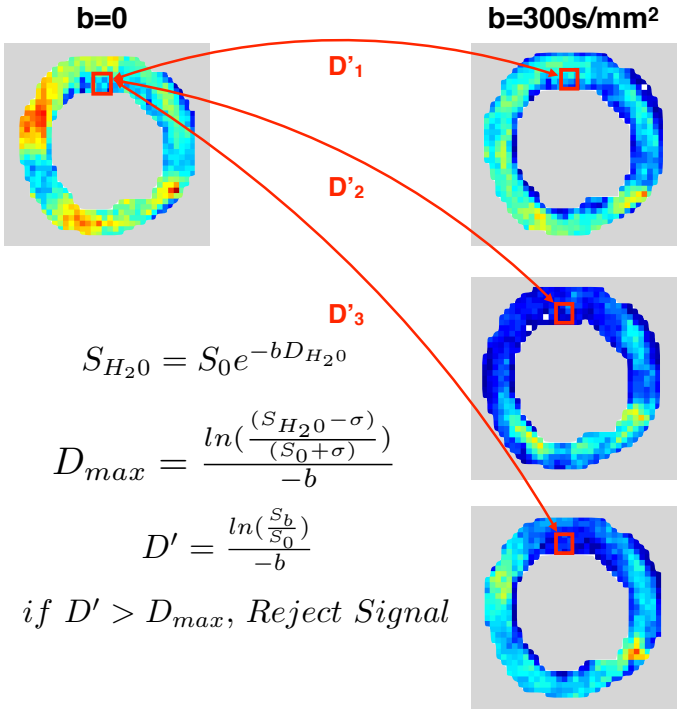

Figure 3.1: The BRCA reconstruction algorithm calculates single-projection estimates of diffusivity (D'_n) at each voxel and rejects data exceeds the maximum expected value (D_{max}) for freely diffusing water.

While the constrained reconstruction approach improves the efficiency of the cDWI acquisition compared with a TMIP strategy by maintaining all non-corrupted data, it still relies on the presence of a diastolic quiescent period. On its own, this approach is thus still subject to the drawbacks described in Chapter 3.3.1.

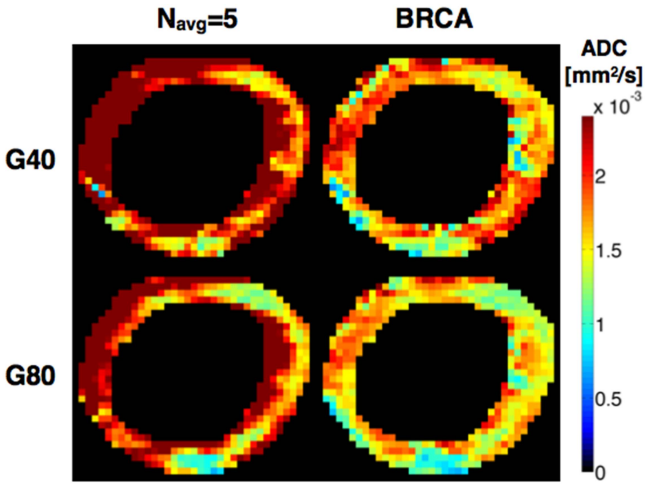

Figure 3.2: Typical ADC maps of the LV using signal averaging (left column) and the proposed biophysical reconstruction constraint algorithm (right column) using G_{max}=40mT/m (top row) and 80mT/m (bottom row). Deep red indicates voxels where ADC>(DH20+σ). Increasing G_{max} permitted a shorter diffusion encoding period which reduced motion sensitivity and BRCA successfully discarded corrupted data.

3.3.3 STEAM

Another pulse sequence strategy for combatting the bulk motion issue in cDWI is to replace the Stejskal-Tanner sequence with the STimulated Echo Acquisition Mode (STEAM) [62] technique. The STEAM approach exploits the periodicity of cardiac motion and divides the dephasing and rephasing diffusion encoding gradient lobes between two subsequent heart beats. After a specified ECG trigger delay, a saturation pulse is followed by a single diffusion encoding gradient and an additional saturation pulse to tip the magnetization back to the longitudinal axis where it is not subject to T_2^* decay. Then, following the QRS complex of the *next* heart beat and

the same trigger delay, the magnetization is tipped back down with a saturation pulse, rephased with a second diffusion encoding gradient and immediately acquired with a single shot EPI readout. This approach has several features that make it advantageous for cardiac applications. First, the long duration (one heart beat) between the two diffusion encoding gradients (termed the mixing time), leads to high b-values with very short gradient pulses. Because the DWI pulse sequence is only exceptionally bulk motion sensitive during the diffusion encoding gradients themselves, this substantially reduces the impact of intra-shot motion corruption and enables cDWI at nearly any cardiac phase. Furthermore, this substantially reduces the requirements for high performance gradient hardware that is important for efficient spin echo cDWI. The long mixing time in STEAM also increases the time scale and thus distance scale of the cDWI experiment compared with a spin echo approach. Data suggests that this increases the effective FA of myocardial tissue which can lead to smoother maps with higher precision [39].

However, STEAM also has several drawbacks compared with spin echo DWI. First, the use of a stimulated echo sequence has half the SNR of a spin echo sequence [63], which exacerbates the already low SNR in DWI and necessitates long scans with many signal averages. STEAM cDWI is also sensitive to myocardial strain and thus can only produce accurate ADC measurements at “sweet spots” in the cardiac cycle when strain effects cancel each other out. This can be corrected by using a bipolar STEAM sequence, but this removes the diffusion encoding effect during the mixing time and substantially reduces the efficiency and increases TEs. Additionally, while the ECG trigger delay can in principle time the two diffusion encoding gradients to occur at exactly the same cardiac phase, beat to beat timing changes can be a confounder. This can result in intra-shot b-value differences [64] or even un-refocused and thus unusable data points.

Nonetheless, STEAM cDWI has endured as an acceptably robust technique for quantifying cardiac microstructure and has facilitated several developments in our understanding of cardiac

structure. For example, this approach was used to identify the dynamics of myolaminar sheetlet orientations between cardiac phases in the healthy heart as well as a loss of this dynamic in patients with hypertrophic [15] and dilated cardiomyopathies [14, 16].

3.3.4 Motion Compensated Diffusion Encoding

It is possible to designing diffusion encoding gradient waveforms that encode diffusive motion but "ignore" physiological motion by employing the concept of motion compensated (MOCO) diffusion encoding. In describing this concept, it is useful to more formally describe the phase imparted by a diffusion encoding gradient as introduced in chapter 2.2.1. Considering a gradient waveform, G(t) and a spin with a time varying position, x(t), the accrued phase is given by:

$$\boldsymbol{\varphi}(\mathbf{t}) = \boldsymbol{\gamma} \int_{\mathbf{0}}^{\mathbf{t}} \mathbf{G}(\mathbf{t}') \cdot \mathbf{x}(\mathbf{t}') \mathbf{dt}' \tag{3.1}$$

The spin's position can also be described using a Taylor polynomial expansion:

$$\mathbf{x}(\mathbf{t}) = \mathbf{x_0} + \mathbf{t}\,\mathbf{x}'(\mathbf{t}) + \frac{\mathbf{t^2 x''(t)}}{\mathbf{2!}} + \cdots \tag{3.2}$$

Or, equivalently:

$$\mathbf{x}(\mathbf{t}) = \mathbf{x_0} + \mathbf{t} \cdot \mathbf{v} + \frac{\mathbf{t^2} \cdot \mathbf{a}}{\mathbf{2}} + \ \ldots \tag{3.3}$$

Where v and a are the spin's instantaneous velocity and acceleration, respectively. The accrued phase from G(t) can thus be described by:

$$\boldsymbol{\varphi}(\mathbf{t}) = \boldsymbol{\gamma} \int_{\mathbf{0}}^{\mathbf{t}} \mathbf{G}(\mathbf{t}') \cdot \mathbf{x_0}\, \mathbf{dt}' + \boldsymbol{\gamma} \int_{\mathbf{0}}^{\mathbf{t}} \mathbf{G}(\mathbf{t}') \cdot \mathbf{t}' \cdot \mathbf{v}\, \mathbf{dt}' + \frac{\boldsymbol{\gamma}}{\mathbf{2}} \int_{\mathbf{0}}^{\mathbf{t}} \mathbf{G}(\mathbf{t}') \cdot \mathbf{t}'^{\mathbf{2}} \cdot \mathbf{a}\, \mathbf{dt}' + \cdots \tag{3.4}$$

It is convenient to describe this in terms of gradient moments:

$$\boldsymbol{\varphi(t) = \mathbf{M_0 x_0} + \mathbf{M_1 v} + \frac{\mathbf{M_2 a}}{2} + \cdots} \quad 3.5$$

Where:

$$\mathbf{M_0} = \boldsymbol{\gamma} \int_0^{\mathbf{t}} \mathbf{G(t')dt'} \quad 3.6$$

$$\mathbf{M_1} = \boldsymbol{\gamma} \int_0^{\mathbf{t}} \mathbf{t'\, G(t')dt'} \quad 3.7$$

$$\mathbf{M_2} = \boldsymbol{\gamma} \int_0^{\mathbf{t}} \mathbf{t'^2 G(t')dt'} \quad 3.8$$

$$\mathbf{M_n} = \boldsymbol{\gamma} \int_0^{\mathbf{t}} \mathbf{t'^n G(t')dt'} \quad 3.9$$

Note that moments are typically defined for an entire gradient waveform (i.e. with t representing T_{Diff}, the end time of diffusion encoding).

It follows that the M_0 of the gradient waveform (i.e. its area) dictates the phase applied as a function of starting position and thus must be zero for all diffusion encoding gradient waveforms. Maintaining M_0=0 ensures that stationary spins are fully rephased as shown in Figure 2.3A. In the case of first order motion (constant velocity throughout the experiment), no phase will accrue if the diffusion encoding gradient waveform is designed such that M_0=M_1=0. This is achieved, for example, when a pair of bipolar gradient lobes is used. Furthermore, phase due to second order motion (constant acceleration during the diffusion encoding) can be nulled by designing the gradient waveform such that M_0=M_1=M_2=0. Higher order motion can thus be compensated by nulling higher order gradient moments. However, it has been shown that first and second order motion compensation is sufficient for largely eliminating the effects of cardiac motion in cDWI [19]. This implies that cardiac bulk motion can be approximated by a second order Taylor polynomial:

$$\mathbf{x_{Bulk}(t)} \approx \mathbf{x_0} + \mathbf{t \cdot v} + \frac{\mathbf{t^2 \cdot a}}{\mathbf{2}} \tag{3.10}$$

Critically, motion compensated diffusion encoding gradients still impart phase on diffusing spins and thus can still be used to characterize diffusion in moving tissues. To describe how motion compensated gradients can "ignore" physiological motion but still be sensitive to diffusion, it is useful to consider the sum of two sources of motion, bulk motion and diffusive motion (Figure 3.3):

$$\mathbf{x(t)} = \mathbf{x_{Bulk}(t)} + \mathbf{x_{Diff}(t)} \tag{3.11}$$

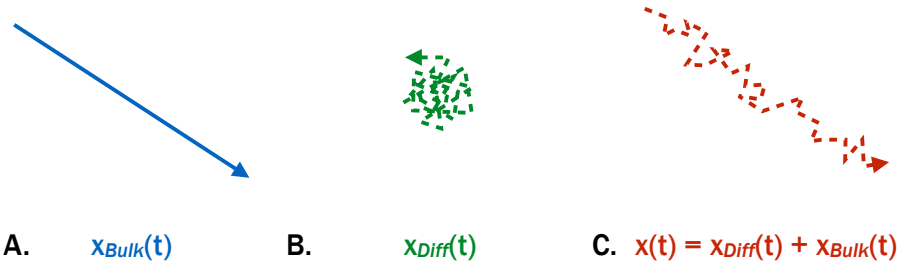

Figure 3.3: The motion of diffusing molecules confined in moving tissue can be broken down into two components of motion, bulk motion (A), and diffusive motion (B), which combine to form a hybrid pattern of motion (C). Motion compensated diffusion encoding is sensitive to diffusive motion, but not to bulk motion.

Because diffusion is an inherently random process, its Taylor expansion cannot be truncated as in the description of bulk cardiac motion. The phase due to G(t) and both components of motion is given by:

$$\boldsymbol{\varphi}(\mathbf{t}) = \boldsymbol{\gamma} \int_0^{\mathbf{t}} \mathbf{G}(\mathbf{t}') \cdot \mathbf{x_{Bulk}}(\mathbf{t}')\mathbf{dt}' + \boldsymbol{\gamma} \int_0^{\mathbf{t}} \mathbf{G}(\mathbf{t}') \cdot \mathbf{x_{Diff}}(\mathbf{t}')\mathbf{dt}' \tag{3.12}$$

Which simplifies when taking the Taylor expansion of the bulk motion component and making the assumption given in Equation **3.10**:

$$\boldsymbol{\varphi(t) = \mathbf{M_0 x_0} + \mathbf{M_1 v} + \frac{\mathbf{M_2 a}}{2} + \gamma \int_0^t \mathbf{G(t')} \cdot \mathbf{x_{Diff}(t')} dt'} \quad 3.13$$

Therefore, if the gradient waveform is designed such that M_0=M_1=M_2=0, the resultant phase is due only to the diffusive component of the motion:

$$\boldsymbol{\varphi_{MOCO}(t) = \gamma \int_0^t \mathbf{G(t')} \cdot \mathbf{x_{Diff}(t')} dt'} \quad 3.14$$

MOCO diffusion encoding with M_0=M_1=M_2=0 has proven to be a viable technique for encoding diffusion in the heart. Multiple designs have been proposed to achieve this design constraint including a twice refocused quadrapolar scheme [65] and a tri-polar gradient pair [66] for diffusion prepared cDWI as well as an asymmetric bipolar scheme [18] in spin echo single shot EPI cDWI.

Another motion compensation approach is the so called “diffusion prepared” strategy, which employs an additional saturation RF pulse after diffusion encoding to tip up the magnetization. This approach permits flexibility in the choice and speed of the readout and thus does not necessitate single shot EPI. Consequently, imaging with readouts such as balanced steady state free precession (bSSFP) or fast low angle shot (FLASH), which are less susceptible to image distortions are both possible. However, the increase in readout duration increases the temporal footprint of the pulse sequence within the cardiac cycle and thus is more likely to incur blurring due to cardiac motion or necessitate the use of segmented imaging, which extends acquisition durations. As a result, this technique is typically limited to diastolic imaging. Furthermore, this approach generally uses multi-shot readouts (i.e. only a portion of the image k-space is acquired per heartbeat) which improve image quality, but substantially increase scan times and can lead to mismatches is k-space where multiple shots are combined and is associated with ghosting artifacts.

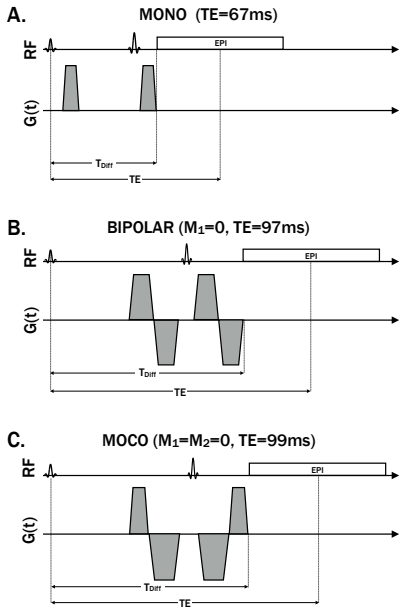

Figure 3.4: Typical monopolar (MONO) DWI pulse sequences (A) are highly sensitive to bulk motion. Motion sensitivity can be reduced by incorporating moment nulling in the design of the diffusion encoding gradient to achieve motion compensated diffusion encoding as in first order (BIPOLAR, B) and second order (MOCO, C) moment nulling, but also extend the minimum TE.

In this thesis, we adopt the MOCO approach for spin echo single shot EPI cDWI, which is fast and thus amenable to both systolic and diastolic imaging. It also is not susceptible to k-space mismatches as in multi-shot imaging. However, it is subject to all of the limitations of EPI as described in chapter 1.3.6, the most notable of which is image distortions. Furthermore, M_1 and M_2 nulling requires a multipolar gradient design that reduces the temporal efficiency of diffusion encoding and necessarily extends the pulse sequence TE and reduces the available SNR. In this thesis, an optimized strategy for designing MOCO diffusion encoding gradient waveforms with shorter TEs is described. This approach uses convex optimization to design the time optimal MOCO waveform for any protocol and is described at length in chapter 4.

3.3.5 EPI in the Heart

Because it typically relies on single shot EPI readouts, cDWI also presents image quality challenges that are independent from the diffusion encoding process. As mentioned in Section 1.3.6, several of the problems associated with EPI are exacerbated in cardiac applications, which can lead to poor image quality if not carefully considered. The two main issues in this regard are chemical shift and susceptibility-induced magnetical field inhomogeneities.

Because hyrogen nuclei contained in fat precess at a slightly lower frequency than those in water, fat tissue exhibits a linear shift in position relative to water in an effect called *chemical shift* [67]. This effect is accentuated in EPI, where large chemical shifts (on the order of tens of pixels) can occur in the phase encode direction. In cardiac EPI, this can cause fat from the chest wall, back, or elsewhere overlap with the myocardium and distort measurement. To combat this, fat saturation can be used to suppress the signal from fat [68] or RF pulses can be specifically designed to only excite water protons [69].

As mentioned in Section 1.3.6, sharp magnetic susceptibility gradients that arise at the interface between the heart and the air-filled lungs leads to magnetic field inhomogeneities that can distort EPI images. This can arise as distortions in the apparent myocardial shape or as signal voids near the posterior wall of the LV [70]. We deal with this issue in two ways: careful field shimming and keeping the EPI echo train as short as possible. Shimming refers to the process of making small adjustments to the B_0 magnetic field in order to maximize homogeneity within a localized region of interest [71]. The EPI readout can also be shortened to mitigate distortions from inhomogeneity. This can be accomplished by either shortening the duration of each k_y line or reducing the number of k_y lines to be read out. The duration of each readout line can be shortened by simply optimizing the readout gradient amplitudes (i.e. readout bandwidth) to minimize readout duration. Note that because gradient ramp times are limited by peripheral nerve stimulation (PNS) limitations, this does not always amount to using the maximum

available gradient amplitude. To reduce the number of k_y lines to be read out without reducing spatial resolution, the FOV can be reduced to include only the anatomy of interest. However, to avoid *aliasing* (i.e. the wrapping of anatomy from outside the FOV onto the image), signal from outside the FOV must be suppressed. This can be accomplished by using 2D-RF excitation [72] or by only refocusing signal within a limited region by playing a phase selective 180° pulse a slice selective excitation [73]. Furthermore, partial Fourier or parallel imaging techniques can be used to extrapolate a fully sampled dataset from an undersampled *k*-space (Chapter 1.3.6). The combination of a custom shim applied to a region tightly surrounding the heart and a short EPI readout can substantially reduce field inhomogeneity related EPI artifacts in the heart.

4 CONVEX OPTIMIZED DIFFUSION ENCODING

In this chapter, we develop an optimized approach for second order motion compensated diffusion encoding that permits DWI in the beating heart with greater temporal efficiency (and thus higher SNR) than existing motion compensated methods. This technique designs the diffusion encoding gradient waveform using a constrained convex optimization procedure that removes inefficient "dead time" from the DWI pulse sequences to achieve shorter TEs than previously described waveforms for the same b-values. We demonstrate that this technique, called Convex Optimized Diffusion Encoding (CODE), permits high-resolution spin echo cardiac DWI that is robust to cardiac motion. We also demonstrate the benefit of CODE gradients in DWI outside the heart in both neurological and liver applications. This work was previously published in *Magnetic Resonance in Medicine* in 2017: *Aliotta E, Wu HH, Ennis DB, Convex Optimized Diffusion Encoding (CODE) Gradient Waveforms for Minimum Echo Time and Bulk Motion Compensated Diffusion Weighted MRI. MRM; 2017 Feb;77(2):717-729.*

4.1 Abstract

Purpose: To evaluate convex optimized diffusion encoding (CODE) gradient waveforms for minimum echo time and bulk motion compensated diffusion weighted imaging (DWI).

Methods: Diffusion encoding gradient waveforms were designed for a range of b-values and spatial resolutions with and without motion compensation using the CODE framework. CODE, first moment (M_1) nulled CODE-M_1, and first and second moment (M_2) nulled CODE-M_1M_2 were used to acquire neuro, liver, and cardiac ADC maps in healthy subjects (N=10) that were compared respectively to monopolar (MONO), BIPOLAR (M_1=0) and motion compensated (MOCO, M_1+M_2=0) diffusion encoding.

Results: CODE significantly improved the SNR of neuro ADC maps compared with MONO (19.5±2.5 vs. 14.5±1.9). CODE-M_1 liver ADCs were significantly lower (1.3±0.1 vs. 1.8±0.3x$10^{-3}$$mm^2$/s, i.e. less motion corrupted) and more spatially uniform (6% vs. 55% ROI difference) than MONO and had higher SNR than BIPOLAR (SNR=14.9±5.3 vs. 8.0±3.1). CODE-M_1M_2 cardiac ADCs were significantly lower than MONO (1.9±0.6 vs. 3.8±0.3 x10^{-3} mm^2/s) throughout the cardiac cycle and had higher SNR than MOCO at systole (9.1±3.9 vs 7.0±2.6) while reporting similar ADCs (1.5±0.2 vs. 1.4±0.6x$10^{-3}$$mm^2$/s).

Conclusion: CODE significantly improved SNR for ADC mapping in the brain, liver and heart; and significantly improved DWI bulk motion robustness in the liver and heart.

4.2 Introduction

Diffusion weighted imaging (DWI) is a powerful MRI technique that measures the self-diffusion of water in a wide variety of soft tissues to provide directionally dependent microstructural information. In the brain, DWI is widely used to estimate the apparent diffusion coefficient (ADC) and is the clinical gold standard for detection of acute and chronic stroke. DWI has also demonstrated clinical value in the heart [6, 7, 74] and liver [75-78], but sensitivity to cardiac and respiratory bulk motion frequently contributes to large signal losses that confound diffusion weighted measurements in these regions[59, 60, 79-81].

DWI generally uses a Spin-Echo Echo Planar Imaging (SE-EPI) sequence with large, motion sensitizing, monopolar diffusion encoding gradients. Consequently, any bulk motion that occurs during diffusion encoding leads to substantial signal losses and elevated ADC measurements. These errors cannot be corrected retrospectively, which means they must be prevented with prospective changes to the DWI sequence.

Synchronizing the DWI acquisition with physiologic motion is a frontline approach to mitigating bulk motion artifacts. In the liver, bulk motion artifacts can be largely eliminated by implementing cardiac and respiratory triggering [82-84], but this significantly increases acquisition durations. In the heart, cardiac triggering and respiratory motion compensation (via triggering, breath holds, or navigators) are insufficient to suppress bulk motion artifacts [59, 60, 80]. Bulk motion sensitivity can be further reduced by shortening the temporal footprint of the diffusion encoding gradient, as in DWI with stimulated echoes[85].

Implementing motion compensated (MOCO) diffusion encoding gradient waveforms with nulled first and/or second-order gradient moments (M_1, M_2) can mitigate sensitivity to bulk motion. For example, velocity compensated diffusion encoding gradient waveforms (M_1=0) have been implemented in the liver and demonstrate improved ADC measurement reproducibility without respiratory or cardiac triggering [86, 87]. Similarly, velocity and acceleration compensated waveforms (M_1=M_2=0) have been shown to dramatically improve the bulk motion robustness of cardiac DWI [17-19].

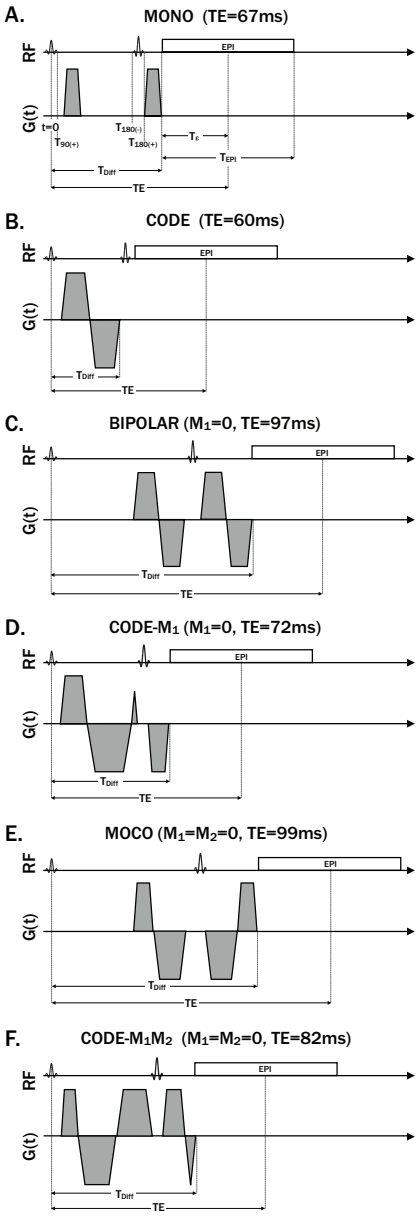

Figure 4.1: Diffusion encoding gradient waveforms for b=500s/mm^2 and T_ε=26.4ms (2x2mm spatial resolution with 300x300mm FOV, 1740Hz/px BW and GRAPPA acceleration factor 2) with (A) conventional monopolar, (B) CODE optimized monopolar, (C) conventional bipolar (velocity insensitive), (D) CODE-M_1, (E) conventional $M_1^+M_2$ nulled (velocity and acceleration insensitive), and (F) CODE-M_1M_2 encoding. CODE reduced the TE in all cases. Conventional encoding schemes (A, C, and E) all have deadtime that the CODE framework uses to minimize the diffusion encoding duration.

Conventional MOCO diffusion encoding is accomplished using a multi-polar gradient waveform that necessarily and significantly increases the TE compared to monopolar encoding, degrading SNR in the absence of bulk motion. Note, however, that the TE of SE-EPI DWI is dictated by the temporal footprint of: 1) the diffusion encoding gradient, and 2) the EPI readout (from its start to the TE). Consequently, there is always dead time between the excitation and refocusing pulses (Figure 4.1-A,C,E). This dead time increases with longer EPI readouts (i.e higher spatial resolution, lower bandwidth, etc.). In principle, this deadtime can be filled with diffusion encoding gradients such that less diffusion encoding is needed after the refocusing pulse, consequently decreasing the TE.

Herein, we present a versatile optimization framework to redesign the diffusion encoding gradient waveforms to be M_1 or M_1+M_2 compensated in order to mitigate sensitivity to bulk motion artifacts and eliminate dead time. This approach significantly shortens the TE in SE-EPI DWI, which improves the DWI signal-to-noise (SNR). The resulting diffusion encoding gradients are necessarily asymmetric about the refocusing pulse and closed-form gradient waveform designs that conform to pulse sequence constraints (i.e. the diffusion encoding gradients must be off during RF pulses and the EPI readout, for which the specific timing is dictated by the field of view, readout bandwidth, spatial resolution, etc.), diffusion encoding gradient waveform constraints (b-value, M_1, and M_2), and hardware constraints (maximum gradient amplitude and slew rate) are difficult, if not impossible, to determine. Therefore, a mathematical optimization technique is needed.

Convex optimization (CVX) is a proven method for minimizing gradient durations while conforming to pulse sequence and hardware constraints [88, 89]. The objective of this study was to design and implement a Convex Optimized Diffusion Encoding (CODE) framework that can optimize gradient waveforms with any b-value and gradient moment-nulling properties in order to simultaneously achieve the shortest possible TE and robustness to bulk motion artifacts.

4.3 Theory

CVX was applied to design diffusion encoding gradient waveforms that minimize the TE for any b-value with no constraint on the gradient shape or symmetry while conforming to all pulse sequence, diffusion encoding (gradient moment) and hardware constraints, which are defined as follows:

4.3.1 Pulse Sequence Constraints

The diffusion encoding gradients must be off during both periods of RF activity (excitation and refocusing pulses) and during the EPI readout. Therefore, the diffusion encoding gradient design must conform to:

$$G(0 \leq t \leq T_{90(+)}) = 0 \quad 4.1$$

$$G(T_{180(-)} \leq t \leq T_{180(+)}) = 0 \quad 4.2$$

$$G(T_{Diff} \leq t \leq TE) = 0 \quad 4.3$$

Where diffusion encoding begins at t = $T_{90(+)}$ (immediately after excitation and EPI correction lines), the refocusing pulse is played when $T_{180(-)} \leq t \leq T_{180(+)}$, and the EPI readout occurs when $T_{Diff} \leq t \leq T_{Diff}+T_{EPI}$ (where T_{EPI} is the EPI readout duration) (Figure 4.1A). The duration of the EPI readout gradient needed to reach the center k-space line is given by the time-to-echo, T_{ε}, where $T_{\varepsilon}=0.5*T_{EPI}$ for full-Fourier imaging.

4.3.2 Gradient Moment Constraints

The optimized diffusion encoding gradient waveform must have a nulled M_0 and, as required, nulled M_1 or M_1+M_2 at the end of diffusion encoding (t = T_{Diff}. Figure 4.1):

$$M_0 = \int_0^{T_{Diff}} G(t)dt = 0 \quad (4.4)$$

$$M_1 = \int_0^{T_{Diff}} tG(t)dt = 0 \quad (4.5)$$

$$M_2 = \int_0^{T_{Diff}} t^2G(t)dt = 0 \quad (4.6)$$

The imaging gradients played during the EPI readout have zero net M_0, and negligible M_1, and M_2 at the TE (<1% of typical moments from MONO). Therefore if they are nulled at t=T_{Diff}, they are also effectively nulled at t=TE. The moments of the slice select gradient, which are also negligible (<0.5% of typical diffusion encoding gradient moments for MONO) with respect to the diffusion encoding gradients, are not considered in this optimization.

4.3.3 Hardware Constraints

The gradient waveform design must adhere to gradient hardware limitations on maximum gradient amplitude (G_{max}) and slewrate (SR_{max}). This leads to the following constraint terms in the optimization:

$$G(t) \leq G_{max} \quad (4.7)$$

$$\dot{G}(t) \leq SR_{max} \quad (4.8)$$

4.3.4 Maximizing b-value

The magnitude of diffusion weighting in a DWI acquisition is characterized by the b-value (b), which is given by:

$$b = \gamma^2 \int_0^{T_{Diff}} F(t)^2 dt \tag{4.9}$$

where:

$$F(t) = \int_0^t G(\tau) d\tau \tag{4.10}$$

G(t) is the gradient amplitude as a function of time, T_{Diff} is the time at the end of the diffusion encoding gradient waveform and γ is the gyromagnetic ratio of ^{1}H. The time t=0 corresponds with the center of the excitation pulse.

The CODE framework begins by determining the maximum b-value for a fixed TE, then subsequently reducing the TE until the maximum b-value is equivalent to the target b-value (b_{target}). However, the b-value (Eqn. **4**.**9**) is a convex functional of G(t) (i.e. its second variation is positive definite[90]) and therefore does not contain a single maximum that can be determined with CVX. In addition, Eqn. **4**.**9** is not a unique functional of G(t), which means multiple waveforms can produce the same b-value (e.g., +G(t) and -G(t) have the same b-value). Therefore, to facilitate convex optimization, the objective function can be reformulated by defining the function, β:

$$\beta = \int_0^{T_{Diff}} F(t) dt \tag{4.11}$$

The magnitude of β corresponds directly with the b-value, but it is a concave functional of G(t) (i.e. its second variation is negative definite[90]); therefore it contains a maximum that can be determined using CVX. Consequently, the gradient waveform G(t) that produces the maximum β (and thus the maximum b-value) can be determined using the following objective function:

$$G(t) = \underset{G}{\operatorname{argmax}}\, \beta(G) \tag{4.12}$$

Subject to the constraints in Eqn. **4.1**-4.8. G(t) is defined discretely on t = m•dt where dt is the temporal resolution of the optimization and m is an integer between 1 and T_{Diff}/dt.

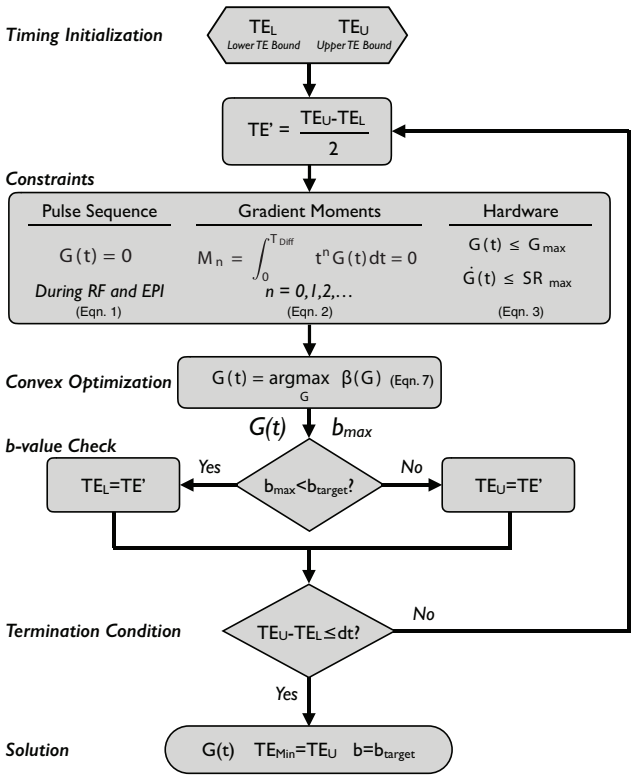

*Figure 4.2: Flow chart describing the CODE optimization algorithm. The time optimal solution is determined by finding the minimum TE for which a gradient waveform exists that is consistent with all constraints and can achieve the target b-value (b_{target}). This problem is solved through successive binary searches to divide the TE search space with each call of the convex solver. Upper and lower limits on TE (TE_U and TE_L) are first defined to initiate the optimization. TE_U is defined by the TE of the non-optimized sequence with the desired gradient moments. TE_L is defined by the TE of an equivalent spin echo sequence (i.e without diffusion encoding gradients), which has a minimum TE of $2•(0.5•T_{180}+T_{\varepsilon})$. The function β is defined in Eqn. **4.11** and is directly related to the b-value (i.e. maximizing β also maximized b-value), but is compatible with convex optimization.*

4.3.5 Solution Strategy

The time optimal solution is determined by finding the minimum TE for which a gradient waveform exists that is consistent with all constraints (Eqns. **4**.**1**-4.8) and has $b_{max} \geq b_{target}$. This problem can be efficiently solved through successive binary searches that divide the TE search space with each iteration of Eqn. **4**.**12**, similar to the method described by Hargreaves et al[88]. The search algorithm is shown in a flow chart (Figure 4.2) and is provided as a downloadable MATLAB function (http://mrrl.ucla.edu/resources/code-optimization/). Upper and lower limits on TE (TE_U and TE_L) are first defined to initialize the optimization. TE_U is defined by the TE of the non-optimized sequence with the desired gradient moments (i.e monopolar for M_0=0, bipolar for M_0=M_1=0, modified bipolar [18] for M_0=M_1=M_2=0). TE_L is defined by the TE of an equivalent spin echo sequence (i.e without diffusion encoding gradients), which has a minimum TE of $2 \bullet (0.5 \bullet T_{180} + T_\varepsilon)$.

4.4 Methods

4.4.1 Diffusion Encoding Gradient Waveform Design

In order to evaluate the reduction in TE when using CODE, diffusion encoding gradient waveforms were designed for a range of b-values (100-1000s/mm^2) and T_ε (10-60ms); corresponding to roughly 0.5-3.0mm in plane resolution, with full Fourier symmetric k-space coverage) using the following designs: 1) monopolar (MONO, Figure 4.1A); 2) CODE with M_0=0 (CODE, Figure 4.1B), 3) velocity compensated (M_0=M_1=0) bipolar (BIPOLAR, Figure 4.1C); 4) velocity compensated (M_0=M_1=0) CODE (CODE-M_1, Figure 4.1D); 5) velocity and acceleration compensated (M_0=M_1=M_2=0) modified bipolar (MOCO, Figure 4.1E); 6) velocity and acceleration compensated CODE (CODE-M_1M_2, Figure 4.1F).

All diffusion encoding gradient waveforms were designed for a 3T MRI scanner (Prisma, Siemens, Erlangen, Germany) with high performance gradients (G_{max}=80mT/m and SR_{max}=200T/m/s). To limit peripheral nerve stimulation during diffusion encoding, the gradient performance was limited to G_{max}=74mT/m and SR_{max}=50T/m/s. All optimizations were done in MATLAB (Mathworks, Natick, MA, USA) using the CPLEX linear solver (IBM, Armonk, NY, USA) with the YALMIP toolbox [91] and used time-step dt=100μs to maintain reasonable computation times (<5min). Shorter time-steps increase computational demand without significantly reducing echo times.

4.4.2 Concomitant Field Correction

The application of a gradient field leads to the production of concomitant magnetic fields as described by the higher order terms of Maxwell's equations [92-95]. Because DWI typically employs large gradient amplitudes, these fields can have a notable effect and lead to erroneous DWI pixel values, distorted images, and consequently problematic ADC maps. Concomitant fields are not typically an issue in DWI because they are cancelled out when diffusion encoding gradient waveforms are identical on either side of a refocusing pulse. However, because the CODE gradient waveforms are not identical on either side of the refocusing pulse, the concomitant fields must be accounted for. Therefore, a prospective approach that has been used in PC-MRI [96] and DWI [96, 97] was implemented in the CODE sequence. Phase variations due to concomitant fields were linearly approximated on the scanner for the direction-specific diffusion encoding gradient waveform and were corrected by adding a gradient magnitude offset to the diffusion encoding gradient waveform along the x, y and z axes. Further detail on the correction can be found in Ref. [96].

4.4.3 In Vivo Protocols

DWI protocols were designed for neuro (T_ε=27.1ms, $T_{90(+)}$=5.8ms, T_{180}=4.3ms), liver (T_ε=26.4ms, $T_{90(+)}$=5.3ms, T_{180}=4.3ms) and cardiac (T_ε=25.3ms, $T_{90(+)}$=5.4ms, T_{180}=4.3ms) acquisitions with and without CODE. The specific parameters are defined in Table 1. All acquisitions included diffusion encoding along three oblique orthogonal directions. In the cardiac protocols, FOV reduction was performed in the phase encode direction using phase cycling between the excitation and refocusing RF pulses[73].

	Neuro		Liver			Cardiac		
	MONO	CODE	MONO	BIPOLAR	CODE-M_1	MONO	MOCO	CODE-M_1M_2
TE (ms)	75	64	67	97	72	65	93	76
TR (ms)	5000ms		1000ms			1 Heartbeat		
Resolution (mm)	1.6x1.6x3.0		2.0x2.0x7.0			1.5x1.5x5		
FOV (mm)	220x220		300x300			200x160		
BW (Hz/px)	1450		1740			2000		
b (s/mm^2)	0, 1000		0, 500			0, 350		
Fat Suppression	None		SPAIR [98]			Water Excitation		
Common	Parallel Imaging Acceleration (GRAPPA[35]) Factor 2, Full-Fourier k-space sampling							

Table 4.1 Specific imaging parameters used in the neuro, liver and cardiac protocols are shown. Interleaved multi-slice imaging was used in the liver protocols. Reduced FOV imaging was used in the cardiac protocols using phase cycling between the 90° and 180° pulses. Additional fat suppression was achieved in the cardiac protocols using spatially selective saturation bands.

4.4.4 Concomitant Field Evaluation

To evaluate the performance of the concomitant field correction strategy, DWI were acquired in a uniform water phantom along seven directions (x,y,z,xy,xz,yz,xyz) using MONO diffusion

encoding as a reference for comparison to both CODE-M_1M_2 with and without the concomitant field correction (using the cardiac DWI protocols). Maps from single-direction projections of the ADC were reconstructed independently for each direction, in addition to a composite ADC map (from all directions).

4.4.5 Phantom Validation

All protocols were performed in a polyvinylpyrrolidone diffusion phantom (High Precision Devices, Boulder, CO, USA) containing thirteen regions with varying diffusivities. The ADC was reconstructed for each protocol and the mean value was calculated within each of the thirteen regions. Mean ADCs obtained with the neuro (MONO and CODE with b=1000mm^2/s), liver (MONO and CODE-M_1 with b=500mm^2/s) and cardiac protocols (MONO and CODE-M_1M_2 with b=350mm^2/s) were compared using linear regression analysis.

4.4.6 In Vivo Acquisitions

MRI examinations were performed on healthy volunteers who provided signed statements of informed consent prior to each MRI exam. All studies were in compliance with the local IRB, state, and federal guidelines. All imaging was performed on a 3T MRI scanner (Prisma, Siemens, Erlangen, Germany).

4.4.7 Neuro DWI

DWI of the brain were acquired in healthy volunteers (N=10) in a single axial slice with the neuro MONO and CODE protocols. All acquisitions included three discarded TRs to reach steady state and were repeated ten times for SNR analysis (scan time: 3min 40sec).

ADC maps were reconstructed for each of the ten repetitions of MONO and CODE using linear least squares. A voxel-wise SNR map was generated by dividing the mean ADC at each

voxel by the standard deviation (across the ten repetitions). The global mean SNR was then calculated within the brain for CODE and MONO and compared across the ten subjects.

4.4.8 Liver DWI

Breath held liver DWI were acquired in healthy volunteers (N=10) using the MONO, BIPOLAR and CODE-M_1 liver protocols with three averages. Cardiac triggering was not used. Slice interleaved imaging was used to acquire four slices per TR and provide coverage of the superior and inferior liver in two breath holds (8 slices). Additional non-diffusion weighted (b=0) images were also acquired separately with four repetitions (three averages per repetition) for SNR analysis. All acquisitions included three discarded TRs to reach steady state (scan time: 15s per breath hold).

ADC maps were reconstructed for MONO, BIPOLAR, and CODE-M_1 acquisitions using linear least squares. Four regions of interest (ROI) were manually defined in homogeneous liver regions (free of vessels) in the lateral left lobe (LL), medial left lobe (ML), superior right lobe (SR) and inferior right lobe (IR). The mean ADC was calculated within each ROI for each acquisition. To identify motion corruption, the mean ADCs in the three superior ROIs (ADC_{LL}, ADC_{ML} and ADC_{SR}) were compared with that in IR (ADC_{IR}, most inferior and least influenced by cardiac motion).

SNR maps were then calculated from the b=0 images for MONO, BIPOLAR and CODE-M_1 (voxel-wise standard deviation divided by mean signal across repetitions). The mean SNR was calculated within the IR ROI and compared between MONO, BIPOLAR and CODE-M_1 across the ten subjects.

4.4.9 Cardiac DWI

Cardiac MRI examinations were performed in healthy volunteers (N=10). First, the timing of end systole (T_{SYS}, the time-point with minimum ventricular volume) and early diastole (T_{DIA}, the first time-point after rapid filling) were visually determined for each subject using high temporal resolution (20ms) balanced steady state free precession (bSSFP) CINE imaging.

Breath held DWI images were then acquired using the MONO and CODE-M_1M_2 cardiac protocols. Both protocols were acquired with ECG triggering delayed to the following eight subject-specific cardiac phases: $0.5T_{SYS}$, $0.75T_{SYS}$, T_{SYS}, $T_{SYS}+0.25(T_{DIA}-T_{SYS})$, $T_{SYS}+0.5(T_{DIA}-T_{SYS})$, T_{DIA}, $T_{DIA}+0.25(RR-T_{DIA})$, and $T_{DIA}+0.5(RR-T_{DIA})$, where RR is cardiac cycle duration. Each acquisition included three discarded TRs to reach steady state and three repetitions to improve SNR (scan time: 15 heartbeats or ~15 seconds).

ADC maps were reconstructed for each cardiac phase for both MONO and CODE-M_1M_2 cDWI using linear least squares. Masks were manually defined to isolate the LV myocardium at each cardiac phase based on the non-diffusion weighted images. The mean ADC was calculated within the LV for each phase and compared with the diffusivity of free water at 37°C ($3.0x10^{-3}mm^2/s$, a thermodynamic upper bound for soft tissue ADC) using a one-sided comparison. Motion corrupted measurements were identified by voxels in which the reported ADC exceed $3.0x10^{-3}mm^2/s$. The percentage of LV voxels with motion corruption was calculated for MONO and CODE-M_1M_2 at each cardiac phase and compared across the ten volunteers.

An additional cohort of volunteers (N=10) were scanned using MONO, MOCO, and CODE-M_1M_2 at a single systolic phase ($0.5T_{SYS}$) for SNR and ADC comparisons between methods. Two acquisitions were obtained for each technique in separate breath holds: 1) the cardiac ADC mapping protocol with three averages, and 2) four repetitions of the non-diffusion weighted (b=0) images (three averages per repetition). ADC maps were reconstructed from the DWI sets as described above. SNR maps were generated from the b=0 images by dividing the mean

signal intensity at each voxel by the standard deviation (across the four repetitions). The mean ADC, ADC standard deviation (SD), and mean SNR were then calculated within the septum and compared between MONO, MOCO and CODE-M_1M_2 across the ten subjects. Measurements were limited to the septum to remove SNR variations caused by field inhomogeneity in the posterior wall near the lung.

4.4.10 Statistical Analysis

All data were first tested for normality using a skewness and kurtosis test for normality. Variability between groups (e.g. between methods or liver ROIs) was then tested using one-way analysis of variance (ANOVA) (for normal distributions) or Kruskal-Wallis (for non-normal distributions). Variations across cardiac phases were tested using repeated measures ANOVA (normal distributions) or Friedman's test (non-normal distributions). If ANOVA yielded significant differences ($P<0.05$), pairwise comparisons were made between groups (e.g MONO vs. CODE) using paired t-tests (normal distributions) or Wilcoxon signed-rank tests (non-normal distributions) at a 0.05 significance level. Multiple comparisons (i.e. between techniques, cardiac phases and liver ROIs) were evaluated using post hoc Holm-Sidak correction [99].

4.5 Results

4.5.1 CODE Optimization

Convex optimization reduced the TE for all diffusion encoding strategies, i.e. CODE, CODE-M_1, and CODE-M_1M_2 across a wide range of b-values and EPI readouts (Figure 4.3). The minimum TE for each strategy over a range of b-values and T_ε are plotted in Figure 4.3. The TE reductions achievable with CODE increased with both longer T_ε (i.e high spatial resolution) and large b-values. Mean TE reductions from CODE, CODE-M_1 and CODE-M_1M_2 were 9.1%, 26.5%

and 18.4% respectively compared to MONO, BIPOLAR and MOCO. The maximum respective reductions were 17.2%, 32.6% and 28.0%. Example waveforms for each encoding strategy are shown in Figure 1 for b-value=500 s/mm^2 and T_ε=26.4ms (~2x2mm^2 resolution, equivalent to the liver protocols).

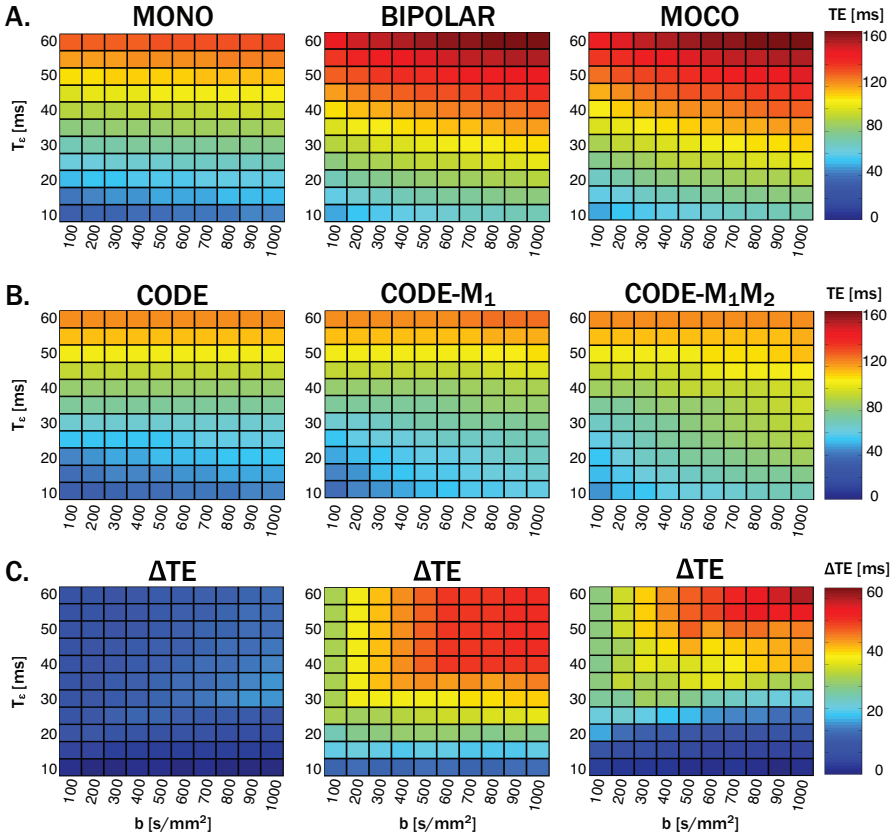

Figure 4.3: Minimum TE for a range of b-values and EPI readout times to echo (T_ε) using (A) conventional monopolar (MONO), BIPOLAR, or MOCO diffusion encoding and (B) CODE, CODE-M_1, and CODE-M_1M_2 gradient waveforms. (C) TE reduction (ΔTE) achieved using the CODE framework. ΔTE was greater for motion compensated encoding and increased with increasing T_ε.

For the neuro protocol (T_ε=27.1ms, b=1000s/mm^2) the MONO waveform requires TE=75ms whereas CODE had TE=67ms (11% reduction). For the liver protocol (T_ε=26.4ms, b=500s/mm^2) the M_1 compensated BIPOLAR waveform requires TE=97ms whereas CODE-M_1 had TE=72ms (26% reduction). For the cardiac protocol (T_ε=25.3ms, b=350s/mm^2) the traditional M_1M_2

compensated (MOCO) waveform requires TE=93ms whereas CODE-M_1M_2 had TE=76ms (18% reduction).

4.5.2 Concomitant Field Corrections

The effect of the prospective concomitant field correction is shown in Figure 4.4. With MONO encoding (no concomitant fields, no correction) the ADC projections were spatially homogeneous and ADC values were distributed tightly about the free diffusivity of water at room temperature (D_{H20}≈2.1x$10^{-3}$$mm^2$/s) for all diffusion encoding directions. Without the concomitant field correction, CODE-M_1M_2 encoding resulted in a large bias and direction-dependent spatial heterogeneity in the ADC projections. The concomitant field correction significantly reduced the error and spatial variation of the ADC projections for all directions. Mean ADC projections measured across all directions by CODE-M_1M_2 were significantly different from MONO without the correction (4.3±2.2x$10^{-3}$$mm^2$/s vs. 2.1±0.005x$10^{-3}$$mm^2$/s, p=0.01), but were not different with the correction (2.1±0.004x$10^{-3}$$mm^2$/s vs. 2.1±0.005x$10^{-3}$ mm^2/s, p=N.S.).

4.5.3 Phantom Validation

There was good agreement between MONO and CODE for all three sets of protocols across the range of diffusivities in the diffusion phantom (range: 0.3x$10^{-3}$$mm^2$/s to 2.1x$10^{-3}$$mm^2$/s). Regression analysis yielded the following linear fits for each pair of protocols: Neuro – ADC_{CODE}=0.92*ADC_{MONO} + 0.06x10^{-3} mm^2/s (R^2=0.997), *Liver* – $ADC_{CODE\text{-}M1}$=0.94*ADC_{MONO} + 0.07x10^{-3} mm^2/s (R^2=0.99), *Cardiac* – $ADC_{CODE\text{-}M1M21}$=1.02*ADC_{MONO} + 0.21x10^{-3} mm^2/s (R^2=0.92).

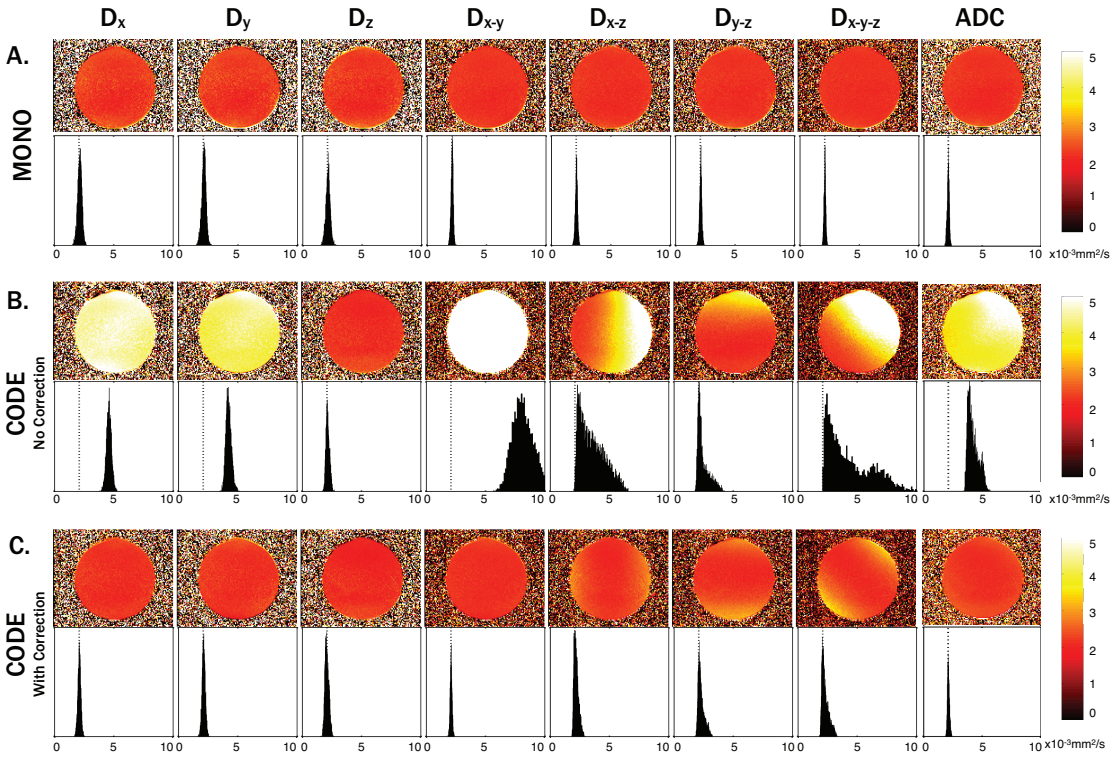

Figure 4.4: Measured diffusivity maps and histograms along each gradient direction (D_i) and the final ADC maps (rightmost column) for (A) MONO, (B) CODE-M_1M_2 without concomitant field corrections, and (C) CODE-M_1M_2 with concomitant field corrections in a uniform water phantom. Without the correction, the CODE-M_1M_2 gradients produce large concomitant fields that lead to errors (bias and heterogeneity) in the ADC maps that is also evident in the histograms. The concomitant field correction largely eliminates this effect. The dotted line indicates ADC=2.1x10^{-3}mm^2/s (the "true" value as determined from MONO encoding).

4.5.4 Neuro DWI

The results from the neuro acquisitions are shown in Figure 4.5. CODE encoding reduced the TE by 11% as compared to MONO (from 75ms to 67ms), which resulted in ADC maps with higher SNR (Figure 4.5C). The mean global SNR of the ADC maps were 35% higher with CODE than MONO (19.5±2.5 vs 14.5±1.9, P<0.0001) across the ten volunteers scanned.

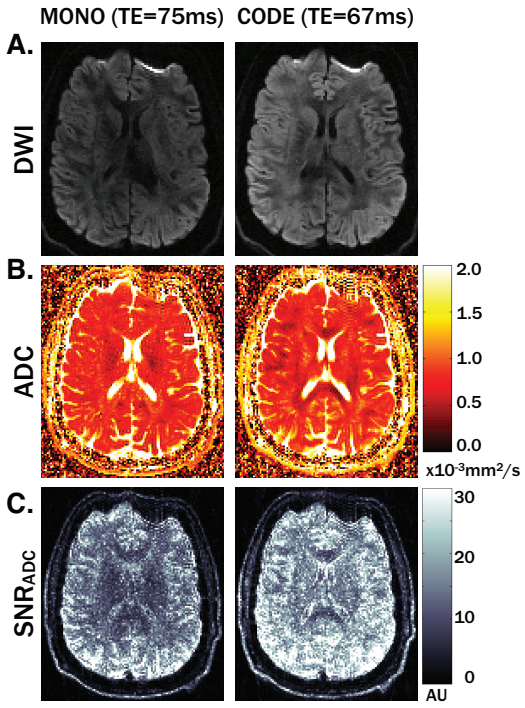

Figure 4.5: (A) Diffusion weighted images of the brain from a typical healthy volunteer are shown with b=1000s/mm^2 using MONO (TE=75ms) and CODE (TE=67ms) encoding. The 12% TE reduction leads to brighter DWI and (B) qualitatively improved ADC maps. (C) The SNR of the ADC maps measured voxel-wise from ten repeated experiments per subject, show increased SNR. ADC SNR throughout the brain was increased by 35% on average across ten volunteers with CODE encoding.

4.5.5 Liver DWI

Results from the liver acquisitions are shown in Figure 4.6. MONO encoding resulted in large bulk motion signal dropouts in portions of the liver that are closest to the heart (i.e superior regions and left lobe, Figure 4.6A). These signal dropouts lead to large overestimates of the ADC and were eliminated with BIPOLAR and CODE-M_1 encoding (Figure 4.6B). Across the ten volunteers the mean ADC measured in left-most ROIs (ADC_{LL} and ADC_{ML}) were significantly higher than in the most inferior ROI (i.e least influenced by cardiac motion, ADC_{IR}) with MONO (Table 4.2, both $P<0.004$). There was no significant difference between ADC_{IR} and ADC_{SR} with

MONO (Table 4.2, P=N.S.). Notably, there were no significant differences between the four BIPOLAR or CODE-M_1 ROIs (Table 4.2). With MONO the maximum difference between mean ADCs across the four ROIs normalized by the mean ADC in the IR (i.e. $(ADC_{LL}-ADC_{IR})/ADC_{IR}$) was 55%; this decreased to 41% with BIPOLAR and 6% with CODE-M_1. The mean ADC was also lower with CODE-M_1 than MONO in a pairwise comparison to MONO in three of the four ROIs (ADC_{LL}, ADC_{ML} and ADC_{SR}, all $P<0.006$). ADC_{LL} and ADC_{ML} were lower with BIPOLAR than MONO ($P<0.006$), but there was no significant difference in ADC_{SR}. There were no significant differences between techniques in ADC_{IR}.

CODE-M_1 and MONO both had significantly higher SNR than BIPOLAR (Figure 4.6E) (CODE-M_1: 14.9±5.3 and MONO: 17.5±6.8 vs BIPOLAR: 8.0±3.1, both $P<0.003$). SNR was not significantly different between MONO and CODE-M_1.

	ADC_{LL}	ADC_{ML}	ADC_{SR}	ADC_{IR}
MONO	2.1 ± 0.3†	2.0 ± 0.5†	1.5 ± 0.3	1.5 ± 0.3
BIPOLAR	1.5 ± 0.6*	1.2 ± 0.4*	1.3 ± 0.4	1.2 ± 0.5
CODE-M_1	1.3 ± 0.2*	1.2 ± 0.1*	1.3 ± 0.2*	1.3 ± 0.2

Table 4.2: Mean ADC values measured in the four liver ROIs (LL - Left lobe, ML - Middle lobe, SR - Superior right, and IR - Inferior right).† Indicates mean ADCs that are significantly different from ADC_{IR} ($p<0.003$). * Indicates that mean ADCs are significantly different from MONO.

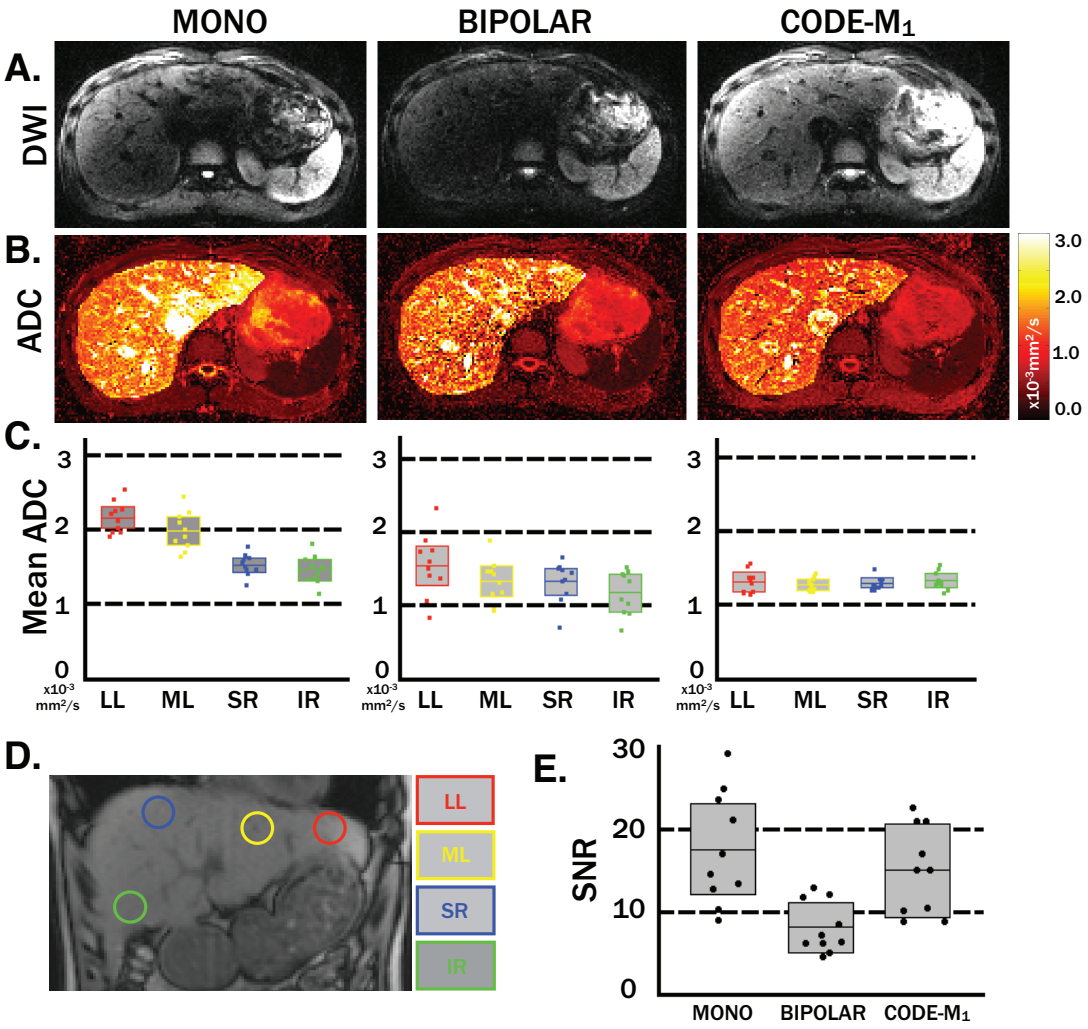

*Figure 4.6: (A) Axial diffusion weighted images of the liver from a typical healthy volunteer are shown with b=500s/mm^2 using MONO, BIPOLAR and CODE-M$_1$. (B) Signal dropouts caused by physiological motion lead to elevated ADC maps, but are largely eliminated with CODE-M$_1$. (C) Mean±95%CI ADC values within the four ROIs across ten volunteers. The MONO ADC values are higher close to the heart (LL - left lobe and ML - middle lobe) where cardiac-induced bulk motion is greatest. CODE-M$_1$ encoding leads to more spatially homogeneous ADC maps. (D) Approximate regions chosen for the four ROIs are shown in the coronal view. (E) Mean±95%CI SNR values within the IR ROI across the ten volunteers for MONO, BIPOLAR and CODE-M$_1$ encoding. CODE-M$_1$ had greater SNR than BIPOLAR while maintaining motion robustness (*P<0.0002, †P<0.02).*

4.5.6 Cardiac DWI

Results from the cardiac DWI acquisitions are shown in Figure 4.7 and Figure 4.8. Qualitatively, Figure 4.7A demonstrates acceptable DWI when using CODE-M_1M_2, but unacceptable bulk-motion signal losses when using MONO in most cardiac phases. Mean ADC values were significantly corrupted (>3.0x$10^{-3}$$mm^2$/s) for 50% of the cardiac phases with MONO ($p<0.004$) and 0% of the cardiac phases with CODE-M_1M_2 (p=N.S.) (Figure 4.7B). CODE-M_1M_2 resulted in significantly lower mean ADCs (1.9±0.3x$10^{-3}$$mm^2$/s vs. 3.8±0.6x$10^{-3}$$mm^2$/s, $p<0.007$) and fewer motion corrupted voxels (14% vs 67%, $p<0.0006$) than MONO in 100% of cardiac phases (Figure 4.7B and Figure 4.7C).

Figure 4.8A demonstrates the improved motion robustness of both MOCO and CODE-M_1M_2 compared with MONO and also the SNR gains of CODE-M_1M_2 compared with MOCO. Mean ADCs were not different between CODE-M_1M_2 and MOCO (1.5x10^{-3}±0.2mm^2/s vs 1.4x10^{-3}±0.6 mm^2/s, P=N.S.) (Figure 4.8B), but CODE-M_1M_2 had significantly lower ADC variance than MOCO (mean SD = 0.7x10^{-3}±0.3 vs. 0.9x10^{-3}±0.3, $P<0.002$) (Figure 4.8C) and significantly higher SNR (9.1±3.9 vs 7.0±2.6, $P<0.02$) (Figure 4.8D). MONO had significantly higher SNR (mean SNR = 11.0±5.9) than MOCO (mean SNR = 7.0±2.6, $P<0.002$), and slightly higher SNR than CODE-M_1M_2 (mean SNR = 9.1±3.9, P=N.S.), but reported corrupted ADC values that were significantly higher than CODE-M_1M_2 and MOCO (mean ADC = 4.4x10^{-3}±1.6mm^2/s, $P<1x10^{-5}$ for MOCO and CODE-M_1M_2) (Figure 4.8B).

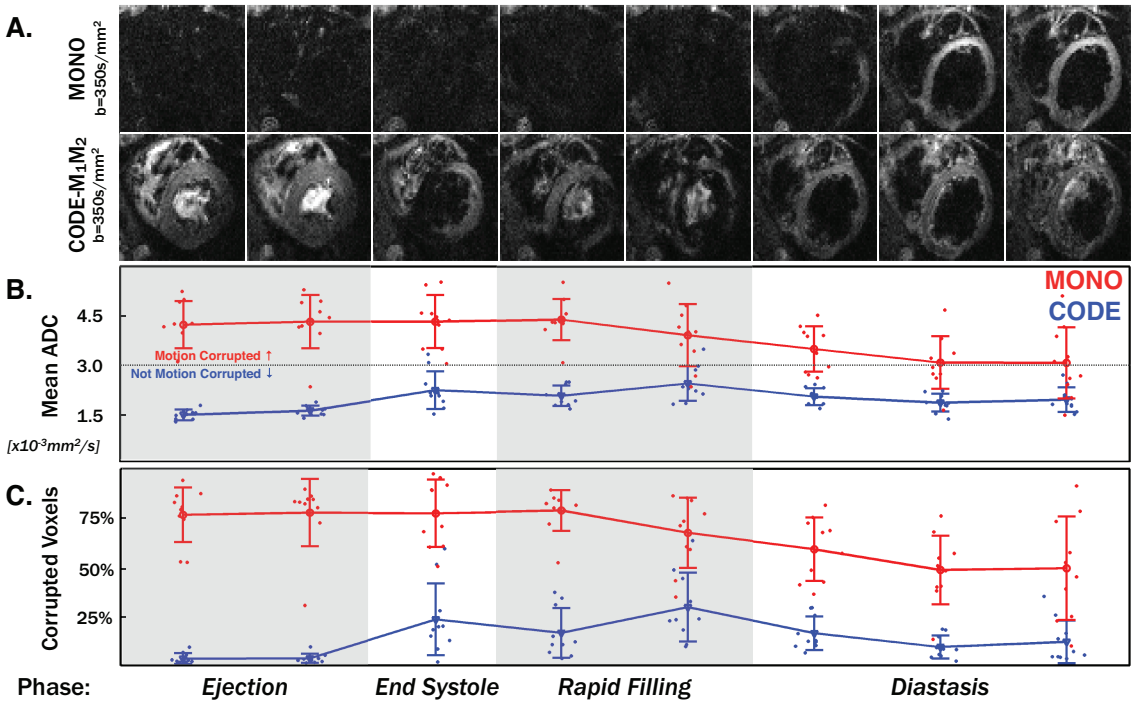

Figure 4.7: (A) Diffusion weighted images are shown from a typical healthy volunteer acquired at eight different cardiac phases with MONO and CODE-M_1M_2. Motion corruption in MONO is highly subject dependent and varies greatly with cardiac phase.(B) Mean±SD LV ADC values and (C) percentage±SD of motion corrupted (ADC>3.0x$10^{-3}$$mm^2$/s) LV voxels for MONO and CODE-M_1M_2 across the ten volunteers. CODE-M_1M_2 is much less sensitive to bulk motion and is not as dependent on precise sequence timing as shown by both (B) the lower ADC measurements and (C) lower percentage of motion corrupted voxels for all cardiac phases.

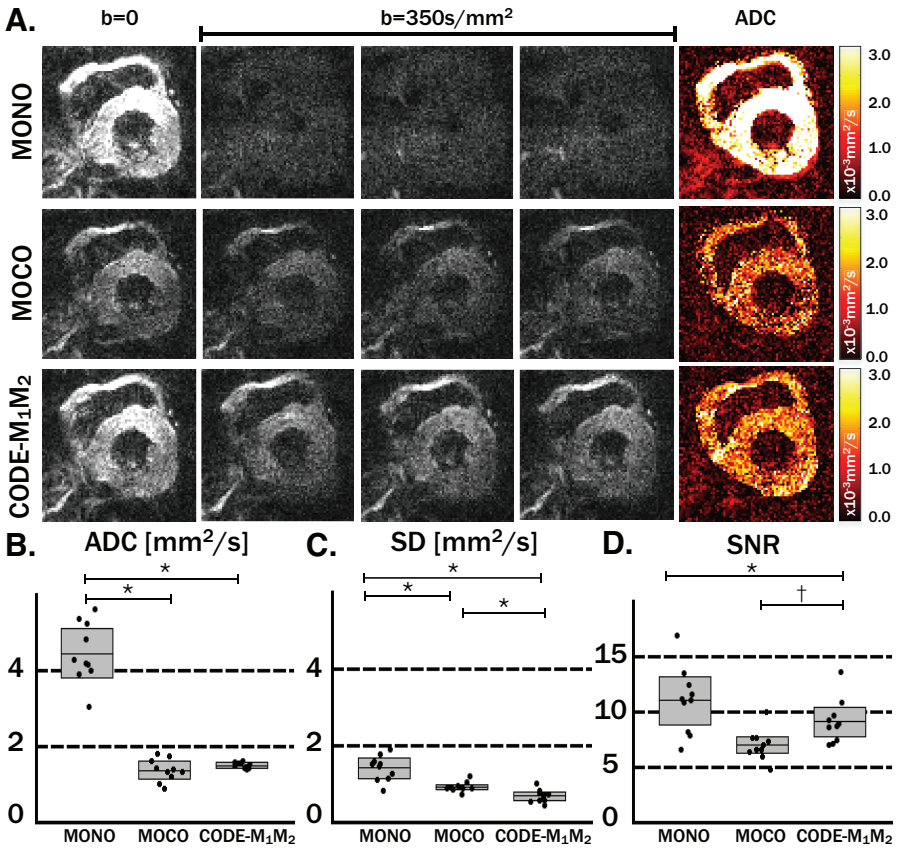

Figure 4.8: (A) Diffusion weighted images and ADC maps are shown from a typical healthy volunteer acquired at a single systolic cardiac phase with MONO, MOCO, and CODE-M_1M_2. MONO led to bulk motion corrupted DWI and subsequently elevated ADC maps while MOCO and CODE-M_1M_2 led to uncorrupted DWI and physiologically meaningful ADC values. (B) Mean septal ADC values were consistent between MOCO and CODE-M_1M_2, but much higher with MONO. CODE-M_1M_2 had less variability in mean ADC. (C) Standard deviations (SD) of the ADC within the septum were lower with CODE-M_1M_2 than MONO or MOCO. (D) SNR of the b=0 images was highest with MONO, but DWI were heavily corrupted. CODE-M_1M_2 had higher SNR than MOCO while maintaining bulk motion robustness.

4.6 Discussion

In this study, time-optimal, bulk motion compensated DWI with CODE gradient waveforms was described, implemented, and evaluated *in vivo* on a clinical scanner. CODE reduced the TE for all combinations of b-value and T_ε (Figure 4.3) and the largest reductions were seen for combinations of longer T_ε (higher spatial resolution) and larger b-values. The benefit of CODE is greatest for high resolution imaging (long T_ε) and is likely to be minimal in applications requiring coarse spatial resolution. Similarly, applications using low b-values may not benefit as much as applications that require large b-values, such as q-space[45] or diffusion spectrum[43] imaging.

TEs can also be reduced using partial Fourier acquisitions that asymmetrically sample k-space and shorten T_ε. Reducing T_ε decreases the TE reduction benefit from CODE (Figure 4.3). However, partial Fourier can lead to signal dropouts due to bulk vibrations or rotations[100, 101]. CODE can achieve TE reductions similar to partial Fourier methods without these adverse effects and while acquiring more k-space lines for improved SNR. For example, neuro CODE permitted full-Fourier with a negligible TE increase compared to MONO with 7/8 PF (67ms vs. 63ms), liver CODE-M_1 with full-Fourier had a shorter TE than BIPOLAR with 7/8 PF (72ms vs. 84ms) and cardiac CODE-M_1M_2 with full-Fourier had a shorter TE than MOCO with 7/8 PF (76ms vs. 81ms). Note that all comparisons assumed two-fold parallel imaging acceleration, which already roughly halves T_{EPI} and T_ε.

CODE gradient waveforms were designed to be optimal along any gradient direction and can thus be applied to diffusion tensor imaging (DTI) or higher order q-space sampling. However, because the diffusion encoding direction affects the available gradient amplitude (G_{max} effectively increases when more gradient axes are active simultaneously), the directions to be sampled must be accounted for in the optimization.

While the prospective concomitant field correction significantly reduced image artifacts, some residual errors could still be seen along some diffusion encoding directions, as evidenced

by overestimates of diffusivity near the phantom edges (e.g x-z, y-z, x-y-z in Figure 4.4). These are likely caused by the linear field approximation made in the correction. However, because these errors varied spatially with different diffusion encoding directions, the final ADC maps had minimal errors throughout the FOV. Further investigation into more sophisticated corrections is warranted and may be necessary for use in DTI.

No apparent eddy current distortions were observed in any of the CODE DWI compared with the non-diffusion weighted images or with MONO, BIPOLAR or MOCO encoding. There were also no issues associated with gradient heating or system instability from any of the CODE sequences.

While the phantom experiments showed good agreement between CODE and MONO in all protocols, CODE-M_1M_2 showed a slight positive ADC bias and increased variability as compared with MONO. One possible explanation is the lower SNR of this particular protocol caused by its high spatial resolution (1.5mm in-plane) and relatively long TE (TE=75ms). Previous reports have shown through simulation that low SNR imaging can lead to overestimates of ADC [102].

All gradient optimizations were performed with the slew rate constrained to ≤50T/m/s, which is significantly less than the 200T/m/s capability of the gradient system. This is a conservative bound that is software-imposed on all diffusion encoding gradients to avoid peripheral nerve stimulation (PNS). TEs can be further reduced if this constraint is relaxed, which can likely be done safely. Recent work has shown that a more sophisticated PNS model based on nerve response functions can be applied to safely shorten gradient waveforms [103]. Future work will include applying a similar approach to the CODE framework.

The neuro scans showed that CODE can improve the SNR of ADC maps by reducing TE compared to monopolar encoding at the same b-value. Neuro DWI often uses high spatial resolutions and large b-values (2000s/mm^2 or higher) which limit SNR. This necessitates many signal averages and long scan times. The shortened TEs permitted by CODE can reduce the

number of averages needed for acceptable SNR. Note that while only single slice imaging was performed, CODE is fully compatible with 2D multi-slice imaging.

In vivo liver (Figure 4.6) and cardiac (Figure 4.7, Figure 4.8) scans in healthy volunteers demonstrated the value of bulk motion compensated CODE. The results of this study echo previous reports of M_1M_2 nulled DWI in the heart by Nguyen et al. [65], Welsh et al. [19] and Stoeck et al. [18] as well as M_1 nulled DWI in the liver by Ozaki et al. [87]. The CODE framework is specifically designed for SE-EPI DWI and needs further evaluation to identify any advantages for diffusion preparation based sequences. For example, 3D segmented bSSFP with diffusion preparation [65] has a potential image quality advantage over SE-EPI, but also has lower acquisition efficiency and a long diffusion preparation time.

In the liver, CODE-M_1 resulted in lower ADC values than MONO in all regions, even in ROIs distal from the heart and ostensibly free of bulk motion (though not significantly different in the most distal ROI). BIPOLAR reported lower ADC values in all four regions (with significant differences in two of the four). Note too that the CODE-M_1 and MONO ADC measurements were in agreement in the phantom. This discrepancy is likely due to the perfusion sensitivity in MONO acquisitions that is reduced with CODE-M_1 and BIPOLAR. The motion of perfusing blood within liver tissue contributes to the diffusion encoding signal decay with MONO, leading to overestimates of ADC. This effect is reduced in CODE-M_1 and BIPOLAR and is absent as long as blood velocities are constant during diffusion encoding. All ADC reconstructions assumed a single compartment diffusion model and thus could not distinguish this effect.

The present work leverages state-of-the-art gradient hardware that can achieve high gradient amplitudes (G_{max}=80mT/m) and significantly shorten diffusion encoding gradient waveforms. This reduces the TE and improves bulk motion robustness (reduces the diffusion encoding footprint) as compared to more commonly available systems (typically G_{max}=40mT/m) [104, 105]**.** The benefit of similar maximum gradient amplitude performance for cardiac DWI has been previously demonstrated at 1.5T [18, 106]. While CODE can be used with any gradient

hardware and will always reduce TEs compared to symmetric encoding, all TEs will be lengthened significantly when using lower gradient amplitudes and/or lower slew rates. In these cases, moment-nulled diffusion encoding may limit SNR or extend the diffusion encoding intervals beyond a point that is practical for clinical use. In fact, acceptable image quality with M_1M_2 nulled SE-EPI DWI in the heart has not been demonstrated with G_{max}=40mT/m. Non-motion compensated CODE (only M_0 nulled) can still be used in this case to minimize the temporal footprint of diffusion encoding. In fact, in some conditions (e.g long T_ε), CODE converges to the single-sided bipolar waveform (Figure 4.1B) which is designed to be a bulk motion management technique [106].

All CODE gradient waveform design was performed using MATLAB (2013A, The Mathworks, Nattick, MA) running on a MacBook Pro (2.3 Ghz Core i7 with 16 GB RAM) and took between 2 and 5 minutes. This can likely be shortened by converting the optimization software to a faster language and by using a faster computer. However, it remains to be shown that the optimization can be fast enough to be performed during routine clinical exams. In this case, a database of waveforms previously optimized to a wide range of b-values and imaging constraints can be generated and readily accessed on the scanner.

4.7 Conclusion

CODE DWI reduced TEs for DWI with and without motion compensation compared to conventional encoding waveforms. Implementation on a clinical scanner in healthy volunteers demonstrated that CODE improved the SNR of ADC maps in DWI of the brain while CODE-M_1 and CODE-M_1M_2 improved the bulk motion robustness of DWI and ADC maps in the liver and heart with shorter TEs and consequently higher SNR than existing methods.

4.8 Acknowledgements

This work was supported, in part, by the Graduate Program in Bioscience at UCLA and the Department of Radiological Sciences at UCLA. The authors also benefitted from discussions with Stan Rapacchi, Subashini Srinivasan, Grace Kim, and Patrick Magrath.

5 SIMULTANEOUS T_2 AND ADC MEASUREMENT IN THE HEART

In this chapter, we modify the cardiac CODE-M_1M_2 approach developed in Chapter 5 to facilitate the simultaneous generation of quantitative myocardial T_2 and ADC maps. T_2 and ADC mapping both have potential value in the contrast free evaluation of MI but typically require separate acquisitions, which can be mismatched due to subject motion or subtle differences in image distortion. Our technique (T_2+ADC) generates perfectly co-registered maps with free breathing scans that do not increase scan time compared with ADC mapping alone. We demonstrate the T_2+ADC technique in simulations, phantom imaging, healthy volunteer imaging and in one patient with an acute MI. This work has been accepted for publication in *Magnetic Resonance in Medicine* in 2017: *Aliotta E, Moulin K, Zhang Z, Ennis DB. Simultaneous Measurement of T_2 and Apparent Diffusion Coefficient (T_2+ADC) in the Heart with Motion Compensated Spin Echo Diffusion Weighted Imaging. Magnetic Resonance in Medicine. 2017*.

5.1 Abstract

Purpose: To evaluate a technique for simultaneous quantitative T_2 and apparent diffusion coefficient (ADC) mapping in the heart (T_2+ADC) using spin echo (SE) diffusion weighted imaging (DWI).

Methods: T_2 maps from T_2+ADC were compared with single-echo SE in phantoms and with T_2-prepared (T_2-prep) balanced steady state free precession (bSSFP) in healthy volunteers. ADC maps from T_2+ADC were compared with conventional DWI in phantoms and in vivo. T_2+ADC was also demonstrated in a patient with acute myocardial infarction.

Results: Phantom T_2 values from T_2+ADC were closer to a single-echo SE reference than T_2-prep bSSFP (-2.3±6.0% vs. 22.2±16.3%, p<0.01) and ADC values were in excellent agreement with DWI (0.28±0.4%). In volunteers, myocardial T_2 values from T_2+ADC were significantly shorter than T_2-prep bSSFP (35.8±3.1ms vs. 46.8±3.8ms, p<0.01); myocardial ADC was not significantly (N.S.) different between T_2+ADC and conventional motion compensated (MOCO) DWI (1.39±0.18 vs. 1.38±0.18mm^2/ms, P=N.S.). In the patient, T_2 and ADC were both significantly elevated in the infarct compared with remote myocardium (T_2: 40.4±7.6ms vs. T_2=56.8±22.0ms, P<0.01, ADC: 1.47±0.59mm^2/ms vs. 1.65±0.65mm^2/ms, P<0.01).

Conclusion: T_2+ADC generated co-registered, free-breathing T_2 and ADC maps in healthy volunteers and a patient with acute MI with no cost in accuracy, precision or scan time compared with DWI.

5.2 Introduction

Cardiac diffusion weighted imaging (DWI) has high potential diagnostic value for quantifying the extent and degree of diffuse and focal myocardial fibrosis [8, 107] without the need for a gadolinium-based contrast agent. cDWI measures the self-diffusion of water molecules in soft tissues and can detect fibrosis via increases in the apparent diffusion coefficient (ADC) that accord with the increase in extracellular volume (ECV). This can enable myocardial infarct (MI) evaluation for the ~40% of cardiovascular disease patients with impaired renal function in whom the use of gadolinium-based contrast agents is contraindicated [13, 56].

Conventional DWI approaches are extremely sensitive to bulk motion, but recent developments in gradient hardware and the emergence of bulk motion compensated (MOCO) diffusion encoding techniques have enabled robust DWI in the heart [18, 65]. In this study, we employ convex optimized diffusion encoding (CODE) [108] with first (M_1) and second (M_2) order motion compensation (CODE-M_1M_2). CODE-M_1M_2 simultaneously imparts insensitivity to bulk motion and improves pulse sequence acquisition efficiency, by minimizing the echo time (TE) for a given b-value. The CODE approach enables higher resolution or higher signal-to-noise (SNR) cardiac MOCO DWI with shorter TEs than other techniques.

Quantitative T_2 mapping is also a valuable tool for myocardial tissue characterization. For example, increases in T_2 can indicate the presence of myocardial edema [32, 109] and decreases in T_2 have been observed in iron overload [110], which can occur in thalassemia as well as in hemorrhagic MI [111]. The combination of quantitative T_2 maps for detecting edema or iron overload and DWI maps for identifying myocardial fibrosis can potentially be used to differentiate infracts and score the extent and degree of focal and diffuse fibrosis for a variety of pathologies.

Herein, we describe a free-breathing technique that jointly measures cardiac T_2 and ADC (T_2+ADC) thereby generating maps that are perfectly co-registered and acquired at the same cardiac phase. T_2+ADC requires only minor modification to the spin-echo DWI acquisition and does not increase scan time compared to conventional ADC mapping alone. In this study, T_2+ADC was evaluated through Bloch equation simulations, validated with quantitative phantom imaging, and demonstrated in healthy volunteers.

5.3 Theory

DWI acquisitions typically employ a spin-echo (SE) sequence with a single-shot echo planar imaging (EPI) readout wherein several images are acquired at a fixed TE with diffusion

weighting along multiple directions. The diffusion weighting is characterized by the pulse sequence b-value (*b*, s/mm^2) and the gradient direction ($\vec{G}$) along which it is applied. This produces a series of images with combined T_2 and diffusion weighting that can be defined by a mono-exponential signal dependence on b and the underlying tissue diffusivity (D, mm^2/ms). In a classical DWI experiment, diffusion weighted images are normalized by a non-diffusion weighted acquisition (i.e. b=0) in order to extract only the diffusivity from all other sources of contrast. However, considering the T_2 weighting of the spin echo pulse sequence, the overall signal behavior can be described by a bi-exponential:

$$S(b, TE, \vec{G}) = S_0 e^{-TE/T_2} e^{-bD_{\vec{G}}} \quad 5.1$$

Where S_0 is the non-diffusion and non-T_2 weighted signal intensity, which is predominantly proton density weighted given a sufficiently long repetition time, TR. $D_{\vec{G}}$ is the diffusivity along the diffusion encoding direction $\vec{G}$. The resulting estimate of diffusivity from all sampled directions is denoted the apparent diffusion coefficient (ADC). In the proposed T_2+ADC technique, DWI was acquired with multiple TEs and T_2 and ADC were jointly reconstructed using Equation 5.1.

Because the signal to noise ratio (SNR) of cardiac DWI images can be very low (<10), signal averaging is typically used to suppress noise [18, 64, 112]. However, the non-diffusion weighted reference images (b=0) have significantly higher SNR than those with higher b-values and thus do not require as much signal averaging. Furthermore, while conventional DWI uses the same TE for all images to avoid mixing of T_2 and diffusion weighting, a shorter TE is always possible for b=0 due to the absence of diffusion encoding gradients. T_2+ADC leverages the shorter minimum TE when b=0 to improve SNR and enable the estimation of joint T2+ADC maps. By varying the TE of the non-diffusion weighted images across the repetitions that are necessary to

improve SNR for b>0, T_2+ADC mapping can be acquired with no increase in scan time compared with an analogous ADC mapping acquisition with a single, fixed TE.

5.4 Methods

5.4.1 Bloch Simulations

Bloch equation simulations [113] were used to evaluate and optimize the T_2+ADC acquisition for measurement precision and accuracy. The simulations were designed to fulfill two principal objectives: 1) Determine the minimum TR necessary for T_2+ADC to be insensitive to T_1 (<1% T_2 bias) and thus to changes in heart rate; and 2) Determine the optimal distribution of signal averages for each of the TEs to optimize measurement accuracy under the constraint of fixed scan time.

Simulation Parameters – T_2+ADC acquisitions were simulated using a system of 500 independent spins. The signal amplitude during a spin echo sequence was simulated for two TEs (TE_1=25ms, TE_2=65ms) and two b-values (b=0 and 350s/mm^2). TE_1 and TE_2 were the minimum TEs for the desired 2.0x2.0x5.0mm spatial resolution with b=0 and 350s/mm^2, respectively. These specific TEs accorded well with published sampling guidelines for T_2 mapping of the range of expected myocardial T_2 values [114, 115]. The b-value was chosen to balance SNR, motion insensitivity, and diffusion weighting and was similar to previous cardiac DWI studies [80, 116]. To incorporate T_2* effects, the spin system contained a range of off resonance frequencies ±50Hz (uniformly distributed, corresponding to T_2*~20ms). Repeated simulations were performed over a range of T_1 (T_1=500, 1000, 1500ms) and T_2 values (T_2=30, 40, 50, 60ms). The spin ensemble's signal amplitude was measured over a duration surrounding TE corresponding to the duration of the EPI readout (T_{EPI}=30ms). These signal amplitudes were used to modulate the k-space of a simulated left ventricle (LV) as shown in

Figure Figure 5.1. Diffusion encoding (D=1.4mm^2/ms, isotropic) was applied to the simulated signals directly using Equation **5**.**1** along three directions (x, y and z). Simulated T_2 and ADC maps were then generated from the resultant signals using Equation **5**.**1**.

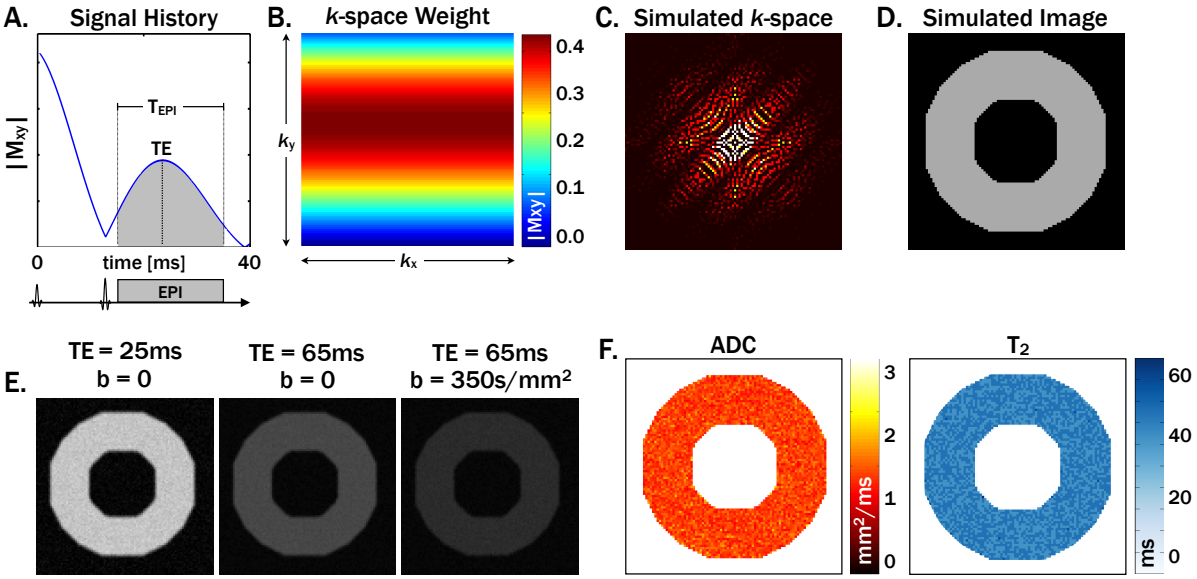

Figure 5.1: T_2+ADC Bloch equation simulation framework. (A) T_2 weighting was generated using Bloch equation simulations of the signal during the spin echo acquisition, which generated (B) the k-space weighting that modulated line-by-line the k-space corresponding to a simulated LV for two TEs (25ms and 65ms) and two b-values (b=0 and 350s/mm2). (D) Complex Gaussian noise was added to the resultant k-space signals to generate noisy images (E) that were then used to estimate T_2 and ADC (F) according to Equation **5**.**1**.*

Impact of T_1 on T2+ADC – To evaluate the impact of T_1 on T_2 and ADC accuracy, the simulation was performed over a range of 10 TRs from 500ms to 5000ms for every combination of T_1 and T_2 evaluated. Mean T_2 and ADC values were then calculated for each TR within the simulated LV. T_2 and ADC accuracy were evaluated by the percent difference between the mean T_2 and ADC and the pre-defined input values.

Evaluating Signal Average Distribution – To define the distribution of signal averages for subsequent *in vivo* acquisitions, complex Gaussian noise was added to the simulated images

such that SNR=50 for b=0 and TE=25ms. Scan time was held constant by maintaining the total number of acquired images (10 signal averages per direction for b=350s/mm^2 and 10 total averages for b=0 and both TE_1 and TE_2). The ratio of averages between TE_1 and TE_2 was, however, varied (i.e. $N_{avg,TE1}$:$N_{avg,TE2}$ = 9:1, 8:2, 7:3, etc.). Measurement precision was quantified for each acquisition by the standard deviation (SD) of T_2 and ADC values within the simulated LV.

5.4.2 Phantom Experiments

T_2+ADC was acquired in a phantom containing vials of water with varying concentrations of agar and $CuSO_4$ which produced a range T_1 and T_2 values (T_1=400-2000ms, T_2=30-150ms) on a 3T MRI scanner (Prisma, Siemens, Erlangen, Germany). The T_2+ADC protocol used TE_1=25ms and TE_2=65ms; TR=4000ms; b=0 and b=350s/mm^2 with CODE-M_1M_2 diffusion encoding along three directions (x, y, z). Three "dummy" cycles (i.e. repetitions of the b=0 sequence without readout) were played to ensure the signal reached a steady state prior to acquiring the first b=0 image. Additional T_2 maps were generated for comparison using: 1) Spin echo imaging with five TEs (TE=12, 25, 55, 85, 100ms, TR=12s); and 2) T_2-prepared (T_2-prep) balanced Steady State Free Precession (bSSFP) with three T_2-prep durations (t_{prep}=0, 25, 55ms, TR=3s), an established technique for myocardial T_2 mapping [117]. For comparison, a conventional ADC map was generated using a DWI protocol matched to the T_2+ADC protocol, but with a single TE (TE=65ms). Additional protocol details are shown in Table 5.1.

$T_{2,T2+ADC}$ and $T_{2,bSSFP}$ were compared to the reference $T_{2,SE}$ using regression analysis on mean T_2 values within each of the 10 phantom regions. ADC_{T2+ADC} was similarly compared with the conventional ADC_{DWI}.

5.4.3 Volunteer Experiments

Healthy volunteers (N=8) were then imaged in an IRB approved study after obtaining written statements of informed consent. Localizers were first acquired to obtain a mid-ventricular short-axis slice that was used for all subsequent imaging. Cine bSSFP images were acquired and visually inspected to determine the timing of the diastolic quiescent period during which bulk cardiac motion was minimized. This subject-specific trigger delay (TD_{DIA}) was used for all subsequent diastolic imaging.

	Resolution (mm)	FOV (mm)	TE (ms)	t_{prep} (ms)	TR (ms)	b (s/mm^2)	Undersampling
T_2+ADC	2.0x2.0x5.0	260x130	25, 65	N/A	4000	0, 350	6/8 PF, iPAT x2
DWI	2.0x2.0x5.0	260x130	65	N/A	4000	0, 350	6/8 PF, iPAT x2
bSSFP	1.5x1.5x5.0	312x312	1.17	0, 25, 55	3000	N/A	6/8 PF
SE	1.0x1.0x5.0	200x200	12,25,55,85,100	N/A	10000	N/A	N/A

Table 5.1: Protocol details for each of the T_2 and ADC mapping sequences.

T_2+ADC – Free breathing T_2+ADC images were acquired with respiratory triggering to end-expiration using a liver-dome navigator. Protocol details were: 2.0x2.0x5.0mm resolution, FOV=260x200mm, 6/8 Partial Fourier (PF), and 2x parallel imaging acceleration using Generalized Autocalibrating Partially Parallel Acquisitions (GRAPPA)[35]. Based on simulation results, the non-diffusion weighted images were acquired with three averages for TE_1 and seven averages for TE_2; b=350s/mm^2 images were acquired at TE=65ms with 10 averages using CODE-M_1M_2. Imaging was triggered to at least every fourth heartbeat such that TR≥4000ms and three "dummy" cycles were played prior to acquiring the first b=0 image. Inner volume excitation was used to reduce the field of view in the phase encode direction, thereby shortening the readout duration and reducing image distortions [73]. TE_2 (b=0 and 350s/mm^2) was acquired at mid-systole using TD_{SYS}=100ms and at late diastole using TD_{DIA} whereas TE_1 was shifted

(TD_{SYS}+40ms and TD_{DIA}+40ms) such that imaging occurred at the same cardiac phase (Figure Figure 5.2). Acquiring 40 images per phase required a total scan time of ~10 minutes.

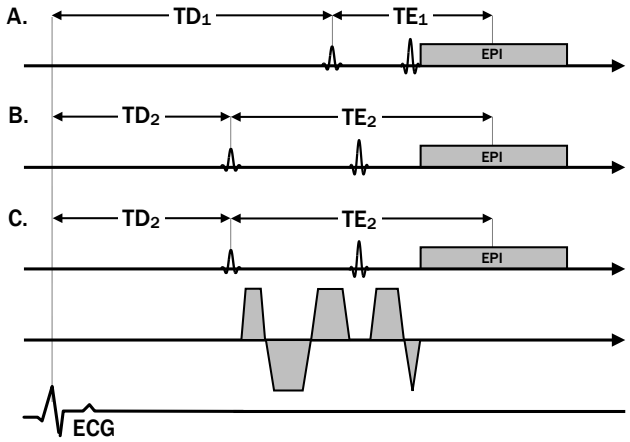

Figure 5.2: T_2+ADC pulse sequence diagram. T_2+ADC consists of SE EPI DWI with b=0 reference images at TE=25ms (A) and TE=65ms (B) to enable T2 mapping. (C) Bulk motion robust CODE-M1M2 gradients were used (b=350s/mm2, TE=65ms) to obtain cardiac DWI within a reasonable TE. ECG trigger delays were defined for each acquisitions such that imaging always occurred at the same cardiac phase.

Image reconstruction was then performed using custom MATLAB code (The Mathworks, Nattick, MA). Prior to averaging, all images were co-registered using a rigid transformation to correct for respiratory motion and motion corrupted voxels were removed using a constrained reconstruction algorithm [104] to correct for artifactual bulk motion signal drop out in the DWI. In this algorithm, a single gradient direction ADC projection, ADC_0, was calculated for each image and any voxels in which ADC_0 exceeded 3.0mm^2/ms (the free diffusivity of water at 37°C, a fundamental limit for diffusion in soft tissue) were discarded.

The T_2+ADC reconstruction was then performed using two methods: 1) a non-linear fit (NLF) to Equation **5**.**1**; and 2) a linear fit (LF) to the natural log of Equation **5**.**1**. For each fitting method, mean T_2 (μ_{T2}), T_2 standard deviation (σ_{T2}), mean ADC (μ_{ADC}), and ADC standard deviation (σ_{ADC}) were calculated within the LV.

Independent T_2 Mapping – For comparison to T_2+ADC, breath-held T_2-prep bSSFP maps were acquired at the same slice location at mid-systole and diastole in separate breath holds with 1.5x1.5x5.0mm resolution, TE=1.17, TR=3 heartbeats, linear k-space encoding and three T_2-prep durations (t_{prep}=0, 25, 55ms). T_2 maps were reconstructed using a least squares linear fit.

Conventional ADC Mapping – ADC maps were also generated from the CODE-M_1M_2 DWI acquired for T_2+ADC, but using only TE=65ms at both systole and diastole. ADC values were reconstructed using a least squares linear fit.

T_2 and ADC Map Comparisons – LV masks were manually defined and were used to determine $\mu_{T2,T2+ADC}$, $\sigma_{T2,T2+ADC}$, $\mu_{T2,bSSFP}$ and $\sigma_{T2,bSSFP}$ for each subject at both systole and diastole. μ_{T2} and σ_{T2} reported by each technique were compared using a paired t-test across the eight subjects.

The same analysis was performed on the ADC maps to measure $\mu_{ADC,T2+ADC}$, $\mu_{ADC,DWI}$, $\sigma_{ADC,T2+ADC}$ and $\sigma_{ADC,DWI}$ for each subject at both cardiac phases.

5.4.4 Patient Imaging

T_2+ADC were acquired on a patient undergoing a clinically indicated cardiac MRI examination at 3.0T (Siemens Prisma) with a non-reperfused acute MI in the infero-lateral wall, impaired LV ejection fraction (22%) and a pericardial effusion after a failed rescue percutaneous coronary intervention. Imaging parameters were identical to the volunteer experiments, but the acquisition was limited to a single mid-ventricular slice at mid-systole (TD=100ms) and the number of averages was reduced to shorten scan time ($N_{avg,TE1}$=2, $N_{avg,TE2}$=3, scan time ~5min. Post-contrast late gadolinium enhanced (LGE) and cine (bSSFP) images were also acquired for reference. Median T_2 and ADC values were measured in manually defined regions of remote and infarcted myocardium as defined on LGE.

5.5 Results

5.5.1 Simulations

T_2+ADC Accuracy – T_2+ADC Bloch simulation results are shown in Figure 5.3. T_2 errors were observed in measurements made with short TRs, but these became negligible (<1%) for all simulated T_1 and T_2 values when TR≥4000ms (Figure 5.3A). For TR=1000ms (approximately one heart beat), T_2 error was as high as 4.6% (for T_1=2000ms, T_2=30ms). TR had no impact on ADC accuracy (ADC accuracy <0.1% for all simulated T_1 and T_2 values) (Figure 5.3B).

T_2+ADC Precision – Both T_2 and ADC precision were dependent on the ratio of $N_{avg,TE1}$:$N_{avg,TE2}$ (Figure 5.3C and D). The precision of both the T_2 and ADC maps was greatest when $N_{avg,TE1}$:$N_{avg,TE2}$=9:1. σ_{ADC} decreased monotonically as $N_{avg,TE1}$:$N_{avg,TE2}$ decreased, but with minimal change when $N_{avg,TE1}$:$N_{avg,TE2}$≤4:6. σ_{T2} was a concave function of $N_{avg,TE1}$ and reached a minimum at $N_{avg,TE1}$:$N_{avg,TE2}$=3:7 for all T_1 values .

5.5.2 Phantom Experiments

Compared with the reference $T_{2,SE}$ maps, T_2+ADC underestimated T_2 ($T_{2,T2+ADC}$ = 1.01*$T_{2,SE}$ – 1.9ms, R^2=0.99) while bSSFP overestimated T_2 ($T_{2,bSSFP}$ = 1.02*$T_{2,SE}$ + 8.8ms, R^2=0.97) for T_2 values between 30ms and 150ms (Figure 5.4A). Across all T_2 reference values, $T_{2,T2+ADC}$ was closer to $T_{2,SE}$ and had a lower variance than $T_{2,bSSFP}$ (-2.3±6.0% vs. 22.2±16.3%, p=2x10^{-7}). Very high agreement was observed in the diffusion phantom between ADC_{T2+ADC} and conventional ADC_{DWI} (ADC_{T2+ADC} = 1.01*ADC_{DWI} - 0.02 mm^2/ms, R^2=0.99, mean ADC difference: 0.14±0.39%) (Figure 5.4B).

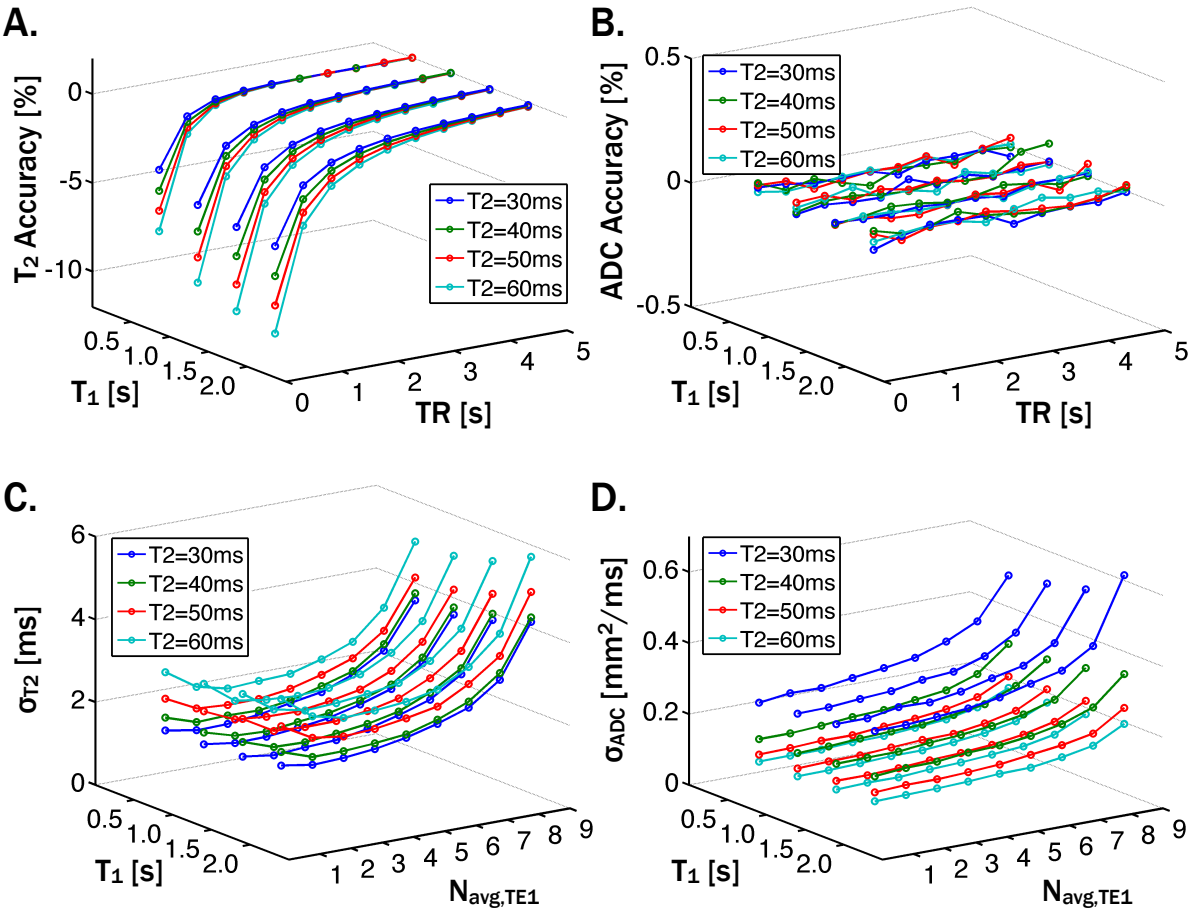

Figure 5.3: Bloch simulation results for joint T_2+ADC mapping. T_2 accuracy (A) was <1% when TR≥4000ms whereas ADC accuracy (B) was <1% for all TRs. T_2 precision (C) was minimized when $N_{avg,TE1}$=3 (TE_1=25ms) and $N_{avg,TE2}$=7 (TE_2=65ms) for all T_1 ($N_{avg,TE1}$+$N_{avg,TE2}$=10). ADC precision (D) decreased with decreasing $N_{avg,TE1}$, but the change was negligible with $N_{avg,TE1}$≤4.

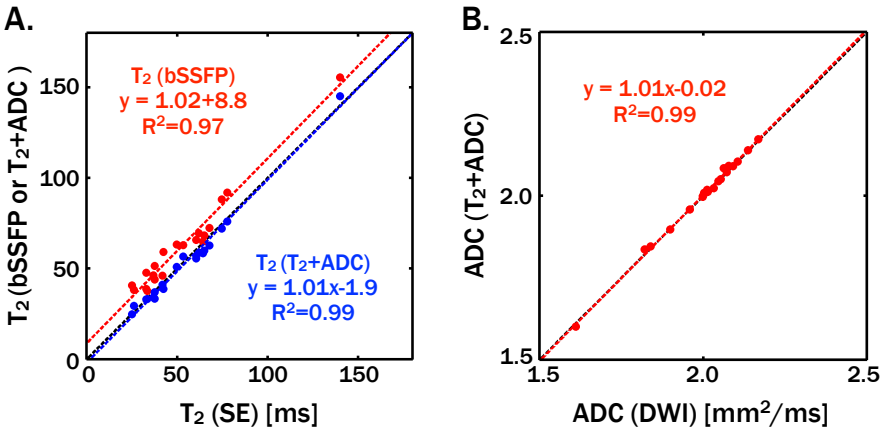

Figure 5.4: (A) T_2 phantom validation results comparing T_2+ADC (blue) and T_2-prepared bSFFP (red) to conventional SE T_2-mapping. (B) compares ADC from T_2+ADC to conventional DWI. Good agreement was observed between T_2 techniques, but bSSFP overestimated T_2 while T_2+ADC slightly underestimated T_2 compared with conventional SE. Very high agreement was observed between ADC maps. The dashed black line is the line of unity.

5.5.3 Volunteer Experiments

Impact of Fitting Algorithm – T_2 and ADC maps were successfully acquired in all eight volunteers during both systole and diastole using T_2+ADC. The choice of fitting algorithm had no significant impact on the population mean or variance of the T_2 maps (LF-μ_{T2}=37.7±3.8ms vs. NLF-μ_{T2}=37.7±3.8ms, p=1.00; LF-σ_{T2}=7.4±1.2ms vs. NLF-σ_{T2}=7.4±1.2ms, p=0.99). NLF and LF mean ADC values were not significantly different (LF-μ_{ADC}=1.58±0.28mm^2/ms vs. NLF-μ_{ADC}=1.53±0.25mm^2/ms, p=0.56), but the NLF ADC variance was significantly lower than LF (LF-σ_{ADC}=0.63±0.21mm^2/ms vs. NLF-σ_{ADC}=0.46±0.15mm^2/ms, p=0.01). With conventional DWI, mean ADC from T_2+ADC mapping was not significantly different from NLF or LF ($\mu_{ADC,DWI}$=1.51±0.26mm^2/ms, $\mu_{ADC,NLF}$=1.53±0.25mm^2/ms, p=0.48, $\mu_{ADC,LF}$=1.58±0.28mm^2/ms, p=0.28). ADC variance from T_2+ADC mapping was significantly lower than LF ($\sigma_{ADC,DWI}$=0.47±0.15mm^2/ms vs. $\sigma_{ADC,LF}$=0.63±0.21mm^2/ms, p=0.02), but not different from NLF ($\sigma_{ADC,DWI}$=0.47±0.15mm^2/ms vs. $\sigma_{ADC,NLF}$=0.46±0.15mm^2/ms, p=0.80). T_2 and ADC maps generated using both NLF and LF fitting algorithms are shown in Figure 5.5. All subsequent analysis of T_2+ADC was performed using NLF because of the lower NLF ADC variance.

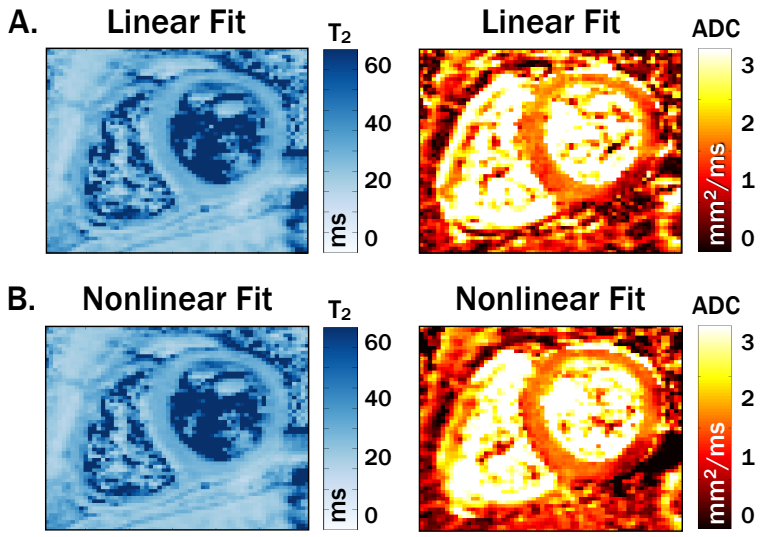

Figure 5.5: Example T2 and ADC maps from T2+ADC generated using linear fitting (A) and nonlinear fitting (B). The choice of fitting algorithm had no significant impact on the mean or variance of the T2 maps. Nonlinear fitting had no significant impact on mean ADC, but led to ADC maps with significantly lower variance (p=0.01).

In Vivo T_2 and ADC Mapping – Representative T_2 maps from T_2+ADC and T_2-prep bSSFP at both mid-systole and diastole are shown in Figure 5.6. ADC maps from T_2+ADC and DWI in the same subject are shown in Figure 7. Mean myocardial T_2 and ADC values (μ_{T2} and μ_{ADC}) as well as myocardial T_2 and ADC variances (σ_{T2} and σ_{ADC}) from each technique are shown in Figure 5.6 and Figure 5.7 as well as in Table 5.2.

Mean myocardial T_2 values from T_2+ADC were significantly lower than bSSFP at both systole and diastole. There were no significant differences in T_2 between systole and diastole within either technique. T_2 variance was significantly lower with T_2+ADC than with T_2-prep bSSFP at both systole and diastole.

There were no significant differences in mean myocardial ADC between T_2+ADC and conventional DWI at either systole or diastole. However, ADC was significantly lower during systole than diastole within both T_2+ADC ($p=0.02$) and DWI ($p=0.03$). No significant differences were observed in ADC variance between T_2+ADC and DWI at systole or diastole.

	Mid-Systole				Diastole			
	μ_{T2} (ms)	σ_{T2} (ms)	μ_{ADC} (mm^2/ms)	σ_{ADC} (mm^2/ms)	μ_{T2} (ms)	σ_{T2} (ms)	μ_{ADC} (mm^2/ms)	σ_{ADC} (mm^2/ms)
T_2+ADC	35.8±3.1	6.9±1.1	1.39±0.18	0.41±0.09	39.2±5.4	8.0±1.0	1.64±0.31	0.51±0.18
DWI	N/A		1.38±0.18	0.41±0.08	N/A		1.65±0.32	0.52±0.19
bSSFP	46.8±3.8*	12.2±3.2*	N/A		46.8±3.4*	14.0±4.1*	N/A	

Table 5.2: Quantitative in vivo results.

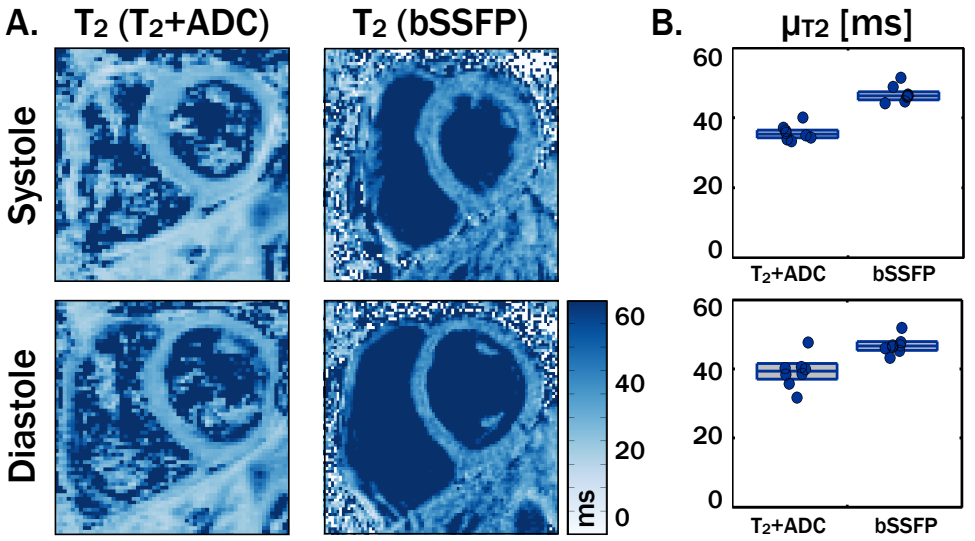

Figure 5.6: Representative T2 maps measured in a healthy volunteer using T2+ADC and T2-prepared bSSFP (A) at a mid-systolic (top row) and diastolic (bottom row) cardiac phase. The mean myocardial T2 values (μT2) measured by each technique for eight (N=8) subjects are also shown in (B). The box edges represent the population mean ± 1SD and individual points represent the mean intra-subject value. Consistent with phantom results, T2+ADC reported significantly lower T2 values than T2-prep bSSFP at both systole (p=6x10-4) and diastole (p=1x10-3).

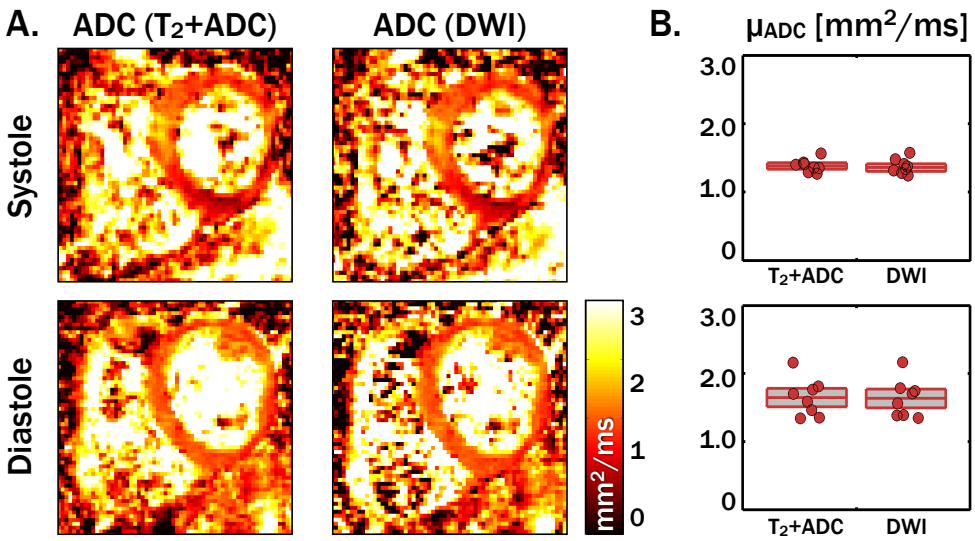

Figure 5.7: ADC maps (A) from the healthy volunteer shown in Figure 5.6 using T2+ADC and DWI at a systolic (top row) and diastolic (bottom row) cardiac phase. The mean myocardial ADC values (μADC) measured by each technique for eight (N=8) subjects are also shown in (B). The box edges represent the population mean ± 1SD and individual points represent the mean intra-subject value. No significant differences were observed in the ADC values reported by T2+ADC and DWI at either phase.

5.5.4 Patient Imaging

T_2 and ADC maps and histograms from T_2+ADC are shown in Figure 5.8 along with companion bSSFP and LGE. LGE revealed a large region of enhancement in infero-lateral LV free wall. T_2+ADC showed a significant increase in T_2 within the infarct compared with remote myocardium ($T_{2,Remote}$=40.4±7.6ms vs. $T_{2,Infarct}$=56.8±22.0ms, P<0.01) as well as a significant increase in ADC (ADC_{Remote}=1.47±0.59mm^2/ms vs. $ADC_{Infarct}$=1.65±0.65mm^2/ms, P<0.01).

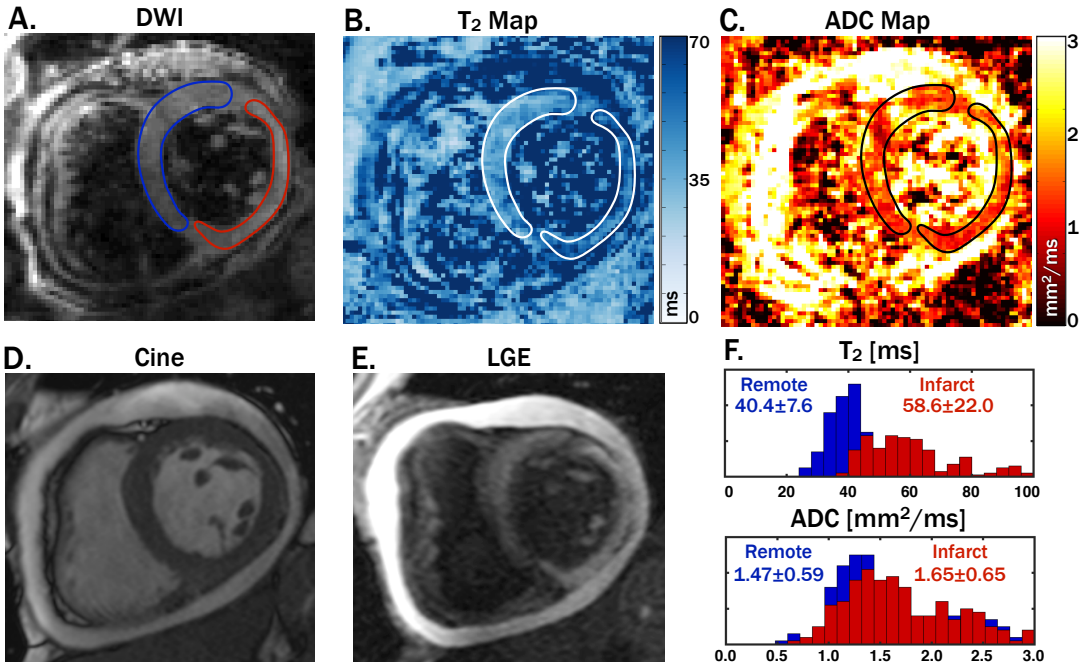

Figure 5.8: A representative diffusion weighted image (A), T_2 map (B), ADC map (C), cine image (D), and LGE (E) from a patient with acute MI. T_2 and ADC were both elevated in the infarct region (lateral wall) compared to the remote myocardium (septal wall) ($T_{2,Infarct}$=56.8±22.0ms vs. $T_{2,Remote}$=40.4±7.6ms, P<0.01, $ADC_{Infarct}$=1.65±0.65mm^2/ms vs. ADC_{Remote}=1.47±0.59mm^2/ms, P<0.01).

5.6 Discussion

T_2+ADC permitted quantitative estimates of T_2 from cardiac DWI acquisitions with no significant impact on ADC measurement and no increase in scan time compared with conventional DWI. While the simulations indicated that a TR≥4s (i.e. approximately 4 heart beats) should be used to eliminate T_1 effects, this significantly limits acquisition efficiency. Although a single slice acquisition was used in this study, T_2+ADC is compatible with multi-slice imaging approaches (e.g. slice following [57]) which would substantially improve acquisition efficiency.

While the linear bi-exponential fit in T_2+ADC did increase ADC variance compared with conventional DWI, the loss in precision was mitigated by using a non-linear exponential fit (NLF) in place of the conventional log-linear fit. When using the NLF, there were no significant

differences in the mean or variance of myocardial ADC with T_2+ADC compared with DWI. This indicates that T_2+ADC can generate both maps with no cost in scan time compared with DWI and without affecting ADC measurement.

Myocardial T_2 values measured using T_2+ADC were significantly shorter than those reported by bSSFP in both the phantom and *in vivo* experiments. However, in the phantom, T_2+ADC was closer to the SE reference than bSSFP. This is consistent with reports of bSSFP overestimating T_2, which are likely due to T_1 signal weighting [118]. It is possible that T_2* decay during the single shot SE-EPI readout caused T_2+ADC to underestimate T_2. However, this effect did not bias T_2 measurements in simulations and did not lead to significant errors compared to SE measurements in the phantom study. We expect the SE sequence produces accurate T_2 measurements as it is free of any stimulated echo effects that are known to lead to errors in multi-echo spin echo T_2 mapping [119-122]

In our experience, the M_1+M_2 nulled diffusion encoding approach used in this work performs best during systolic imaging due to the consistent and coherent motion during that phase [18, 108]. Experience shows that diastolic motion tends to be less consistent and varies with changes in heart rate, which can lead to artificially high diastolic ADC values. This was reflected in the higher and more variable ADC values observed in diastole with both T_2+ADC and DWI despite the constrained image reconstruction algorithm that eliminates the most severe bulk motion artifacts.

Slightly shorter T_2 values were reported at mid-systole compared to diastole when measured with T_2+ADC, whereas no such decrease was observed in bSSFP. This difference could also be caused by bulk motion sensitivity in the SE-EPI pulse sequence. The second order moment of the crusher gradients surrounding the refocusing pulse used for the b=0 acquisitions depends on their timing within the pulse sequence [26]. Consequently, acquisitions with long TEs are more bulk motion sensitive than those with short TEs. This could lead to additional signal decay

for longer TEs, which would shorten the apparent T_2 from T_2+ADC, as observed in mid-systole compared with diastole. Furthermore, inconsistent motion during of diastole may have led to the increase in T_2 variability in diastole.

One drawback of T_2 mapping with T_2+ADC compared with T_2-prep bSSFP is the impact of single shot SE EPI on image quality, which has known issues with distortion and chemical shift in the heart [70]. The use of inner volume excitation combined with high performance imaging gradients significantly mitigates these issues by shortening the EPI readout, but further work is necessary to improve image quality. Furthermore, the minimum TE achievable in T_2+ADC is directly linked to the EPI readout duration, which in turn limits spatial resolution for a given TE. Parallel imaging and partial Fourier were used to shorten the EPI readout and thereby decrease the minimum achievable TE and mitigate EPI distortions. However, this impacts SNR, which necessitated signal averaging. In the present study, the minimum TE of 25ms appeared to be sufficiently short for healthy myocardial T_2 quantification, but this may present a problem with shortened T_2 values in conditions such as Thalassemia [123]. These drawbacks could potentially be avoided by adapting T_2+ADC to a diffusion prepared acquisition [65] at the cost of a significantly longer temporal footprint due to the duration of a single or multi-shot bSSSP readout compared with single shot EPI.

The preliminary T_2+ADC mapping results in acute MI indicate that this technique is applicable in severely ill patients and can detect the presence of fibrosis and edema. Notably, there was good agreement between ADC values in remote myocardium for this patient and those measured in volunteers. Remote T_2 values were slightly longer than what was seen in volunteers at mid-systole which indicates the presence of global inflammation which is expected after acute MI [124]. Infarct T_2 values were consistent with those reported by Giri et al. [32] but infarct ADC values were lower than values observed by Nguyen et al. [116].

5.7 Conclusion

T_2+ADC is a novel technique for simultaneously estimating T_2 and ADC in the heart during a free-breathing acquisition. T_2+ADC generated perfectly co-registered maps and had no impact on ADC accuracy, ADC precision or scan time compared with conventional DWI while making precise measurements of myocardial T_2.

5.8 Acknowledgements

This work was supported, in part, by the Graduate Program in Bioscience at UCLA, the Department of Radiological Sciences at UCLA, the National Institutes of Health (NIH R01HL131975), and the American Heart Association (AHA 16PRE27380023). The authors would like to thank Drs. Pierre Croisille and Magalie Viallon for the clinical dataset presented in this work.

6 QUANTIFYING PRECISION IN CARDIAC DIFFUSION TENSOR IMAGING

In this chapter, we leverage the Convex Optimized Diffusion Encoding (CODE) framework to acquire and evaluate *in vivo* cardiac diffusion tensor imaging (cDTI) using first and second order motion compensated diffusion encoding (CODE-M_1M_2) in healthy volunteers. To assess the precision of this technique, we employ a previously described bootstrapped resampling approach to measure the 95% confidence intervals for measured diffusion tensor orientation (i.e. eigenvectors) and shape (i.e. eigenvalue-based invariants) in clinically viable free-breathing scans with durations between one and five minutes per slice. We also compare the precisions of cDTI acquired in mid-systolic and diastolic cardiac phases to assess the impact of bulk cardiac motion on measurement precision of CODE-M_1M_2 in healthy volunteers.

6.1 Introduction

Cardiac diffusion tensor imaging (cDTI) is an emerging contrast-free technique for quantifying microstructure in healthy [125, 126] and diseased myocardium [14-16]. cDTI provides quantitative maps of local cardiomyocyte orientation, the organization of myolaminar sheetlets, and microstructural anisotropy by probing the diffusion of water molecules contained in

myocardial tissue. Increases in the mean diffusivity (MD) have been linked to the presence of fibrosis in myocardial infarction as well as changes in extracellular volume in hypertrophic cardiomyopathy [8, 116]. Changes in myocardial sheetlet dynamics have also been demonstrated in hypertrophic and dilated cardiomyopathies using cDTI [14-16].

As with any quantitative measure, several sources of error lead to uncertainty for *in vivo* cDTI measurements. These include noise, image distortions, and physiological variability. Noise can have a large impact on cDTI derived parameters due to the low signal to noise ratios (SNR) of the acquired diffusion weighted images that stem from the diffusion induced signal decay and the reliance on single shot echo planar imaging (SS-EPI) readouts. Image distortions can also be substantial in cDTI due to sharp magnetic susceptibility gradients at the heart-lung interface that are exacerbated by the SS-EPI readout [127]. Physiological variability is also significant in cDTI due to the presence of bulk cardiac and respiratory motion as well as pulsatile blood flow. This variability can lead to both corrupted individual measurements (i.e. intra-shot motion effects) and mismatches between subsequent measurements (i.e. inter-shot variability between encoding directions or repetitions).

The propagation of these errors from the acquired image data through diffusion tensor reconstruction and on to derived tensor quantities is a complex problem that is not easily modeled. As a result, a non-parametric bootstrapped approach has been proposed for quantifying uncertainty in diffusion tensor orientation [128] and shape [129, 130] in neurological DTI. This approach provides insight into the uncertainty underlying neurological DTI experiments [131, 132], but these results do not directly apply to *in vivo* cDTI for several reasons. Namely, cardiomyocytes are approximately ten times thicker in diameter than neuronal fibers [133, 134] which leads to diffusion tensors with substantially lower fractional anisotropy (FA) and consequently larger uncertainties in measures of fiber orientation [128]. Cardiac motion also necessitates the use of highly specialized pulse sequences which employ either

motion compensated diffusion encoding gradients [18, 19, 65, 135] or a stimulated echo acquisition mode (STEAM) with diffusion encoding spread across multiple heart beats [64, 136]. Furthermore, even when using motion compensated diffusion encoding schemes, slight variations in heart rate and breathing patterns throughout an acquisition contribute a degree of uncertainty to the measured signal. The impact of bulk physiological motion also depends on the pulse sequence timing within the cardiac cycle [135] and thus uncertainty is expected to depend on the cardiac phase selected for triggering, but this has not yet been characterized.

In light of the many sources of variability present in cDTI, standard practice is to acquire multiple repetitions of the protocol and average the repeated data to increase SNR and thus improve measurement precision. This, of course, increases scan times that are already long in cDTI due to the need for multiple diffusion encoding directions and both cardiac and respiratory triggering (or multiple repeated breath holds). Therefore, it is useful to quantify the precision of cDTI measurements made within clinically viable scan durations.

In this study, we employ bootstrapped uncertainty measurements to characterize the precision of *in vivo* spin echo EPI cDTI measurements made using first and second order motion compensated convex optimized diffusion encoding (CODE) [108] at two points in the cardiac cycle (mid-systole and diastole). Herein, we quantify the precision of diffusion tensor orientation (i.e. tensor eigenvectors) and shape (i.e. tensor invariants) for cDTI acquisitions with scan times between one and five minutes per slice to identify practical guidelines for efficiently measuring high quality microstructural information.

6.2 Theory

Diffusion tensor uncertainty can be measured for a cDTI acquisition using bootstrapped resampling to generate a distribution of tensors that reflects the uncertainty inherent in the measurement. This was previously described for calculating uncertainty in the tensor primary

eigenvector, which was referred to as the “cone of uncertainty” [128]. This technique is briefly described herein and extended to quantify other aspects of diffusion tensor uncertainty including the secondary and tertiary eigenvectors as well as several tensor invariants.

This bootstrapping technique requires the cDTI acquisition to be repeated twice to generate two independent, but matched datasets. From these, a composite dataset can be generated by randomly sampling images for each diffusion encoding direction between the two sets. This composite dataset can be used to reconstruct a diffusion tensor at each voxel with a least squares linear regression. This process can then be repeated a large number of times (N_{boot} repetitions) to generate a distribution of diffusion tensors at each voxel. Eigensystem decomposition can then be performed on each diffusion tensor to determine their eigenvectors (E_1, E_2, and E_3) and eigenvalues (λ_1, λ_2, λ_3). Rotationally invariant quantities such as mean diffusivity (MD), factional anisotropy (FA), and tensor Mode [102] can also be extracted from each diffusion tensor, which describe tensor size (MD) and shape (FA, Mode).

The precision of each eigenvector, E_j can then be measured by first calculating the dyadic mean, ψ_j of the N_{boot} E_j vectors and measuring the angle, θ_j between each vector E_j and ψ_j. E_j precision (dE_j) can then characterized by the one-sided 95% confidence interval (95CI) of the resultant θ_j distribution. A one-sided 95CI is used because by definition $\theta_j \geq 0$. Note that dE1 as described here is exactly the cone of uncertainty as described by Jones in [128].

Analogous measures of tensor invariant precision can be determined by analyzing their distributions across the N_{boot} repetitions (as done for FA in [129]). Unlike the θ_j distributions describing vector uncertainties, which by definition are bounded between 0° and 90°, the invariants form two-sided distributions and can meaningfully exhibit negative deviations from the median value. As such, their uncertainty should be represented by a two-sided 95CI, which need not be symmetric about the median. The width of this 95CI (i.e. the upper bound minus the lower bound) can then be used to represent the underlying uncertainty (dMD, dFA, dMode).

6.3 Methods

6.3.1 cDTI Acquisition

cDTI were acquired in healthy volunteers (N=10) on a 3.0T scanner (Siemens Prisma, Erlangen Germany) using a spin echo EPI DWI pulse sequence with convex optimized diffusion encoding with first and second order moment compensation (CODE-M_1M_2) to reduce the echo time (TE) and thus improve SNR. The acquisition included two b-values (b=0 and 350s/mm^2) along 12 diffusion encoding directions with 2.0x2.0x5.0mm spatial resolution (TE=65ms, FOV=200x160mm, GRAPPA factor 2 [35], full-Fourier, water-only excitation). Local B_0 shimming was performed in a focused shim-box containing only the left ventricular (LV) myocardium to minimize susceptibility artifacts in the posterior wall. Imaging was timed to an end-expiratory respiratory phase using a liver-dome navigator trigger (TR=one respiratory cycle). Separate acquisitions were performed with ECG trigger delays timed to: 1) mid-systole (fixed trigger delay=100ms); and 2) late diastole (subject specific trigger delay determined from a balanced steady state free precession (bSSFP) cine image). 10 signal repetitions were acquired at each cardiac phase to facilitate bootstrapped uncertainty measurement for datasets containing up to 5 averages (scan time: ~10 minutes per cardiac phase).

6.3.2 Image Quality Evaluation

While SNR generally increases with additional signal averages (SNR $\propto \sqrt{N_{avg}}$), it can vary substantially in space and between subjects due to differences in subject geometry and coil positioning. It is thus useful to quantify voxel-wise image SNR in order to more precisely observe the relationship between SNR and cDTI uncertainty. Because ten repetitions of each image were acquired, it was possible to map SNR for each reference DWI (b=0) acquisition. In order to estimate SNR from images that included several averaged repetitions, a bootstrapped

approach similar to that described above was used. For example, for N_{avg}=5, five b=0 images were randomly chosen (with replacement) from the acquired set of ten and averaged together. This process was repeated to generate a set of 300 images that each included five averages. SNR was then calculated at each voxel by dividing the mean signal value across the 300 images by their standard deviation. SNR maps were generated in this manner for N_{avg}=1-10.

Because all pulse sequence parameters and set-up conditions were held constant between acquisitions at mid-systole and diastole, we can assume that any differences observed between the acquisitions arise from physiological variability. Furthermore, if cardiac bulk motion effects are present in the images, it is expected that they will vary subtly from beat to beat [59] and lead to signal fluctuation between repetitions. To quantify this effect, the coefficient of variation (i.e. the standard deviation normalized by the mean) of the image intensity across all 10 repetitions of each direction (CoV_{DTI}) was measured at each voxel for both cardiac phases.

6.3.3 cDTI Precision Measurement

Subsets of the set of 10 cDTI repetitions were first randomly selected and averaged together to reflect acquisitions with scan times ranging from approximately one to five minutes (N_{avg}=1 to N_{avg}=5). A second subset was then randomly generated for each case to facilitate bootstrapping. The uncertainty in tensor eigenvectors (dE_1, dE_2, dE_3) and invariants (dMD, dFA, dMode) was then measured from the two subsets as described above. These calculations used N_{boot}=1000 bootstrapped samples which was determined to be sufficient to generate stable statistical measures of uncertainty (i.e. increasing N_{boot} did not alter the measured tensor uncertainties) and is in line with previous studies [126].

Histograms of the uncertainty in each tensor quantity were generated for all LV voxels within each subject for N_{avg}=1 to N_{avg}=5 at both mid-systole and diastole. Median and maximum likelihood values were then extracted from each histogram. Global LV histograms of each

quantity's uncertainty were also generated from data pooled across all subjects at each cardiac phase.

Uncertainty was then characterized as a function of b=0 image SNR on a voxel-wise basis. This was done by first binning all voxels by SNR (bin size: 2) and generating histograms of uncertainty across all voxels contained in each SNR bin. The median uncertainty was then measured within each bin and the 95CI of the median was measured using bootstrapped histogram analysis. Significant differences between mid-systole and diastolic median uncertainties were identified by non-overlapping 95CIs.

In order to examine the impact of bulk motion induced signal attenuation on precision, the same process was then carried out to measure the median uncertainty of each parameter as a function of CoV_{DTI} (bin size: 2%).

6.3.4 Tensor Evolution with Varying Signal Averages

The dependence of eigenvector and tensor invariant parameters was also evaluated as a function of N_{avg}. To do so, diffusion tensors were reconstructed from cDTI image subsets including the full range of acquired signal averages (N_{avg}=1-10, note that all 10 averages could be used for this analysis because it did not require bootstrapped resampling). Maps of $\mathbf{E_1}$, $\mathbf{E_2}$, $\mathbf{E_3}$, MD, FA, and Mode were then generated for each subset.

Helix Angle (HA) maps were then generated by measuring the elevation angle of the projection of E_1 relative to the local circumferential tangent vector, **C** [49]. **C** was defined by a b-spline vector fit to the endo- and epicardial surfaces as defined by ten manually defined seed points on each surface [49]. The average HA slope across the wall, HA_{pitch} was calculated using a linear regression between HA and percent wall depth (PWD) for each subject. PWD values

were calculated at each LV voxel by linearly interpolating between the endo- and epicardial splines (where PWD=0% at the epicardial surface and 100% at the endocardial surface). Myocardial sheet angles, E2A and E3A were then defined by the angles between the circumferential-long axis plane and E_2 and E_3, respectively [49]. Median myocardial HA, |E2A|, and |E3A| were then calculated for each subject for N_{avg}=1-10. The median (μ) and standard deviations (σ) of myocardial MD, FA, and Mode were also calculated for each subject for N_{avg}=1-10. Statistical differences between each median and SD across all subjects as a function of N_{avg} were identified using one-way ANOVA. If ANOVA yielded significant differences, μ and σ from N_{avg}=1 were compared with N_{avg}≥2 using paired t-tests.

6.3.5 Cardiac Phase Dependence of Tensor Parameters

Median myocardial HA, HA_{pitch}, |E2A|, |E3A|, MD, FA, and Mode were also compared between mid-systole and diastole with N_{avg}=10 using paired t-tests.

6.4 Results

6.4.1 Image Quality Evaluation

All imaging experiments resulted in cDTI with sufficient quality to reconstruct diffusion tensors across the LV. The average heart beat duration (R-R interval) was 1006.1±101.4ms and the ECG trigger delays used for systolic and diastolic imaging were TD_{SYS}=100±0ms and TD_{DIA}=705±63ms. The average scan time was 9.1±3.1 minutes per cardiac phase (54.7±18.5 seconds per cDTI average).

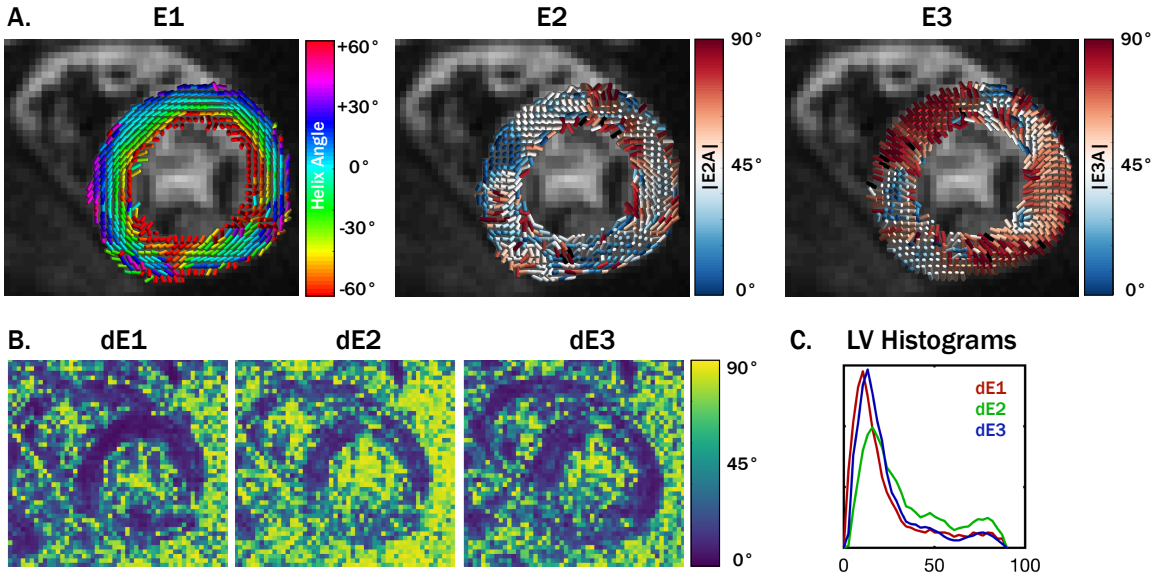

Figure 6.1: (A) Maps of eigenvector orientations for one subject from a mid-systolic cardiac phase with (B) corresponding eigenvector orientation 95CI uncertainty maps and (C) histograms of uncertainty within the LV. Qualitatively, regions with increased uncertainty correspond with regions of eigenvector incoherence. Overall, uncertainty in E_2 was greater than uncertainty in E_1 and E_3, a trend that was observed in all subjects.

The mean b=0 image SNR in the LV increased from 8.0±1.9 with N_{avg}=1 to 22.3±6.1 with N_{avg}=10. No significant differences in SNR were observed between mid-systolic and diastolic b=0 images (8.2±1.1 vs. 7.9±2.6, p=N.S.). However, median myocardial CoV_{DTI} was significantly lower in mid-systole than in diastole (16.7±2.2% vs. 25.8±9.1%, p=0.006), which indicates an increased sensitivity to bulk cardiac motion and a greater degree of variability in the diastolic phase.

6.4.2 cDTI Precision Measurement

Primary, secondary, and tertiary eigenvector (E_1, E_2, and E_3) maps along with eigenvector uncertainty maps (dE_1, dE_2, and dE_3) and myocardial uncertainty histograms are shown for a mid-systolic acquisition from a single subject in Figure 6.1. Qualitatively, regions with increased

uncertainty corresponded with regions with less coherent eigenvectors. cDTI images, and reconstructed maps of MD, FA, and Mode as well as maps of each parameter's uncertainty and histograms of myocardial uncertainty are shown for the same subject and cardiac phase in Figure 6.2.

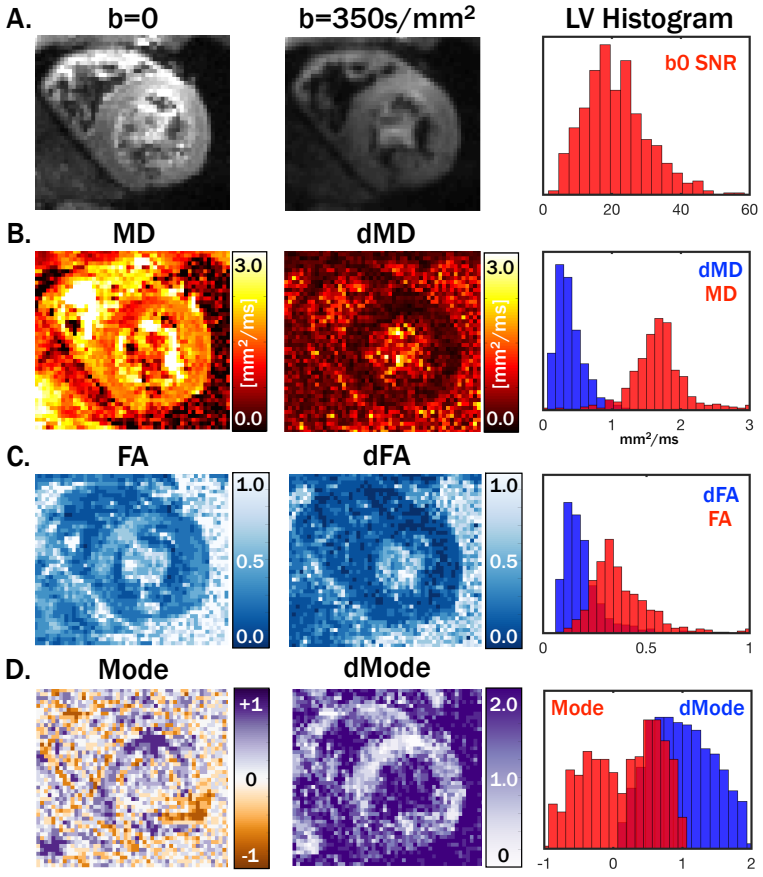

Figure 6.2: (A) Example images with b=0 and 350s/mm² from the subject shown in Figure 1 and a histogram of LV b0 SNR. Maps of tensor (B) MD, (C) FA, and (D) Mode with their corresponding uncertainties and LV histograms. dMD was low compared with myocardial MD values, while dFA was closer to myocardial FA and Mode was not well resolved with respect to dMode.

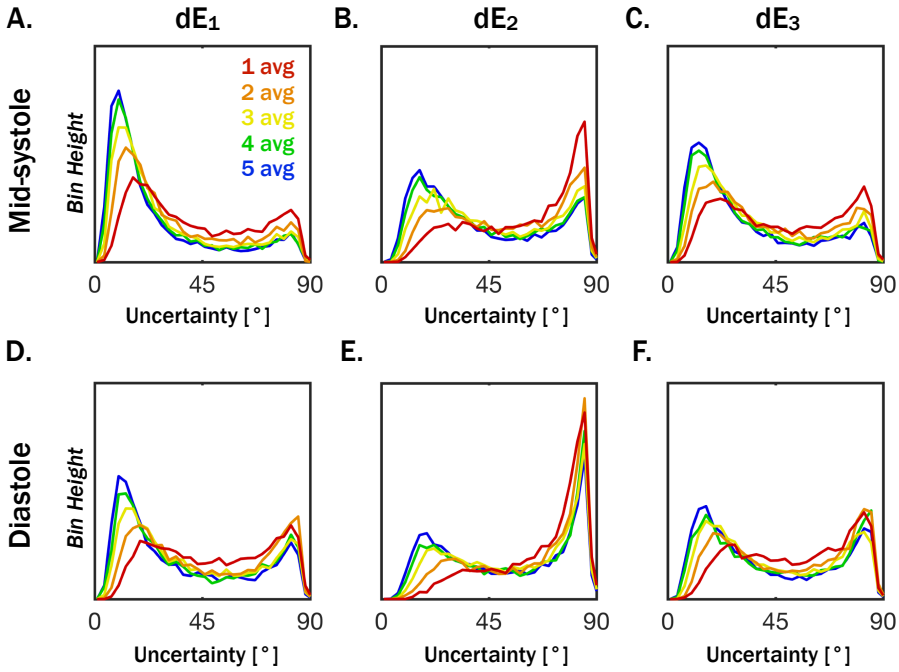

Figure 6.3: Histograms of uncertainty in tensor eigenvectors pooled from all LV voxels from all subjects at mid-systole (A,B,C) and diastole (D,E,F) from acquisitions with N_{avg}=1-5. Uncertainty decreased with additional signal averages, but differences were minimal for N_{avg}≥4. Uncertainty was larger for diastolic cDTI.

Histograms of tensor eigenvector uncertainty are shown in Figure 6.3 for mid-systolic and diastolic cDTI with N_{avg}=1-5 pooled across all subjects at systole (Figure 6.3A-C) and diastole (Figure 6.3D-F). Uncertainty decreased with additional signal averages, but differences were minimal for N_{avg}≥4. Uncertainty was generally larger for cDTI acquired in diastole than in mid-systole. Analogous histograms of tensor invariant uncertainty (MD, FA and Mode) are shown in Figure 6.4. Invariant uncertainty also decreased with increasing N_{avg}, but with minimal differences for N_{avg}≥4. Differences in tensor invariant uncertainty histograms between mid-systolic and diastolic cDTI were minimal.

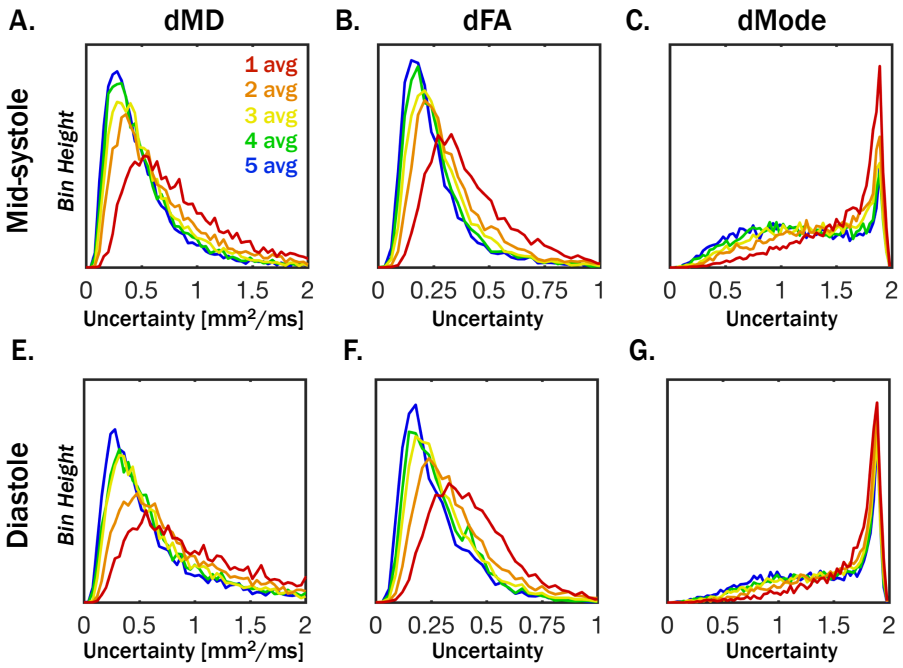

Figure 6.4: Histograms of uncertainty in tensor invariants pooled from all LV voxels from all subjects at (A,B,C) mid-systole and (D,E,F) diastole from acquisitions with N_{avg}=1-5. Differences between mid-systolic and diastolic cDTI were minimal and all uncertainties reduced with increasing N_{avg}. However, only minimal differences were observed between N_{avg}=4 and 5.

The median and maximum likelihood values from the uncertainty histograms generated for each subject are shown for N_{avg}=5 in Table 6.1. Median and maximum likelihood uncertainties were lower in mid-systole than in diastole for all parameters.

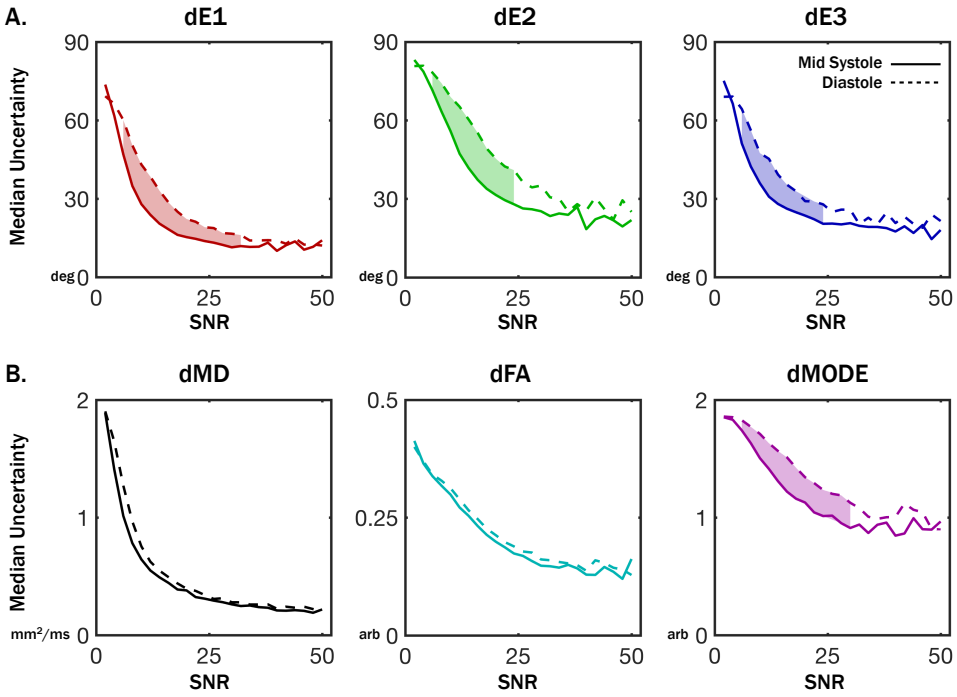

Figure 6.5: Plots of median uncertainty in (A) tensor eigenvalues and (B) invariants as a function of b0 image SNR at mid-systole (solid lines) and diastole (dotted lines). Median uncertainties and 95CI of the medians (not shown) were calculated from uncertainty distributions across all voxels and subjects with a particular b0 SNR (binned in SNR increments of 1) across images with N_{avg}=1-5. Significant differences between mid-systole and diastole were identified by non-overlapping 95CIs and are indicated by shaded regions between the plots. dE_1, dE_2, dE_3, and dMode were significantly lower at mid-systole for moderate SNRs. No significant differences in dMD or dFA were observed between phases.

		dE1 degree	dE2 degree	dE3 degree	dMD mm^2/ms	dFA unitless	dMode unitless
Mid-systole	Max Likelihood	9.7±1.0	15.7±1.0	12.1±1.5	0.25±0.02	0.13±0.01	1.62±0.47
	Median	15.5±1.2	31.2±3.5	21.8±3.1	0.38±0.02	0.20±0.01	1.10±0.08
Diastole	Max Likelihood	17.8±21.6	84.1±1.5	42.7±33.2	0.28±0.07	0.16±0.003	1.88±0.02
	Median	31.9±7.1	59.6±6.8	40.5±6.4	0.52±0.09	0.23±0.01	1.57±0.11

Table 6.1: Mean ± SD from N=10 subjects of uncertainty histogram maximum likelihoods and medians with N_{avg}=5.

Median eigenvector and invariant uncertainties are plotted as functions of b0 in Figure 6.5. Uncertainty in all measured parameters dropped consistently with increasing SNR. Uncertainty dropped faster with respect to SNR for mid-systolic data, particularly in dE_1, dE_2, dE_3, and dMode where significant differences were observed between phases for intermediate SNRs as highlighted in Figure 6.5. While the maximum observed SNR across all subjects and voxels was 95, histograms were only generated for SNR≤50 due to a lack of sufficient data for meaningful statistics as seen in the histograms of b=0 SNR pooled across all subjects and cardiac phases which are plotted for N_{avg}=1-5 in Figure 6.6.

Median uncertainty values were plotted as functions of CoV_{DTI} in Figure 6.7. There were clear increases in uncertainty for all parameters with increasing CoV_{DTI}. Figure 6.7C shows global histograms of CoV_{DTI}, which demonstrates the increased CoV_{DTI} in the diastolic phase.

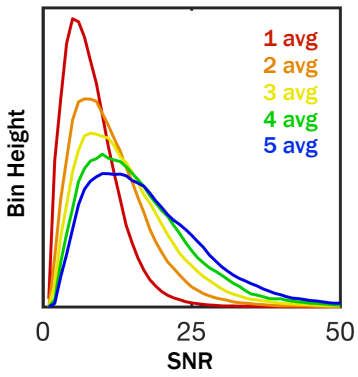

Figure 6.6: Histograms of b0 image SNR within the LV with N_{avg}=1-5 for all subjects and phases. Median (±95CI) SNR increased from 7.4±0.3 with N_{avg}=1 to 16.7±0.7 with N_{avg}=5.

6.4.3 Tensor Evolution with Varying Signal Averages

Differences in HA, HA_{pitch}, |E2A|, or |E3A| across signal averages at either mid-systole or diastole were not significant. Median myocardial values are tabulated for each parameter in Table 6.2.

Median (μ) and standard deviations (σ) of MD, FA, and Mode across the LV myocardium are plotted for all subjects as functions of N_{avg} in Figure 6.8. No significant changes in μ_{MD} were observed between any number of averages at either mid-systole or diastole. Compared with N_{avg}=1, σ_{MD} decreased significantly with $N_{avg}\geq 2$ in mid-systole ($\sigma_{MD,1avg}$=0.95±0.2mm^2/ms vs. $\sigma_{MD,2avg}$=0.67±0.2mm^2/ms, p=8x10^{-4}) and with $N_{avg}\geq 6$ in diastole ($\sigma_{MD,1avg}$=1.39±1.1mm^2/ms vs. $\sigma_{MD,6avg}$=0.63±0.2mm^2/ms, p=0.05).

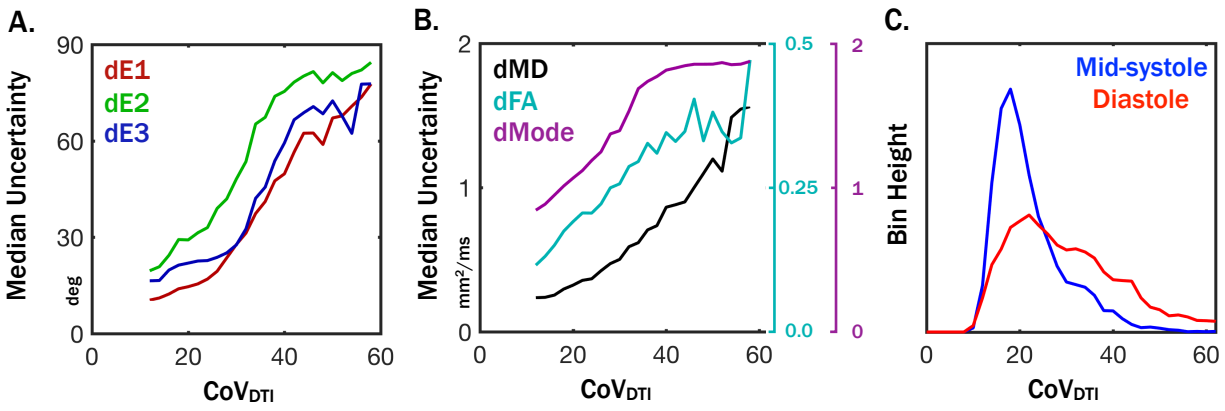

Figure 6.7: Plots of median uncertainty in (A) tensor eigenvalues and (B) invariants as a function of CoV_{DTI} with N_{avg}=5 and pooled across all subjects and cardiac phases as well as (C) histograms of CoV_{DTI} from mid-systole and diastole. Median values were calculated from uncertainty distributions across all voxels and subjects with a particular CoV_{DTI} (binned in increments of 1%). Uncertainty in all parameters increased with increasing CoV_{DTI} indicating a connection with bulk-motion induced signal variations. This likely explains the increased uncertainty observed in diastolic cDTI parameters, which had significantly higher CoV_{DTI}.

Compared with N_{avg}=1, μFA decreased significantly with $N_{avg}\geq 3$ at both mid-systole ($\mu_{FA,1avg}$=0.46±0.05 vs. $\mu_{FA,3avg}$=0.41±0.04, p=0.01) and diastole ($\mu_{FA,1avg}$=0.48±0.08 vs. $\mu_{FA,3avg}$=0.38±0.06, p=4x10^{-3}). Compared with N_{avg}=1, σ_{FA} decreased significantly with $N_{avg}\geq 2$ in mid-systole ($\sigma_{FA,1avg}$=0.24±0.03 vs. $\sigma_{FA,2avg}$=0.21±0.03, p=0.03) and with $N_{avg}\geq 3$ in diastole ($\sigma_{FA,1avg}$=0.22±0.03 vs. $\sigma_{FA,3avg}$=0.18±0.04, p=0.01).

A significant increase in Mode was observed in mid-systole with N_{avg}≥4 compared with N_{avg}=1 ($\mu_{Mode,1avg}$=0.22±0.6 vs. $\mu_{Mode,4avg}$=0.31±0.9, p=0.02). Compared with N_{avg}=1, σ_{Mode} decreased significantly with N_{avg}≥3 in mid-systole ($\sigma_{Mode,1avg}$=0.57±0.02 vs. $\sigma_{Mode,1avg}$=0.56±0.01, p=0.03). No corresponding significant differences were observed in diastole.

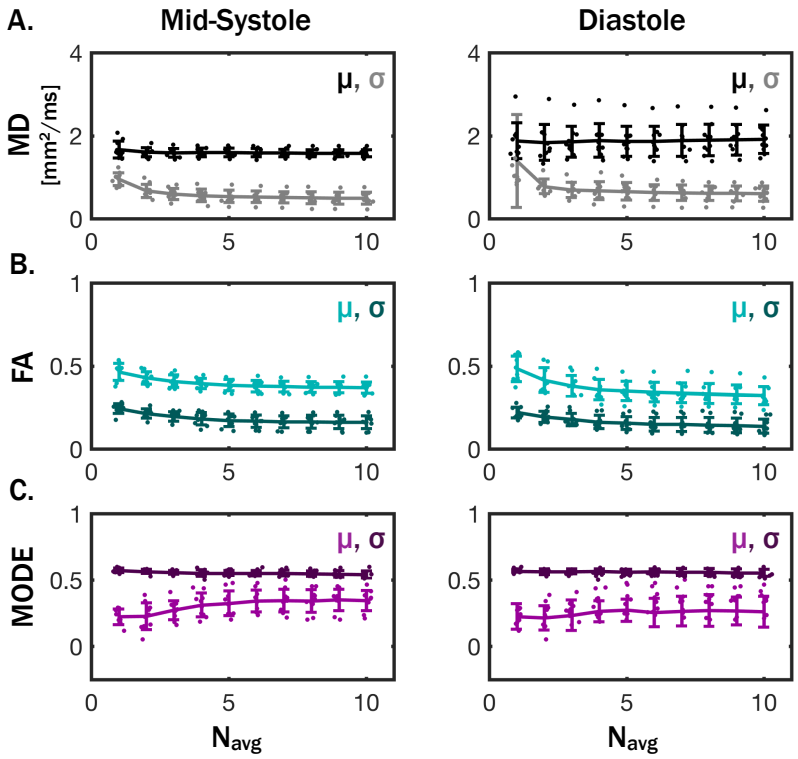

Figure 6.8: LV medians (μ) and SDs (σ) of MD (A), FA (B), and Mode (C) from mid-systolic (left) and diastolic (right) cDTI with N_{avg}=1-10. Lines and error bars represent the mean and SDs across all subjects and dots represent individual subject values. LV SDs decreased with increasing N_{avg} for all parameters but with diminishing changes with N_{avg}≥4. Median FA values decreased with increasing N_{avg} while median Mode values increased. Median MD values did not change with increasing N_{avg}.

6.4.4 Cardiac Phase Dependence of Tensor Parameters

With N_{avg}=10, median myocardial MD was significantly lower in mid-systole than in diastole (MD_{SYS}=1.58±0.09mm^2/ms vs. MD_{DIA}=1.91±0.34mm^2/ms, p=8x10^{-3}) whereas FA was significantly higher in mid-systole (FA_{SYS}=0.37±0.03 vs. FA_{DIA}=0.32±0.06, p=0.03). No significant differences were observed between cardiac phases for any of the other parameters examined.

6.5 Discussion

The observed increase in bulk motion effects and tensor precision in diastolic cDTI compared with mid-systolic cDTI is consistent with previous reports of the second order motion compensated diffusion encoding scheme [20]. M_1+M_2 nulled diffusion encoding relies on an assumption that cardiac motion can be well described by a second order polynomial (i.e. only velocity and acceleration terms). Systolic (contractile) motion is highly coherent and thus closely conforms to this assumption and is largely compensated by the CODE M_1+M_2 nulled gradient waveform. Contractile motion is also very consistent from beat to beat and over a range of heart rates which limits inter-shot motion fluctuations over the course of an acquisition (i.e. low CoV). On the other hand, diastolic motion, though smaller in magnitude, does not meet the second order assumption as closely and thus is not fully compensated by the M_1+M_2 nulling. Furthermore, it is highly dependent on beat to beat variations and changes in heart rate which leads to substantial deviations in the cDTI signal during an acquisition (i.e. higher CoV). This is reflected in the strong correlation between uncertainty and CoV_{DTI}, which is an indicator of bulk-motion artifacts, and the increased CoV_{DTI} in diastolic imaging (Figure 6.7).

It is possible that the uncertainty in diastolic diffusion tensors could have been reduced by employing specialized image post processing algorithms to remove bulk-motion image artifacts such as constrained reconstruction [104] or maximum intensity projection [59, 60].

These correction strategies would likely reduce the effects of physiological variability, but would not permit the SNR gains from signal averaging.

		N_{avg}=1	N_{avg}=5	N_{avg}=10
Mid-systole	HA	3.8±3.5°	1.88±3.8°	1.6±3.1°
	HA_{pitch}	-1.2±0.2°/%	-1.2±0.2°/%	-1.2±0.2°/%
	|E2A|	40.9±5.7°	38.2±5.5°	36.6±6.0°
	|E3A|	61.7±4.3°	65.2±5.5°	66.5±4.8°
Diastole	HA	4.2±4.5°	1.9±3.4°	1.14±4.1°
	HA_{pitch}	-1.3±0.2°/%	-1.3±0.3°/%	-1.24±0.1°/%
	|E2A|	41.2±7.5°	37.8±9.9°	35.0±10.7°
	|E3A|	64.7±7.1°	67.8±7.7°	68.9±8.1°

Table 6.2: Mean ± SD from N=10 subjects of global median eigenvector orientation metrics with Navg=1, 5, and 10.

Uncertainty varied substantially between tensor parameters and was lowest for E_1, MD, and FA and largest for E_2, E_3, and Mode. This indicates that SNR and scan time requirements vary depending on the parameters of interest in a given study. To contextualize these uncertainties, it is useful to consider examples of expected physiological variability. For example, the global HA_{pitch} value of 1.2±0.2°/% observed in this work (which are in line with other *in vivo* studies [15, 66]) indicate an inherent range of fiber orientations present in each imaging voxel. Assuming an LV wall thickness of 15mm and 2.0mm in-plane spatial resolution, each voxel will occupy approximately 13% of wall depth. Consequently, each voxel should contain a range of fiber orientations which vary by as much as 15° thus placing a reasonable upper bound on the expected precision of E_1. For a 5 minute acquisition (5 averages, SNR~18), the maximum likelihood for E_1 precision was within this bound for mid-systolic cDTI: dE_1=9.7±1.0° (median dE_1=15.4±1.2°). To reach median E_1 uncertainties within 15°, our data

indicates that an SNR of at least 22 (Figure 6.5A) is required, which corresponds to an acquisition with ~8 averages (scan time ~8min).

In comparison to our observed eigenvector uncertainties, an *ex vivo* study of cDTI in rat hearts reported mean dE_1, dE_2, and dE_3 values of 3.7°±0.2°, 10.9°±0.4°, and 10.6°±0.5°, respectively [126]. However, this study was performed at high field (9.4T), employed gradients capable of amplitudes >10x of standard clinical hardware (1T/m) and did not contend with physiological motion. Furthermore the 0.1mm spatial resolution protocol resulted in substantially lower range of fiber orientations and thus less physiological variability within each voxel.

Notably, the uncertainty in E_2 was consistently greater than the uncertainty in E_3. This is surprising because E_2, by definition, has a larger eigenvalue than E_3. This behavior was also reported by Teh *et al*. [126]. One possible explanation for this is the orthogonality enforced by the eigensystem tensor decomposition. This implies that once E_1 and E_2 are determined for a system, E_3 is automatically oriented normal to the E_1-E_2 plane, which could result in the observed E_3 uncertainties that lie between those of E_1 and E_2.

Another example of expected physiological diffusion tensor variability is the 0.9mm^2/ms MD increase observed in myocardial infarcts compared with healthy tissue observed by Nguyen et al. [65]. MD precision should thus be sufficiently small to detect this difference for the purpose of identifying infarcts. The median MD uncertainty was within this difference for even just one average in mid-systole (median dMD=0.73±0.04mm^2/ms). However, the uncertainty histogram for one average (Figure 6.4) shows that nearly 40% of voxels exhibited MD uncertainties ≥0.9mm^2/ms, a number that reduced to just 11% with five averages (median dMD=0.38±0.02mm^2/ms).

Our results indicate that little benefit in precision is achieved by increasing SNR beyond approximately 25 (Figure 6.5), which, in this study this corresponded to an approximately 10 minute long acquisition (i.e. ten averages). Note, that this study was conducted on a 3.0T

clinical system with high performance gradient hardware (G_{max}=76mT/m), which reduces the minimum TE (65ms) for the cDTI protocol compared with more commonly available gradient hardware sets (G_{max}=40mT/m, TE_{Min}=85ms). The baseline SNR on these systems will consequently be lower than those reported here and would thus require longer scans to achieve the same degree of uncertainty. Further scan time increases would also be required for imaging at 1.5T.

Conversely, no significant changes in median myocardial tensor parameters or their standard deviations were achieved by increasing scan time beyond approximately 4 minutes, which corresponded with b0 image SNR=16.0±3.8 (i.e. four averages, Figure 6.8). With low SNR (N_{avg}<4), we observed an upward bias in FA and a downward bias in Mode, which are both consistent with published reports based on numerical simulations [102]. Notably, no significant differences in median MD were observed for any number of signal averages. This indicates that MD measurement accuracy is very robust to variability and does not require long scan times.

The only significant differences observed between cardiac phases were an increase in MD and a decrease FA in diastole relative to mid-systole. It is likely that the increase in MD in diastole stems from the increased bulk motion sensitivity in this phase [20]. The FA decrease may be due to an increase in myocardial blood volume in diastole, which contributes an isotropic diffusive compartment. However, this comes in contrast to the increase in FA in diastole measured with STEAM cDTI [137].

The |E2A| steepening in diastole compared with peak-systole that has been previously observed was not observed in this study. This may arise, in part, because the mid-systolic phase does not correspond with a fully contracted myocardium, which limits the observable differences in sheetlet mobility. Furthermore, the relatively large E_2 uncertainties indicate this method may not be as sensitive to sheetlet mobility, possibly because of the short diffusion times of the CODE-M_1M_2 sequence.

This study only examines the precision in spin echo EPI cDTI. Substantial differences may be observed in STEAM cDTI, which generally reports higher FA (FA_{STEAM}~0.5-0.6 [137, 138] vs. FA_{SE}~0.3-0.4 reported here and elsewhere [138]) values than spin echo data due to the longer diffusion "mixing times" that allow diffusing molecules to probe larger length scales during diffusion encoding. The higher effective FA will likely reduce the inherent uncertainty in E_1. However, STEAM cDTI has half the baseline SNR of spin echo cDTI and also double the scan time due to the need for two heartbeats per diffusion encode, which results in lower SNR efficiency [138]. However, currently it is unclear how the tradeoffs between FA and SNR efficiency affect the relative tensor uncertainty from these pulse sequences.

The number of unique diffusion encoding gradient orientations sampled in a DTI acquisition also impacts measurement precision [131]. While neurological studies provide guidance in this regard (the 12-direction sampling scheme was used based on such guidance [131]), it remains an open question whether additional signal averages or diffusion encoding directions more efficiently improve the precision of *in vivo* cDTI. Furthermore, it is unclear how to best employ EPI acceleration techniques such as parallel imaging and partial Fourier, which have complex relationships with image SNR in that they reduce SNR efficiency but often permit shorter TEs. Partial fourier also has the added effect of increasing bulk motion sensitivity [100].

It would be interesting to observe the progression of tensor precision with $N_{avg}>5$, but the bootstrapped technique used in this work requires a repeated acquisition and thus can only quantify uncertainties for datasets containing half of the acquired 10 averages. Model-based techniques such as the wild bootstrap [139], however, can quantify precision without a repeated acquisition, but require assumptions of the underlying uncertainties. It is unclear whether these approaches can be successfully applied to *in vivo* cDTI and they have not been examined in this work.

6.6 Conclusion

Diffusion tensor precision was evaluated for *in vivo* spin echo cDTI using motion compensated CODE-M_1M_2 diffusion encoding. Acceptable levels of precision in E_1, MD, and FA were achieved in a four to five minute (per slice) free breathing scan. Increased uncertainty during diastolic acquisitions indicate that bulk cardiac motion can still confound measurements made with first and second order motion compensation.

6.7 Acknowledgements

This work was supported, in part, by the Graduate Program in Bioscience at UCLA, the Department of Radiological Sciences at UCLA, NIH R01HL131975 and AHA 16PRE27380023.

7 EDDY CURRENT NULLED CONVEX OPTIMIZED DIFFUSION ENCODING

In this chapter, we modify the Convex Optimized Diffusion Encoding (CODE) framework to generate optimized gradient waveforms that reduce image distortions by nullifying the eddy currents that are produced in conductive MRI hardware components during gradient ramps. Eddy current nulled CODE (EN-CODE) gradient design is accomplished by incorporating an exponential eddy current decay model as an additional constraint in the optimization problem. We demonstrate that EN-CODE can reduce eddy current induced image distortions to a degree equivalent to the established twice refocused spin echo (TRSE) pulse sequence but with substantially shorter echo times in most situations. EN-CODE also achieves similar echo times to traditional monopolar diffusion encoding, which suffers from severe eddy current induced image distortions. This work was previously published in *Magnetic Resonance in Medicine* in 2017: *Aliotta E, Moulin K, Ennis DB, Eddy Current Nulled Convex Optimized Diffusion Encoding (EN-CODE) for Distortion-Free Diffusion Tensor Imaging with Short Echo Times. MRM; 2017 doi: 10.1002/mrm.26709.*

7.1 Abstract

Purpose: To design and evaluate eddy current nulled convex optimized diffusion encoding (EN-CODE) gradient waveforms for efficient diffusion tensor imaging (DTI) that is free of eddy current induced image distortions.

Methods: The EN-CODE framework was used to generate diffusion encoding waveforms that are eddy current compensated. EN-CODE DTI was compared with the existing eddy current nulled twice refocused spin echo (TRSE) sequence as well as monopolar (MONO) and non-eddy current compensated CODE in terms of echo time (TE) and image distortions. Comparisons were made in simulations, phantom experiments and neuro imaging in ten healthy volunteers.

Results: EN-CODE achieved eddy current compensation with a significantly shorter TE than TRSE (78ms vs. 96ms) and a slightly shorter TE than MONO (78ms vs. 80ms). Intravoxel signal variance was lower in phantoms with EN-CODE than with MONO (13.6±11.6vs.37.4±25.8) and not different from TRSE (15.1±11.6) indicating good robustness to eddy current induced image distortions. Mean FA values in brain edges were also significantly lower with EN-CODE than with MONO (0.16±0.01vs.0.24±0.02, $p<1x10^{-5}$) and not different from TRSE (0.16±0.01vs.0.16±0.01, p=N.S.).

Conclusion: EN-CODE eliminated eddy current induced image distortions in DTI with a TE comparable to MONO and substantially shorter than TRSE.

7.2 Introduction

Diffusion weighted imaging (DWI) uses large amplitude gradient pulses to impart sensitivity to diffusion in the MRI signal amplitude. These same gradients, however, induce eddy currents within conductive hardware components in the MRI system, which generate additional magnetic

fields. The use of active gradient coil shielding [140-142], advanced gradient coil designs [143] and gradient pre-emphasis corrections [144, 145] has reduced the magnitude and impact of eddy currents, but they can still lead to substantial image distortions with the large amplitude gradient pulses used in DWI. These image distortions are especially apparent in echo planar imaging (EPI) — the readout most commonly used in both DWI and diffusion tensor imaging (DTI) — which is particularly sensitive to magnetic field perturbations. Within a specific protocol, eddy current induced image distortions are dependent on the direction and magnitude (i.e. b-value) of the diffusion encoding gradients, which leads to mis-registration between different DWI and confounds diffusion tensor reconstruction if not carefully corrected for in post-processing [46, 146].

In addition to improved gradient hardware and post-processing methods, modified pulse sequence approaches are another solution strategy. For example, the twice refocused spin echo (TRSE) pulse sequence [147] significantly reduces eddy current induced image distortions. TRSE balances the eddy currents produced by each diffusion encoding gradient ramp by using a bipolar gradient encoding design and an additional refocusing pulse. TRSE is an effective technique for mitigating eddy current induced distortions, but it significantly increases echo times (TE) compared with conventional monopolar (MONO) encoding. This is particularly true for low to moderate b-values ($b \leq 1000 s/mm^2$) and long EPI readouts (≥50ms, i.e. high spatial resolution imaging). The use of two refocusing pulses also enhances sensitivity to B_1 imperfections and increases SAR deposition [148].

Recently, Convex Optimized Diffusion Encoding (CODE) was described as a framework for generating time-optimal (minimum TE) gradient waveforms for spin echo EPI (SE-EPI) DWI [20]. CODE formulates the design of the diffusion encoding gradient waveforms as a constrained (i.e. gradient hardware limits, pulse sequence timing constraints, b-value, and gradient moment requirements) convex optimization problem. Consequently, CODE can

efficiently determine the diffusion encoding gradient waveform that optimally satisfies all requirements and produces the shortest TE.

In this work, the CODE framework was used to design eddy current compensated diffusion encoding gradient waveforms for DTI that is free of eddy current image distortions with a single refocusing pulse. To do so, an additional eddy current nulling constraint was incorporated into the CODE optimization framework. The resultant eddy current nulled convex optimized diffusion encoding (EN-CODE) gradient waveforms shorten TE compared with both TRSE and MONO DTI, particularly for low b-values and high spatial resolution imaging. EN-CODE was evaluated using eddy current simulations as well as imaging in both phantoms and healthy volunteers.

7.3 Theory

7.3.1 CODE Optimization Framework

The previously reported CODE framework employs convex optimization to design diffusion encoding gradient waveforms that minimize TE in SE-EPI DWI for a given b-value with no explicit constraint on gradient waveform shape or symmetry [20]. Minimum TE waveforms are achieved by first maximizing the b-value (b) for any particular sequence timing, which is given by:

$$b = \gamma^2 \int_0^{T_{Diff}} F(t)^2 dt \qquad 7.1$$

where γ is the gyromagnetic ratio of ^{1}H, T_{Diff} is the time corresponding to the end of diffusion encoding and:

$$F(t) = \int_0^t G(\tau)d\tau \tag{7.2}$$

where the time t=0 corresponds with the center of the excitation pulse.

However, because the b-value (Eqn. **7**.**1**) is a convex and non-unique functional of G(t), it does not contain a single maximum that can be determined through convex optimization. To facilitate convex optimization, the objective function can be reformulated by defining the function, β:

$$\beta = \int_0^{T_{Diff}} F(t)dt \tag{7.3}$$

The magnitude of β corresponds directly with the b-value, but it is a concave functional of G(t) (i.e. its second variation is negative definite [90]); and thus contains a unique maximum that can be determined using convex optimization. Consequently, the gradient waveform G(t) that maximizes β (and thus the b-value) can be determined using the following objective function:

$$G(t) = \arg\max_G \beta(G) \tag{7.4}$$

G(t) is defined discretely and arbitrarily on t = m•dt where m is an integer number of gradient time points and dt is the temporal discretization of the optimization.

7.3.2 Optimization Constraints

In addition to maximizing the b-value, CODE diffusion encoding gradient waveforms must also be achievable on an MRI system. Therefore, the CODE optimization includes three constraints: 1) *Pulse sequence timing constraints* to ensure that gradients are off during periods of RF activity and during readout; 2) *Gradient moment constraints* to ensure that the total gradient area (i.e. M_0) is zero and that higher order gradient moments (M_1, M_2) for motion compensated diffusion encoding are zero as needed (M_1 and M_2 were not nulled in the present study); and 3)

Hardware constraints to limit the gradient waveform design to operate within gradient amplitude and slewrate limits. EN-CODE adds a fourth constraint on the diffusion encoding gradient waveform for *eddy current nulling*.

7.3.3 Eddy Current Model

Eddy currents are generated within various conductive MRI hardware components during the application of time-varying gradient pulses. Eddy currents predominantly exhibit exponential decay over time and can be modeled as a resistive-inductive (RL) circuit. The eddy currents generated during equivalent gradient ramp-up and ramp-down intervals (e.g. in a trapezoidal gradient waveform) are equal in magnitude and opposite in direction. Exponential decay of the eddy currents generated at earlier time points, however, leads to imperfect cancellation and a non-zero superposition of the eddy current induced magnetic fields (B_{EC}). These magnetic fields can persist during the EPI readout and result in deviations from the target *k*-space trajectory and substantial image distortions. By modeling the induced eddy currents with a RL-circuit B_{EC} from an arbitrary gradient waveform, G(t), can be described as follows [26]:

$$B_{EC}(t) = \sum_i w(\lambda_i)(\frac{dG}{dt} * e^{-\frac{t}{\lambda}_i}) \quad 7.5$$

Where * is the convolution operator, λ_i are the time constants of eddy current decay, and w is a system-dependent scaling factor for each λ_i. Previous approaches have effectively eliminated eddy current induced image distortions by compensating for a single λ [147, 149]. Considering only a single λ reduces the problem:

$$B_{EC}(\lambda, t) = w(\lambda)\frac{dG}{dt} * e^{-\frac{t}{\lambda}} \quad 7.6$$

In general, w is scanner-dependent scalar value, but it is not necessary to know the value in order to null eddy currents for any single λ, if the convolution term can be minimized at a

specific time. Therefore, a new function is defined that is proportional to B_{EC}, but independent of w:

$$\varepsilon(\lambda, t) = \frac{dG}{dt} * e^{-\frac{t}{\lambda}} \quad 7.7$$

An *eddy current nulling* constraint can then be defined using Eqn. **7**.**7**:

$$\varepsilon(\lambda_{null}, T_{Diff}) = 0 \quad 7.8$$

where λ_{null} is the target decay constant to be nulled. Importantly, nulling eddy currents at T_{Diff} ensures that eddy current contributions from the diffusion encoding gradient waveform are zero for all $t \geq T_{Diff}$.

Comparing the magnitude of eddy current induced artifacts between two different pulse sequences is typically an empirical exercise. Note, however, that Eqn. **7**.**7** can also be used to define the eddy current characteristics of any diffusion encoding gradient waveform, which we term the *eddy current spectrum*. By calculating ε(λ,t) over a range of λ and at the end of diffusion encoding (T_{Diff}) the *eddy current spectrum* can be compared between different diffusion encoding gradient waveforms. Importantly, because w is not included in this formulation, the eddy current spectrum is system invariant.

7.3.4 Solution Strategy

The time optimal EN-CODE gradient waveforms are determined by finding the minimum TE for which a gradient waveform exists that is consistent with all constraints and reaches the desired b-value. This is efficiently accomplished using a binary search through a TE search space with each iteration of Eqn. 4 [88, 108]. Upper and lower limits on TE (TE_U and TE_L) are first defined to initialize the optimization. TE_U is defined by the TE of MONO plus 20ms, which was a suitable upper bound in all cases examined. TE_L is defined by the TE of a spin echo sequence without

diffusion encoding gradients, which has a minimum TE of $T_{180}+2T_{\varepsilon}$ where T_{ε} is the duration of the EPI readout before the spin echo (exactly half of the readout time for full-Fourier imaging) and T_{180} is the refocusing pulse duration.

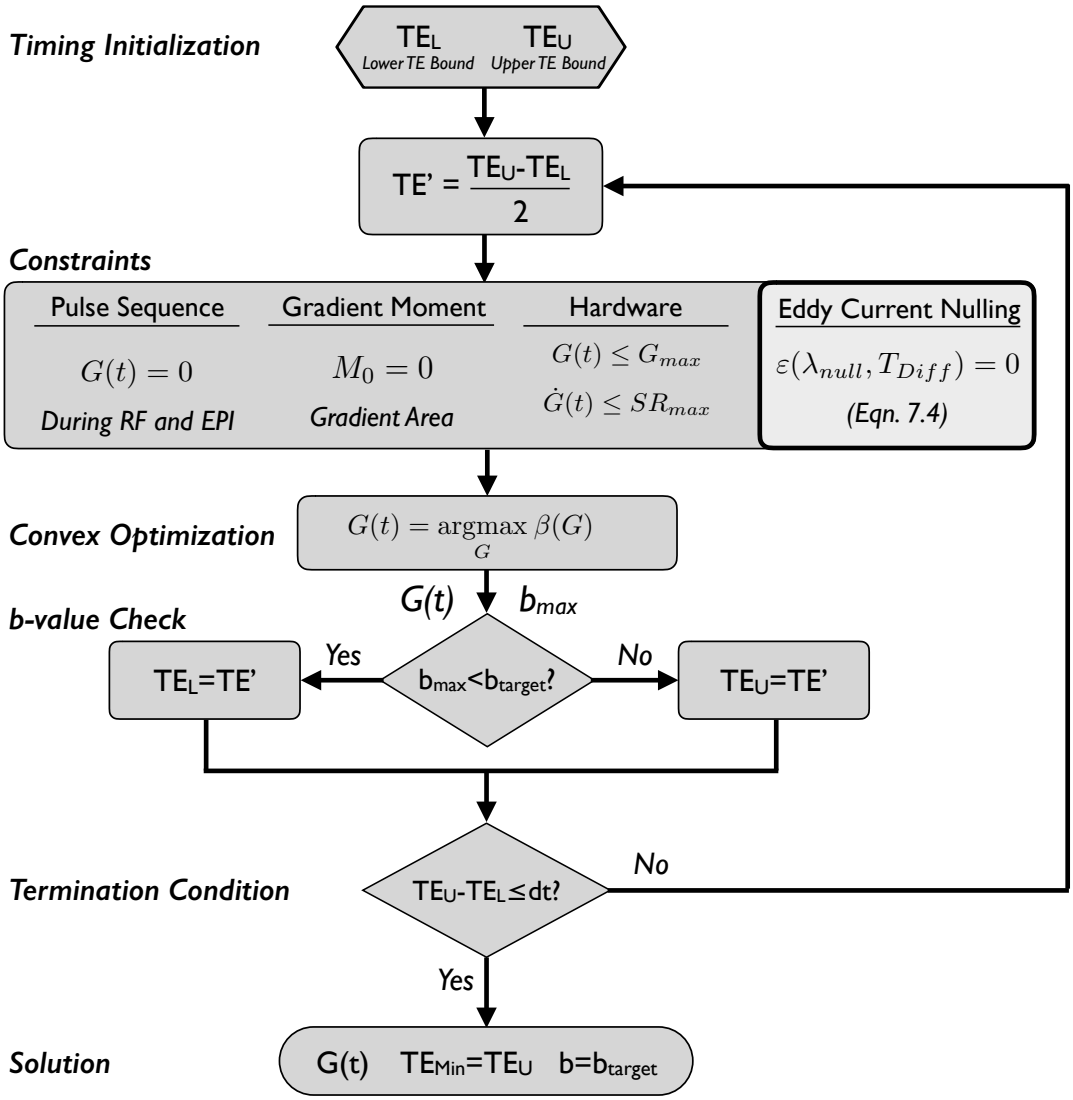

*Figure 7.1: EN-CODE gradient optimization algorithm. The time optimal solution is determined by finding the minimum TE for which a diffusion encoding gradient waveform that is both consistent with all constraints and achieves the target b-value (b_{target}) exists. Successive binary searches divide the TE search space with each call of the convex solver. The function β (Eqn. **7.4**) is directly related to the b-value (i.e. maximizing β also maximized b-value) and is compatible with convex*

optimization. The EN-CODE algorithm is equivalent to the previously described CODE algorithm with the added eddy current nulling constraint.

7.4 Methods

7.4.1 Simulations

EN-CODE diffusion encoding gradient waveforms were designed with a range of individual λ_{null} (10ms to 100ms, $\Delta\lambda_{null}$=10ms) using the algorithm shown in Figure 1. This range of λ_{null} values was chosen to match the time scale of the DWI pulse sequence and corresponds with values that have been previously shown to be relevant on a clinical MRI system [147-149]. The simulated pulse sequence parameters were b=1000s/mm^2, bandwidth=1852Hz/pixel (0.6ms echo spacing), T_ε=27.5ms and T_{180}=5.2ms, corresponding with a neuro DTI protocol with 1.7mm in plane resolution and a 300x300mm field of view (FOV) which was subsequently used for phantom and *in vivo* imaging. Hardware constraints were defined for a 3T MRI scanner with high performance gradients (G_{max}=80mT/m and SR_{max}=200T/m/s), but with G_{max} limited to 76mT/m and SR_{max} limited to 50T/m/s to limit peripheral nerve stimulation during diffusion encoding. All optimizations were performed in MATLAB (Mathworks, Natick, MA, USA) using the CPLEX linear solver (IBM, Armonk, NY, USA) and the YALMIP toolbox [91] with a time-step dt=100μs that maintained EN-CODE gradient waveform computation times to <5min without notably impacting the minimum possible TE.

Analogous TRSE diffusion encoding gradient waveforms were also designed using the same pulse sequence parameters and hardware constraints and with the same λ_{null} values used for EN-CODE. Conventional MONO waveforms and non-eddy current compensated CODE waveforms were also designed. Eddy current spectra were then simulated for each diffusion

encoding gradient waveform using Eqn. **7.7** for a range of λ (0ms to 100ms, Δλ=1ms) and T_{Diff} matched to each sequence.

TE differences between EN-CODE and alternative diffusion encoding methods were also evaluated. Minimum TEs were compared over a range of b-values (200 to 2000s/mm^2) and T_ε (10-60ms) (corresponding to roughly 0.5 to 3.0mm isotropic in-plane resolution, with full-Fourier symmetric *k*-space coverage) using: 1) TRSE with λ_{null}=80ms; 2) EN-CODE with λ_{null}=80ms; and 3) MONO. λ_{null}=80ms was used based on the findings of the phantom imaging experiments shown below.

7.4.2 Phantom Imaging

Phantom experiments were performed to evaluate eddy current induced image distortions between diffusion encoding methods and to determine the optimal λ_{null} for our system. A phantom containing 50mL conical tubes (diameter 5.5cm) of water submerged in a susceptibility-matched fluid with a negligible MRI signal (Fomblin, Solvay Solexis, West Deptford, NJ) was imaged using a 3T scanner (Prisma, Siemens, Erlangen, Germany). DWI were acquired with b=1000s/mm^2 along six diffusion encoding directions (±x,±y,±z), 1.7x1.7x5mm spatial resolution (T_ε=27.5ms), 15 interleaved slices, parallel imaging acceleration factor of two with GRAPPA [35], five averages to improve SNR, and TR=2300ms (Table 7.1). All acquisition parameters were matched, except TE, for all diffusion encoding schemes: 1) MONO (TE=80ms); 2) CODE (TE=71ms); 3) TRSE with λ_{null}=20-100ms (TE=96ms); and 4) EN-CODE with λ_{null}=10-100ms (TE=76-78ms). A $\Delta\lambda_{null}$ of 10ms was used for TRSE and EN-CODE. Note, λ_{null}=10ms was not achievable for TRSE with this protocol due to timing constraints imposed by this particular T_ε. EN-CODE waveforms were calculated offline as described above and then implemented on the scanner.

Eddy current induced image distortions were evaluated for each diffusion encoding waveform by measuring the pixel-wise coefficient of variation (CoV) across the three acquired directions. The mean global CoV (CoV_{Global}) was then calculated within all water voxels (masked to exclude the very low Fomblin signal in the b=0 images) as well in edge voxels (CoV_{Edge}) at water-Fomblin interfaces. Masking was performed using magnitude thresholding and built-in binary image operations in Matlab.

The optimal λ_{null} were determined for EN-CODE and TRSE by comparing the mean CoV_{Edge} from the acquisitions with each of the ten λ_{null} values. The λ_{null} that led to the minimum CoV_{Edge} was then used for *in vivo* imaging.

Apparent diffusion coefficient (ADC) maps were also reconstructed from each DWI set and mean global ADC values were measured within all water voxels.

	FOV (mm)	Resolution (mm)	b (s/mm^2)	TR (ms)	TE (ms)	Other
MONO	300x300	1.7x1.7x5.0	1000	2300	80	2x GRAPPA 5 Averages 15 Slices BW=1852Hz/px
CODE					71	
TRSE					96	
EN-CODE					76-78	

Table 7.1: DWI/DTI protocol details for both phantom and in vivo imaging.

7.4.3 In Vivo Imaging

Neuro DTI were acquired in healthy volunteers (N=10) to further compare the four diffusion encoding protocols. Four DTI sets were acquired: 1) MONO; 2) CODE; 3) TRSE with λ_{null}=80ms; and 4) EN-CODE with λ_{null}=80ms. A λ_{null} of 80ms was chosen for TRSE and EN-CODE based on the phantom results (see below). The *in vivo* protocol was identical to the

phantom study, but with 20 diffusion encoding gradient directions to facilitate tensor reconstruction (Table 7.1).

Images were reconstructed using the manufacturer provided pipeline and no additional image registration or distortion correction was performed to correct for eddy current induced image distortion prior to off-line tensor reconstruction from each DTI set. Fractional Anisotropy (FA) maps were then generated off-line from the diffusion tensors. The mean whole-brain global FA (FA_{Global}) was measured for each diffusion encoding protocol within a manually drawn whole brain mask on the b=0 images and in the outermost single-pixel layer from the global mask (FA_{Edge}). To visualize differences in eddy current induced image distortion, FA-weighted color maps of the diffusion tensor primary eigenvector (red, green and blue mapped to x, y and z) were generated for each subject [150].

All values are reported as Mean±1SD and comparisons were made using paired t-tests wherein p-values <0.05 were deemed statistically significant.

7.5 Results

7.5.1 Simulations

Figure 7.2 shows EN-CODE gradient waveforms generated for a range of λ_{null} values and the corresponding eddy current spectra, normalized to the largest peak. Each EN-CODE gradient waveform nulled eddy currents for each specified λ_{null}.

Pulse sequence diagrams for MONO, CODE, TRSE with λ_{null}=80ms and EN-CODE with λ_{null}=80ms are shown in Figure 7.3. Each was used for both phantom and in vivo imaging. TRSE had the longest TE (96ms), which was reduced to 80ms with MONO, further reduced to

78ms with EN-CODE, and minimized to 71ms with CODE. The eddy current spectra for each sequence are shown in Figure 7.4. MONO demonstrated the largest residual eddy currents across all time constants (λ) whereas CODE notably reduced eddy currents at all λ while minimizing TE compared to the other three methods. TRSE and EN-CODE demonstrated even greater eddy current reductions, particularly for λ>20ms.

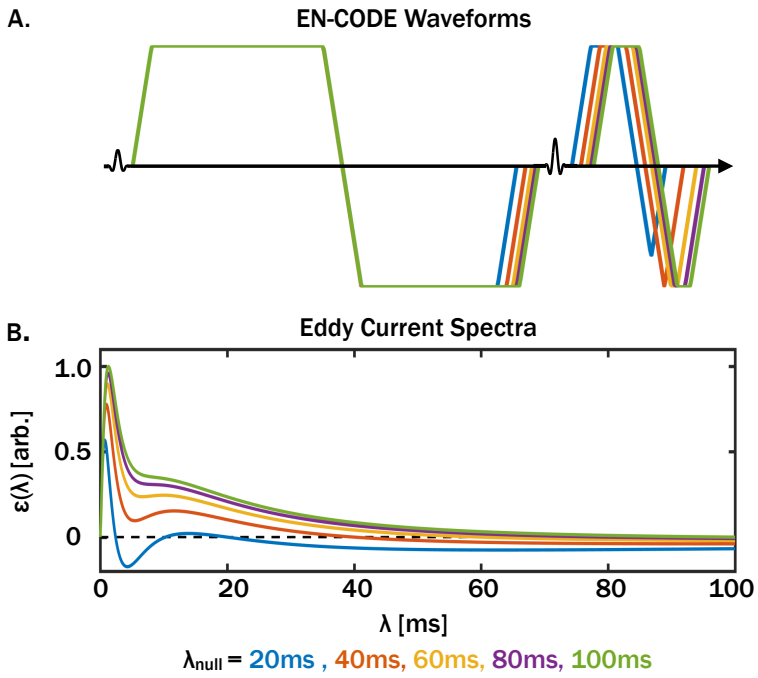

Figure 7.2: (A) EN-CODE diffusion encoding gradient waveforms designed for λ_{NULL} = 20ms, 40ms, 60ms, 80ms and 100ms. While EN-CODE does not impose any specific gradient shape, the resultant waveforms contain only trapezoidal and triangular pulses. (B) The resultant eddy current spectra for each of the waveforms shown in (A). Each waveform nulls eddy currents with $\lambda=\lambda_{null}$. λnull=80ms empirically produced the smallest eddy current induced image distortion on our system and was used for all in vivo imaging. Note that while the location of the refocusing RF pulse varies slightly between waveforms in (A), the position shown is approximated to improve visibility.

The minimum TE for TRSE (λ_{null}=80ms), EN-CODE (λ_{null}=80ms) and MONO over a range of b-values and T_ε, as well as TE differences between sequences are shown in Figure

7.5. EN-CODE had a shorter TE than TRSE for 78% of the examined cases (TE_{TRSE}-$TE_{EN\text{-}CODE}$=20.8±18.8ms) and a shorter TE than MONO in 65% of cases (TE_{MONO}-$TE_{EN\text{-}CODE}$=3.1±12.7ms) while conferring eddy current insensitivity. EN-CODE had a longer TE than MONO for short EPI readouts (T_ε<25ms) at b-values above 500s/mm^2 and a longer TE than TRSE for short EPI readouts (T_ε<30ms) at all b-values. For T_ε≥30ms, EN-CODE had a shorter TE than MONO and TRSE for all b-values. The choice of λ_{null} had only a small impact on the TE for EN-CODE (the maximum TE difference between λ_{null} values was 2ms) and had no impact on TE for TRSE.

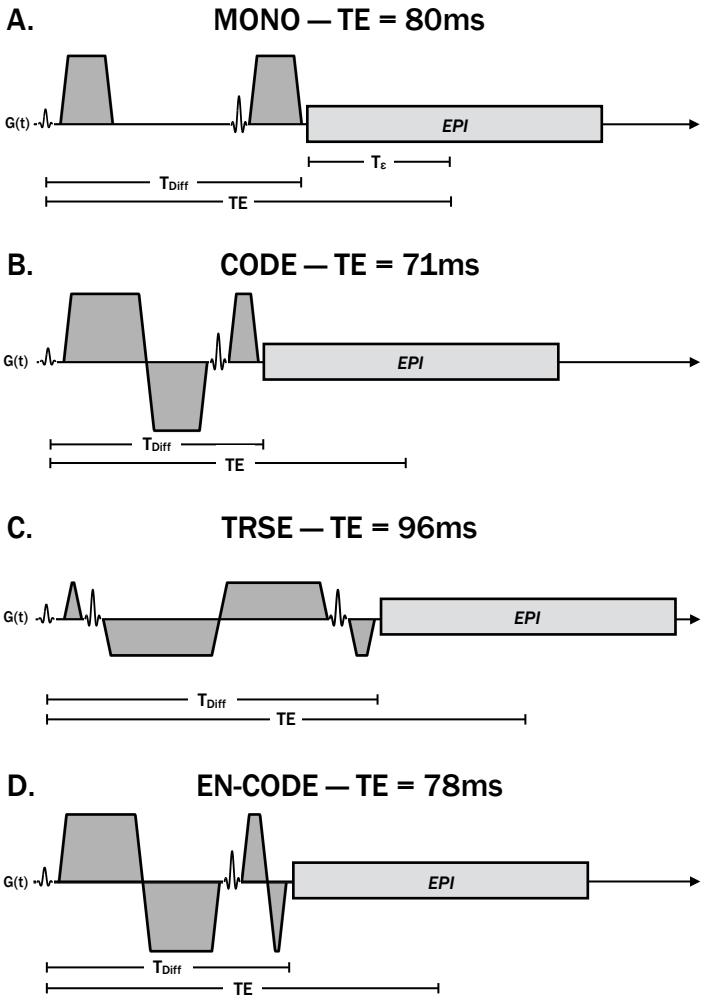

Figure 7.3: Pulse sequence diagrams for b=1000s/mm^2 with (A) MONO, (B) CODE, (C) TRSE and (D) EN-CODE diffusion encoding. The EPI time-to-echo,

T_ε, was 27.5ms, which accords with 1.7mm in-plane spatial resolution (FOV=300x300mm) for all four sequences. MONO and CODE are both susceptible to eddy current distortions, whereas TRSE and EN-CODE are eddy current compensated. EN-CODE accomplishes eddy current nulling with a slight TE decrease compared to MONO, whereas TRSE requires a significant TE increase compared with MONO.

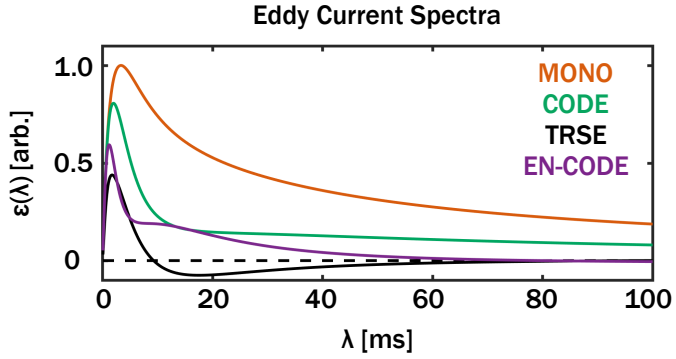

Figure 7.4: Simulated eddy current spectra at the end of diffusion encoding (T_{Diff}) for a range of eddy current decay time constants (λ) for each sequence shown in Figure 3. Spectra are normalized by the peak of the MONO spectrum. MONO generates the largest residual eddy currents for all values of λ. CODE notably reduces eddy currents while minimizing TE whereas TRSE and EN-CODE lead to large reductions for λ greater than 20ms and an eddy current null point at the prescribed λ_{null}=80ms.

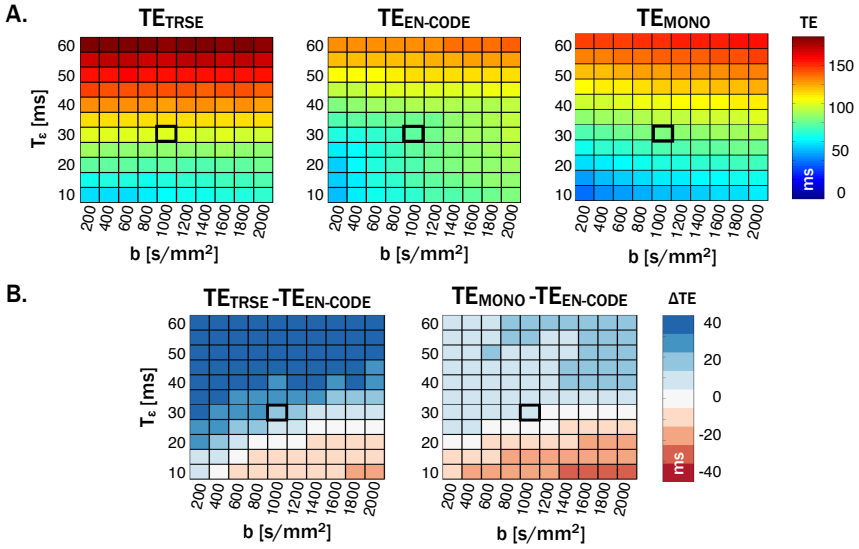

Figure 7.5: (A) The minimum TE as a function of b-value and EPI time-to-echo, T_ε for TRSE, EN-CODE and MONO diffusion encoding. (B) TE differences between TRSE and EN-CODE (left) as well as between MONO and EN-CODE (right). Positive values (blue) indicate EN-CODE has a shorter TE while negative values (red) indicate EN-CODE has a longer TE. EN-CODE had shorter TEs than TRSE in 78% of instances and shorter TEs than MONO in 65% of instances. The black square indicates the parameters used for phantom and in vivo imaging in this study and plotted in Figure 7.3. The upper row (T_ε=60ms) corresponds to a DTI protocol with ~0.5mm in-plane spatial resolution with a full-Fourier readout, the lower row (T_ε=10ms) corresponds to ~3.0mm resolution.

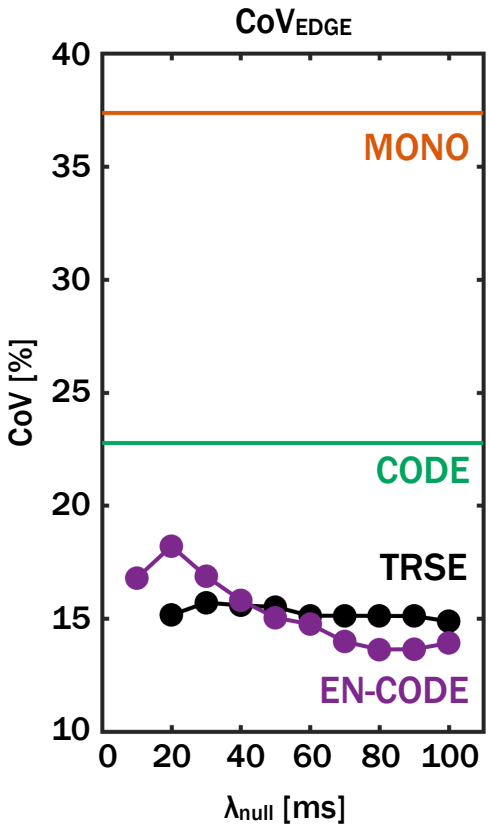

Figure 7.6: DTI distortion, quantified by the mean coefficient of variation across diffusion encoding directions within phantom edges (CoV_{Edge}) for each of the pulse sequences examined. Image reconstruction was performed using only the vendor provided pipeline and no eddy current image distortion correction was performed. MONO was the worst (CoV_{Edge}=37.4±25.8) while CODE performed slightly better (CoV_{Edge}=22.8±18.0). For MONO and CODE, these results are

independent of λ_{null}. TRSE and EN-CODE substantially reduced image distortion for all choices of λ_{null}. CoV_{Edge} was minimized for EN-CODE with λ_{null}=80ms (CoV_{Edge}=13.6±11.6), which was used for subsequent in vivo imaging. The choice of λ_{null} had little effect on distortion for TRSE so λ_{null}=80ms (CoV_{Edge}=15.1±11.6) was also used for TRSE in vivo.

7.5.2 Phantom Imaging

CoV_{Edge} was plotted for for MONO and CODE and for TRSE and EN-CODE as a function of λ_{null} (Figure 7.6). CoV_{Edge} was greatest for MONO (CoV_{Edge}=37.4±25.8%) and reduced by 39% with CODE (CoV_{Edge}=22.8±18.0%). The minimum CoV_{Edge} for EN-CODE was achieved with λ_{null}=80ms (CoV_{Edge}=13.6±11.6%), which reduced CoV_{Edge} by 64% compared with MONO, and was used for subsequent *in vivo* imaging. TRSE demonstrated minimal variation with the choice of λ_{null} (CoV_{Edge} differences were ≤0.9% between λ_{null} values), so λ_{null}=80ms was also used for TRSE in vivo (CoV_{Edge}=15.1±11.6%).

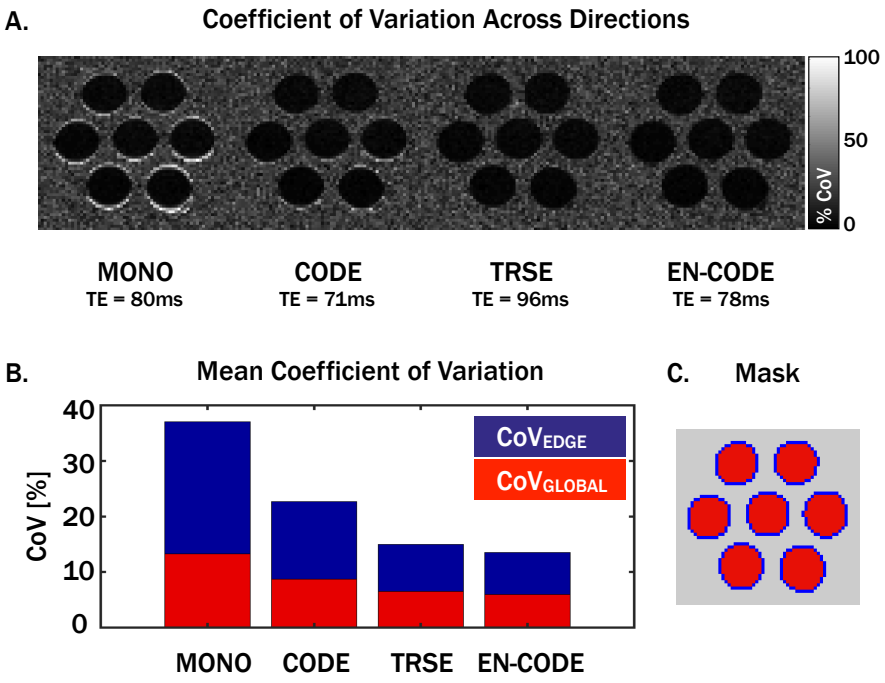

Figure 7.7: (A) Coefficient of variation (CoV) maps calculated across all diffusion encoding directions for each technique as well as (B) mean CoV values within all

cylinders, CoV_{Global} (red) and within edge voxels only, CoV_{Edge} (blue). High CoV indicates large differences in signal intensity between diffusion directions which is indicative of eddy current induced image distortions. CoV was largest with the MONO sequence, reduced with CODE, and further reduced with TRSE and EN-CODE, especially for edge voxels. (C) The segmentation used for global analysis.

CoV maps for MONO, CODE, TRSE (λ_{null}=80ms) and EN-CODE (λ_{null}=80ms) in a single slice are shownin Figure 7.7A. The CoV was high for MONO near phantom edges (water-Fomblin interfaces) indicating eddy current induced misregistration between images with different diffusion encoding directions. This effect was mitigated with CODE and substantially reduced with TRSE and EN-CODE, as shown in the CoV_{Global} and CoV_{Edge} values plotted in Figure 7.7B.

No significant differences were observed in mean ADC values from any of the sequences. MONO ADC was 2.1±0.3mm^2/ms, CODE ADC was 2.1±0.25mm^2/ms, TRSE (λ_{null}=80ms) ADC was 2.1±0.25mm^2/ms, and EN-CODE (λ_{null}=80ms) ADC was 2.1±0.22mm^2/ms.

7.5.3 In Vivo Imaging

A representative neuro DTI example is shown in Figure 7.8. The apparent SNR of the DWI from TRSE was lower compared to the other sequences due to the longer TE (Figure 7.8A) and the second refocusing pulse. Eddy current distortion between diffusion encoding directions in MONO and CODE led to regions of notably elevated FA near brain edges (Figure 7.8B,C) that were largely eliminated with TRSE and EN-CODE.

Global FA analysis is shown in Figure 7.9. FA was reduced with CODE compared to MONO (FA_{Global}=0.24±0.01 vs. 0.25±0.01, p=0.02; FA_{Edge}=0.21±0.02 vs. 0.24±0.02, p=3x10^{-4}). FA was further reduced with EN-CODE compared to MONO (FA_{Global}=0.24±0.01 vs. 0.25±0.01,

$p=1.5x10^{-4}$; FA_{Edge}=0.16±0.01 vs. 0.24±0.02, $p<1x10^{-5}$). Similar FA reductions were observed with TRSE compared to MONO (FA_{Global}=0.23±0.01 vs.0.25±0.01, $p=1x10^{-5}$; FA_{Edge}=0.16±0.01 vs. 0.24±0.02, $p<1x10^{-5}$). There was no significant difference between TRSE and EN-CODE for either FA_{Global} or FA_{Edge}.

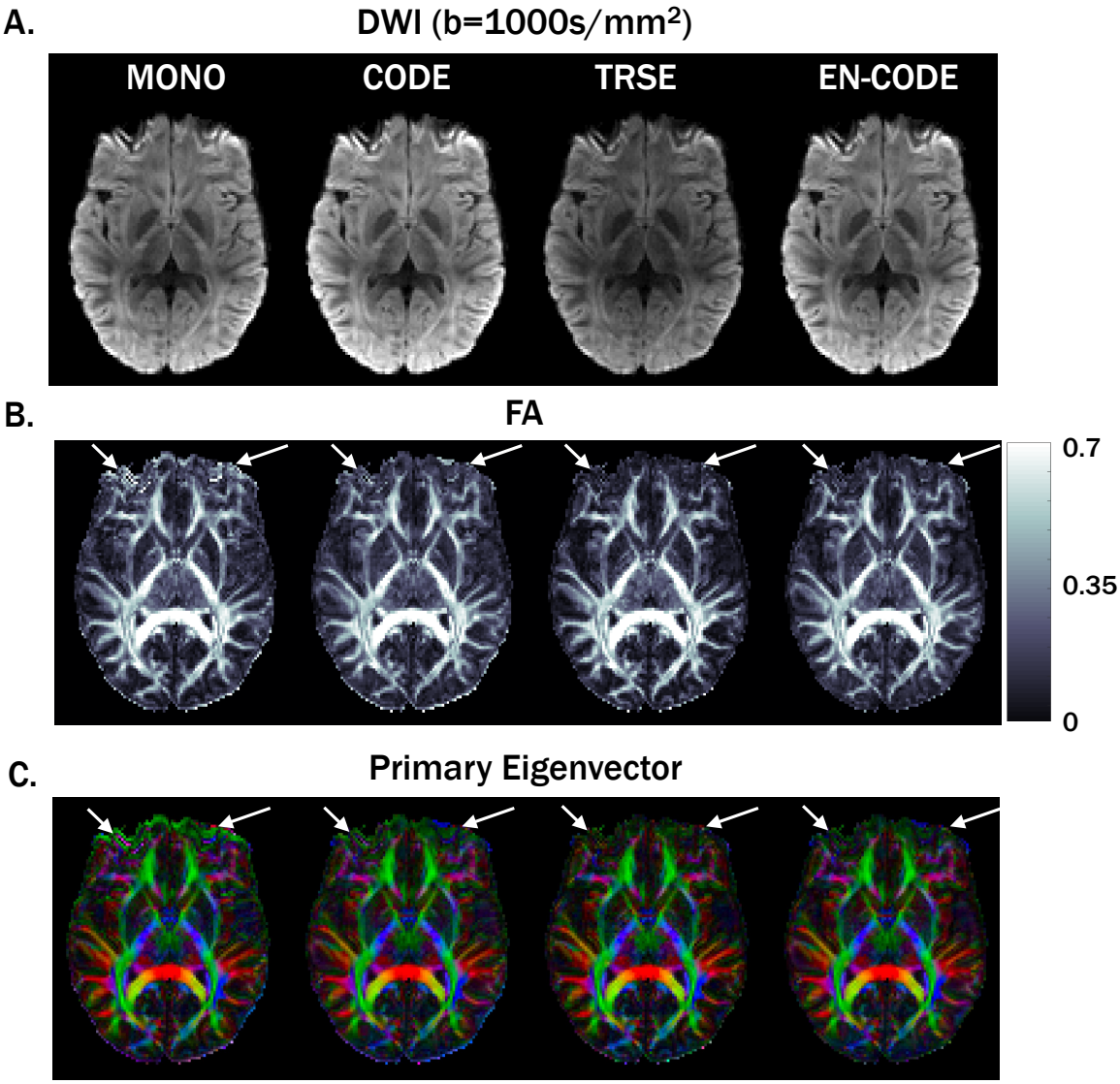

Figure 7.8: (A) Diffusion weighted images from each technique with matched window and level, (B) reconstructed FA maps and (C) FA-weighted primary eigenvector maps where the x, y, and z vector components are mapped to red, green, and blue, respectively. MONO diffusion encoding leads to substantial eddy current image distortions that led to regions of artificially high FA (white

arrows). These were reduced with CODE and further reduced with TRSE and EN-CODE. EN-CODE, however, had a shorter TE than TRSE (78ms vs. 96ms) which led to higher apparent SNR in (A).

7.6 Discussion

The results of the simulations, phantom imaging, and *in vivo* imaging all indicate that EN-CODE achieves a significant reduction of eddy current distortions compared with MONO. In simulations, EN-CODE reduced TE compared with MONO and TRSE for a wide range of imaging and diffusion weightings parameters, only failing to do so for very short (i.e. low-resolution) EPI readouts. Symmetric, full-Fourier k-space coverage was used in this work, but partial Fourier imaging can be used to substantially shorten T_ε and thereby reduce TE, particularly for TRSE and, to a lesser extent MONO, which would reduce or eliminate the TE reduction of EN-CODE. However, the use of partial Fourier leads to an increase in bulk-motion sensitivity [100], the potential for additional signal attenuation from eddy currents [151], a broader point-spread function, and lower SNR. EN-CODE can be used to shorten TE without the drawbacks of partial Fourier imaging. For the protocol used in this study (1.7mm in-plane resolution, b=1000s/mm^2) a partial Fourier factor of 6/8 (i.e. T_ε=20.6ms) results in TE=78ms for TRSE, which is equivalent to full-Fourier EN-CODE.

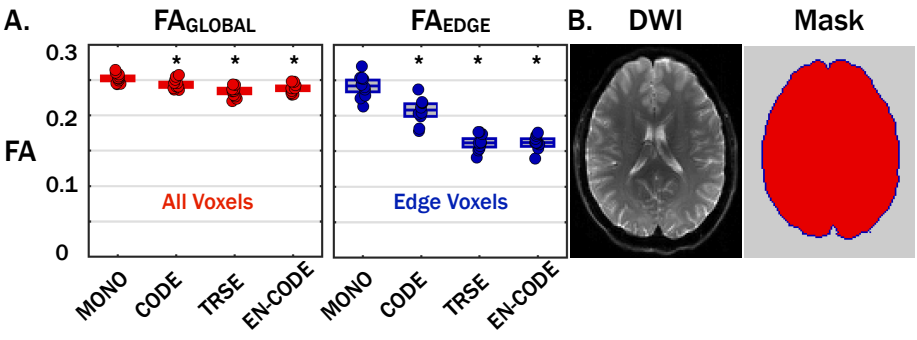

*Figure 7.9: (A) Mean global FA values measured in all brain voxels, FA_{Global} (red) and voxels along brain edges, FA_{Edge} (blue). * Indicates significant differences*

from MONO ($p<0.05$). (B) Example DWI and mask used for FA_{Global} and FA_{Edge} analysis. Notably, FA_{Edge} was highest with MONO, decreased with CODE and decreased further with both TRSE and EN-CODE. This indicates that CODE reduces eddy current distortions compared with MONO and that both TRSE and EN-CODE further reduce them. Trends were equivalent for FA_{Global} and FA_{Edge}, but changes were exaggerated in edge voxels where distortions have a larger impact on the diffusion tensor.

While EN-CODE reduced TE compared to TRSE and MONO for a wide range of acquisition parameters, it led to longer TEs for cases with high b-values and very short (i.e. low spatial resolution, partial Fourier) EPI readouts. In these cases, the temporal footprint of the readout within the TE is reduced, which improves the efficiency of non-optimized waveforms. Therefore, TRSE may be a better choice for these applications. The EN-CODE framework is compatible with a TRSE-like double echo sequence which, when combined, may also confer TE reductions. However, this has not been evaluated in the present study.

Eddy current distortions in EN-CODE were more sensitive to the choice of λ_{null} than TRSE. This may be due to the substantially lower gradient amplitudes used in TRSE than in EN-CODE (gradient amplitude was 46mT/m for TRSE vs. 76mT/m for EN-CODE). The use of two refocusing pulses in TRSE causes the minimum TE to be especially dictated by T_ε rather than b-value (as shown by the flat TRSE TE distribution in Figure 7.5), which also indicates that higher b-values could have been accomplished without increasing TE by increasing gradient amplitude. This also led to lower slew rates for TRSE (30T/m/s) because ramp times were fixed for all diffusion encoding gradients in our vendor-provided implementation of TRSE. Further optimization could have thus led to a slightly shorter TE for TRSE. However, even with the higher gradient amplitudes and higher slew rates, EN-CODE (λ_{null}=80ms) achieved equivalent eddy current nulling performance to TRSE (λ_{null}=80ms).

The relatively flat behavior of EN-CODE for $\lambda_{null} \geq 50$ms indicates that the technique is unlikely to be sensitive to slight variations in hardware between scanners or to the presence of multiple eddy current decay times. This behavior is also consistent with the smooth eddy current spectra for EN-CODE as shown in Figure 7.2. Further distortion reductions may be achievable by nulling multiple values of λ_{null} as previously shown in a double echo sequence [148] albeit with likely TE increases.

The in vivo neuro DTI results demonstrate that EN-CODE improves diffusion tensor reconstruction without the need for post-processing eddy current corrections. While numerous image processing corrections exist that improve DTI reconstruction in the presence of eddy current distortions [46, 151, 152], an eddy current nulled diffusion encoding approach avoids the added complexity and potential for errors [153] and EN-CODE achieves this with no penalty compared to MONO over a wide range of acquisition parameters.

It is possible that subject motion between diffusion encoding directions could have contributed to the observed artifacts near the edges of the brain. However, the consistency of our findings across ten subjects indicates that eddy current induced image distortions were the predominant cause of distortion in the MONO and CODE sequences.

Although it was not evaluated in this work, the tripolar approach for eddy current nulling previously described by Finsterbusch [149] also reduced TE compared with TRSE in many scenarios and used only a single refocusing pulse. EN-CODE has similar benefits to this approach, but has the added flexibility of optimally conforming to any set of sequence parameters. Furthermore, the tripolar approach uses a gap between gradient lobes to accomplish eddy current nulling, which leads to sub-optimal diffusion encoding efficiency which extends TE.

EN-CODE gradients are not symmetric about the refocusing pulse, therefore concomitant magnetic field corrections are needed to avoid significant image artifacts. A

previously described linear correction was used in this work [96, 108] and no residual effects were observed. This approach is widely used for TRSE and was also used for CODE in this work.

It is also notable that CODE, which does not explicitly account for eddy currents, improved eddy current distortions compared to MONO while substantially reducing TE. CODE has previously been shown to reduce TE compared with MONO for a wide range of b-values and EPI durations [108] indicating that the CODE gradient design is both time optimal and more robust to eddy current induced image distortion than MONO. However, both phantom and in vivo imaging showed that some residual eddy current effects were still present in CODE.

7.7 Conclusion

EN-CODE reduced eddy current induced image distortions in DTI by incorporating eddy current compensation in the previously described CODE optimization framework. EN-CODE also has a shorter TE compared to MONO and TRSE over a wide range of acquisition parameters.

7.8 Acknowledgements

The authors are grateful for research support from the Department of Radiological Sciences at UCLA and AHA 16PRE27380023 to EA.

8 APPENDIX

This appendix contains a brief, general description of mathematical optimization and convex optimization and how these concepts apply to the diffusion encoding gradient optimizations described in Chapters 4 and 7.

8.1 Optimization

Broadly speaking, optimization refers to the process of finding the input value that minimizes or maximizes a particular function. For the case of a minimization of some function f(x), this can be represented by:

$$x = \underset{x}{\operatorname{argmin}}\ f(x) \tag{8.1}$$

Here, x represents the input value to f that produces the minimum output value, f(x). There are many ways that this class of problem can be solved and these specifics are outside of the scope of this dissertation.

8.2 Convex Optimization

The strategy for solving an optimization problem and the speed with which it can be solved is highly dependent on the characteristics of the function, f to be maximized or minimized. One important characteristic for the purposes of optimization is *convexity*. A convex function has features that are particularly useful in optimization and is generally defined by the following criterion:

$$\mathbf{f(\theta x_1 + (1-\theta)x_2) < \theta f(x_1) + (1-\theta) f(x_2)} \qquad \mathbf{8.2}$$

Where 0 < θ < 1. In a one-dimensional case, this can be understood as the case where a ray connecting any two points on a curve, $f(x_1)$ and $f(x_2)$, is entirely above the function f(x) for $x_1<x<x_2$ and is illustrated in Figure 8.1.

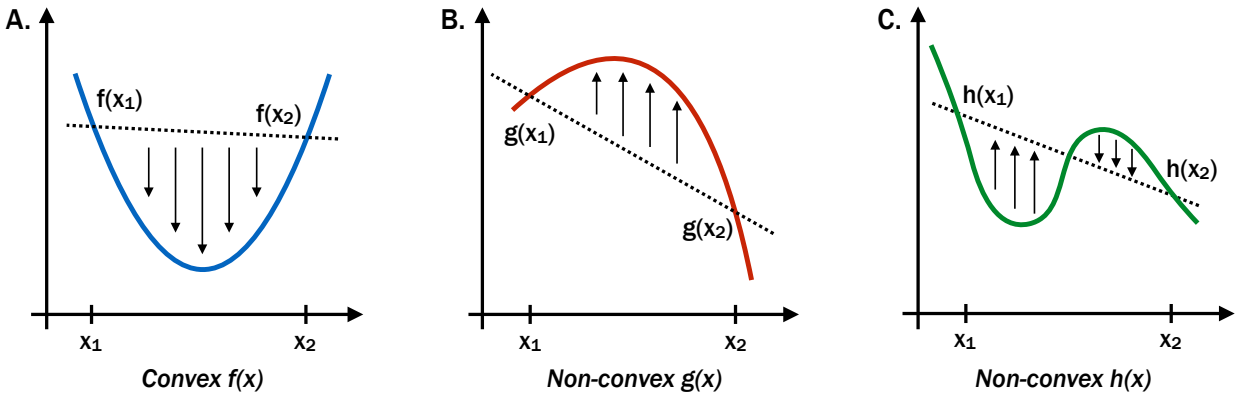

Figure 8.1: Examples of a convex function (A) and non-convex functions (B and C). In one-dimension, convexity requires that a line connecting two points on the curve must exist entirely above the curve itself.

While not all optimizations present themselves immediately as convex optimization problems, it is useful to formulate them as such when possible (as in the case described in Chapter 4). While solutions can be reached for non-convex problems, many proven methods exist for solving convex optimization problems extremely efficiently and reliably. For this reason,

convex optimization has found many applications in situations where the fast, robust convergence to a solution is of great importance.

8.3 Convex Gradient Optimization

In the context of MRI gradient waveform design, an optimization problem can be defined wherein the gradient waveform, G(t), serves as an input value to some function of interest, f(G) with a desired output parameter, y: y = f(G). To design a gradient waveform with this property, the optimization can be formulated as:

$$G(t) = \underset{G}{\operatorname{argmin}}\ f(G) - y \tag{8.3}$$

Note that in this case the input G(t) is not a scalar value, but a function defined discretely over time. Alternatively, we may wish to simply minimize or maximize the output f(G). These problems can be formulated as follows:

$$G(t) = \underset{G}{\operatorname{argmin}}\ f(G) \tag{8.4}$$

$$G(t) = \underset{G}{\operatorname{argmax}}\ f(G) \tag{8.5}$$

The function, f and output, y can be chosen to specify the desired properties of the gradient pulse. For example, in the case of diffusion encoding gradient waveform design, one may wish to determine the waveform that maximizes the diffusion encoding strength (b-value, Equation **4.9**):

$$G(t) = \underset{G}{\operatorname{argmax}}\ b(G) \tag{8.6}$$

The b-value function is *convex* with respect to G(t). However, the minimum of b=0 simply corresponds with the trivial case of G(t)=0 for all t. It is challenging to determine a maximum of the b-value function because of its degenerate nature. This degeneracy arises because multiple

distinct G(t) inputs can produce the same b-value. For example, flipping the polarity of any gradient waveform ahs no impact on its b-value.

While it is difficult to conceptualize the “shape” of the b-value function over the full space of gradient waveform possibilities, it can be easily visualized for a case with only one degree of freedom. Consider a gradient waveform consisting of only two rectangular pulses with fixed duration and spacing, but with amplitudes G_1 and G_2 free to vary between +80mT/m and -80mT/m (Figure 8.2A). To ensure zero total gradient area, G_2 must be equal to $-G_1$. Thus, the full space of possible waveforms can be described by only G_1. If b-value is plotted as a function of G_1 (Figure 8.2B), we can see that it is quadratic and possesses two equivalent maxima at +80mT/m and -80mT/m.

If we instead define the function β (Equation **4.11**), which has a single common maximum with b-value and varies linearly with G_1 instead of quadratically (Figure 8.2C) we can separate each waveform from its negative counterpart. As a result, β has a unique maximum that can be easily and efficiently determined using convex optimization with the following objective function:

$$G(t) = \underset{G}{\operatorname{argmax}}\ \beta(G) \tag{8.7}$$

This objective function can be used to determine the G(t) that occupies the global maximum of β. Because this maximum corresponds with one of the degenerate b-value maxima, it still solves the desired problem. Note that if the objective were reformulated to minimize β, the optimization would converge to the inverse of G(t) as determined by the maximization problem. and the same problem would effectively be solved.

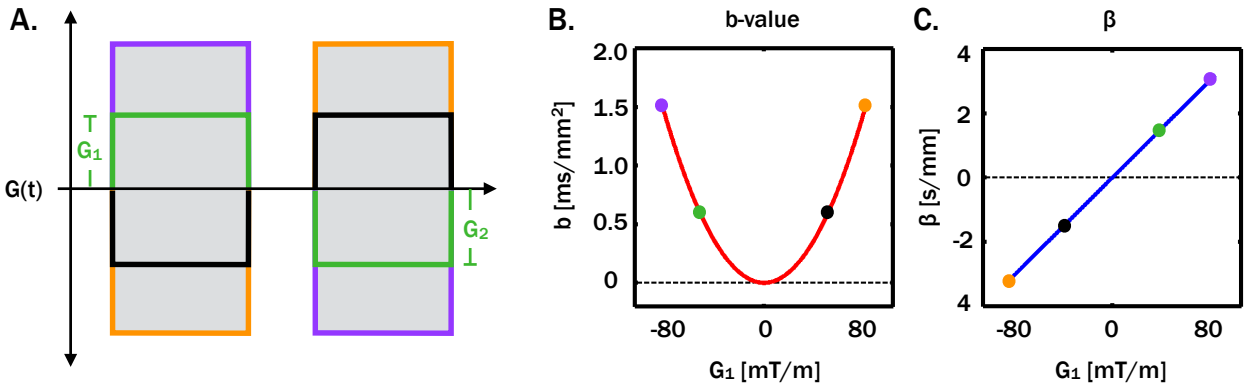

Figure 8.2: Diffusion encoding gradient waveforms (A) with fixed durations and variable gradient amplitudes G_1 and G_2. While the b-value (B) of any waveform and its inverse (i.e. purple vs. orange) are equivalent, β has a unique value for each waveform (C), which facilitates the use of convex optimization.

9 REFERENCES

1. Stejskal EO, Tanner EO. Spin Diffusion measurements: Spin Echoes in the Presence of a Time Dependent Field Gradient. The Journal of Chemical Physics. 1964.

2. Taylor DG, Bushell MC. The spatial mapping of translational diffusion coefficients by the NMR imaging technique. Phys Med Biol. 1985;30(4):345-9.

3. Moseley ME, Kucharczyk J, Mintorovitch J, Cohen Y, Kurhanewicz J, Derugin N, Asgari H, Norman D. Diffusion-weighted MR imaging of acute stroke: correlation with T2-weighted and magnetic susceptibility-enhanced MR imaging in cats. AJNR Am J Neuroradiol. 1990;11(3):423-9.

4. Lyng H, Haraldseth O, Rofstad EK. Measurement of cell density and necrotic fraction in human melanoma xenografts by diffusion weighted magnetic resonance imaging. Magn Reson Med. 2000;43(6):828-36.

5. McNab JA, Edlow BL, Witzel T, et al. The Human Connectome Project and beyond: initial applications of 300 mT/m gradients. Neuroimage. 2013;80:234-45.

6. Wu MT, Su MY, Huang YL, Chiou KR, Yang P, Pan HB, Reese TG, Wedeen VJ, Tseng WY. Sequential changes of myocardial microstructure in patients postmyocardial infarction by diffusion-tensor cardiac MR: correlation with left ventricular structure and function. Circ Cardiovasc Imaging. 2009;2(1):32-40, 6 p following

7. Pop M, Ghugre NR, Ramanan V, Morikawa L, Stanisz G, Dick AJ, Wright GA. Quantification of fibrosis in infarcted swine hearts by ex vivo late gadolinium-enhancement and diffusion-weighted MRI methods. Phys Med Biol. 2013;58(15):5009-28.

8. Nguyen C, Fan Z, Xie Y, Dawkins J, Tseliou E, Bi X, Sharif B, Dharmakumar R, Marban E, Li D. In vivo contrast free chronic myocardial infarction characterization using diffusion-weighted cardiovascular magnetic resonance. J Cardiovasc Magn Reson. 2014;16:68.

9. Sarnak MJ, Levey AS, Schoolwerth AC, et al. Kidney disease as a risk factor for development of cardiovascular disease: a statement from the American Heart Association Councils on Kidney in Cardiovascular Disease, High Blood Pressure Research, Clinical Cardiology, and Epidemiology and Prevention. Hypertension. 2003;42(5):1050-65.

10. Fox CS, Muntner P, Chen AY, et al. Use of evidence-based therapies in short-term outcomes of ST-segment elevation myocardial infarction and non-ST-segment elevation

myocardial infarction in patients with chronic kidney disease: a report from the National Cardiovascular Data Acute Coronary Treatment and Intervention Outcomes Network registry. Circulation. 2010;121(3):357-65.

11. Gansevoort RT, Correa-Rotter R, Hemmelgarn BR, Jafar TH, Heerspink HJ, Mann JF, Matsushita K, Wen CP. Chronic kidney disease and cardiovascular risk: epidemiology, mechanisms, and prevention. Lancet. 2013;382(9889):339-52.

12. Pinto de Carvalho L, McCullough PA, Gao F, Sim LL, Tan HC, Foo D, Ooi YW, Richards AM, Chan MY, Yeo TC. Renal function and anaemia in acute myocardial infarction. Int J Cardiol. 2013;168(2):1397-401.

13. Saran R, Li Y, Robinson B, et al. US Renal Data System 2014 Annual Data Report: Epidemiology of Kidney Disease in the United States. Am J Kidney Dis. 2015;65(6 Suppl 1):A7.

14. Ferreira PF, Kilner PJ, McGill LA, et al. In vivo cardiovascular magnetic resonance diffusion tensor imaging shows evidence of abnormal myocardial laminar orientations and mobility in hypertrophic cardiomyopathy. J Cardiovasc Magn Reson. 2014;16:87.

15. von Deuster C, Sammut E, Asner L, Nordsletten D, Lamata P, Stoeck CT, Kozerke S, Razavi R. Studying Dynamic Myofiber Aggregate Reorientation in Dilated Cardiomyopathy Using In Vivo Magnetic Resonance Diffusion Tensor Imaging. Circ Cardiovasc Imaging. 2016;9(10).

16. Nielles-Vallespin S, Khalique Z, Ferreira PF, et al. Assessment of Myocardial Microstructural Dynamics by In Vivo Diffusion Tensor Cardiac Magnetic Resonance. J Am Coll Cardiol. 2017;69(6):661-76.

17. Nguyen C, Fan Z, Sharif B, He Y, Dharmakumar R, Berman DS, Li D. In vivo three-dimensional high resolution cardiac diffusion-weighted MRI: A motion compensated diffusion-prepared balanced steady-state free precession approach. Magn Reson Med. 2013.

18. Stoeck CT, von Deuster C, Genet M, Atkinson D, Kozerke S. Second-order motion-compensated spin echo diffusion tensor imaging of the human heart. Magn Reson Med. 2015.

19. Welsh C, Di Bella E, Hsu E. Higher-Order Motion-Compensation for In Vivo Cardiac Diffusion Tensor Imaging in Rats. IEEE Trans Med Imaging. 2015.

20. Aliotta E, Wu HH, Ennis DB. Convex Optimized Diffusion Encoding (CODE) Gradient Waveforms for Minimum Echo Time and Bulk Motion Compensated Diffusion Weighted MRI. Magnetic Resonance in Medicine. 2017;77(2):717-29.

21. Lauterbur PC. Image formation by induced local interactions. Examples employing nuclear magnetic resonance. 1973. Clin Orthop Relat Res. 1989(244):3-6.

22. Damadian R, Goldsmith M, Minkoff L. NMR in cancer: XVI. FONAR image of the live human body. Physiol Chem Phys. 1977;9(1):97-100, 8.

23. Zeeman P. On the Influence of Magnetism on the Nature of the Light Emitted by a Substance. The Astrophysical Journal. 1897;5:332.

24. Planck M. Ueber das Gesetz der Energieverteilung im Normalspectrum. Annalen der Physik. 1901;309(3):553-63.

25. Davidson N. Statistical Mechanics: Dover Publications; 2013.

26. Bernstein MA, King KF, Zhou ZJ. Handbook of MRI pulse sequences. Amsterdam ; Boston: Academic Press; 2004. xxii,1017 p. p.

27. Griffiths DJ. Introduction to Quantum Mechanics: Pearson Prentice Hall; 2005.

28. Carr HY. Steady-State Free Precession in Nuclear Magnetic Resonance. Physical Review. 1958;112(5):1693-701.

29. Haase A, Frahm J, Matthaei D, Hanicke W, Merboldt KD. FLASH imaging. Rapid NMR imaging using low flip-angle pulses. Journal of Magnetic Resonance (1969). 1986;67(2):258-66.

30. von Knobelsdorff-Brenkenhoff F, Prothmann M, Dieringer MA, Wassmuth R, Greiser A, Schwenke C, Niendorf T, Schulz-Menger J. Myocardial T1 and T2 mapping at 3 T: reference values, influencing factors and implications. J Cardiovasc Magn Reson. 2013;15:53.

31. Stanisz GJ, Odrobina EE, Pun J, Escaravage M, Graham SJ, Bronskill MJ, Henkelman RM. T1, T2 relaxation and magnetization transfer in tissue at 3T. Magn Reson Med. 2005;54(3):507-12.

32. Giri S, Chung YC, Merchant A, Mihai G, Rajagopalan S, Raman SV, Simonetti OP. T2 quantification for improved detection of myocardial edema. J Cardiovasc Magn Reson. 2009;11:56.

33. Mansfield P. Multi-planar image formation using NMR spin echoes. Journal of Physics C: Solid State Physics. 1977;10(3):L55.

34. Feinberg DA, Hale JD, Watts JC, Kaufman L, Mark A. Halving MR imaging time by conjugation: demonstration at 3.5 kG. Radiology. 1986;161(2):527-31.

35. Griswold MA, Jakob PM, Heidemann RM, Nittka M, Jellus V, Wang J, Kiefer B, Haase A. Generalized autocalibrating partially parallel acquisitions (GRAPPA). Magn Reson Med. 2002;47(6):1202-10.

36. Brown R. XXVII. A brief account of microscopical observations made in the months of June, July and August 1827, on the particles contained in the pollen of plants; and on the general existence of active molecules in organic and inorganic bodies. Philosophical Magazine Series 2. 1828;4(21):161-73.

37. Einstein A. INVESTIGATIONS ON THE THEORY OF THE BROWNIAN MOVEMENT. Ann der Physik. 1905.

38. Kingsley PB. Introduction to diffusion tensor imaging mathematics: Part II. Anisotropy, diffusion-weighting factors, and gradient encoding schemes. Concepts in Magnetic Resonance Part A. 2006;28A(2):123-54.

39. Jones DK, Horsfield MA, Simmons A. Optimal strategies for measuring diffusion in anisotropic systems by magnetic resonance imaging. Magn Reson Med. 1999;42(3):515-25.

40. Seehaus A, Roebroeck A, Bastiani M, Fonseca L, Bratzke H, Lori N, Vilanova A, Goebel R, Galuske R. Histological validation of high-resolution DTI in human post mortem tissue. Frontiers in Neuroanatomy. 2015;9:98.

41. Scollan DF, Holmes A, Winslow R, Forder J. Histological validation of myocardial microstructure obtained from diffusion tensor magnetic resonance imaging. Am J Physiol. 1998;275(6 Pt 2):H2308-18.

42. Hsu EW, Muzikant AL, Matulevicius SA, Penland RC, Henriquez CS. Magnetic resonance myocardial fiber-orientation mapping with direct histological correlation. Am J Physiol. 1998;274(5 Pt 2):H1627-34.

43. Wedeen VJ, Hagmann P, Tseng WY, Reese TG, Weisskoff RM. Mapping complex tissue architecture with diffusion spectrum magnetic resonance imaging. Magn Reson Med. 2005;54(6):1377-86.

44. Tuch DS. Q-ball imaging. Magn Reson Med. 2004;52(6):1358-72.

45. Yeh FC, Wedeen VJ, Tseng WY. Generalized q-sampling imaging. IEEE Trans Med Imaging. 2010;29(9):1626-35.

46. Rohde GK, Barnett AS, Basser PJ, Marenco S, Pierpaoli C. Comprehensive approach for correction of motion and distortion in diffusion-weighted MRI. Magn Reson Med. 2004;51(1):103-14.

47. Streeter DD, Jr., Spotnitz HM, Patel DP, Ross J, Jr., Sonnenblick EH. Fiber orientation in the canine left ventricle during diastole and systole. Circ Res. 1969;24(3):339-47.

48. Axel L, Wedeen VJ, Ennis DB. Probing dynamic myocardial microstructure with cardiac magnetic resonance diffusion tensor imaging. Journal of Cardiovascular Magnetic Resonance. 2014;16(1):89.

49. Kung GL, Nguyen TC, Itoh A, Skare S, Ingels NB, Jr., Miller DC, Ennis DB. The presence of two local myocardial sheet populations confirmed by diffusion tensor MRI and histological validation. J Magn Reson Imaging. 2011;34(5):1080-91.

50. LeGrice IJ, Takayama Y, Covell JW. Transverse Shear Along Myocardial Cleavage Planes Provides a Mechanism for Normal Systolic Wall Thickening. Circ Res. 1995;77(1):182-93.

51. Roger VL. Epidemiology of myocardial infarction. Med Clin North Am. 2007;91(4):537-52; ix.

52. Roger VL. Epidemiology of Heart Failure. Circ Res. 2013;113(6):646-59.

53. Wohlgelernter D Fau - Cleman M, Cleman M Fau - Highman HA, Highman Ha Fau - Fetterman RC, Fetterman Rc Fau - Duncan JS, Duncan Js Fau - Zaret BL, Zaret Bl Fau - Jaffe CC, Jaffe CC. Regional myocardial dysfunction during coronary angioplasty: evaluation by two-dimensional echocardiography and 12 lead electrocardiography. (0735-1097 (Print)).

54. Anagnostopoulos C, Gunning MG, Pennell DJ, Laney R, Proukakis H, Underwood SR. Regional myocardial motion and thickening assessed at rest by ECG-gated99mTc-MIBI emission tomography and by magnetic resonance imaging. European Journal of Nuclear Medicine. 1996;23(8):909-16.

55. Kim RJ, Wu E, Rafael A, Chen EL, Parker MA, Simonetti O, Klocke FJ, Bonow RO, Judd RM. The use of contrast-enhanced magnetic resonance imaging to identify reversible myocardial dysfunction. N Engl J Med. 2000;343(20):1445-53.

56. Perazella MA, Rodby RA. Gadolinium-induced nephrogenic systemic fibrosis in patients with kidney disease. Am J Med. 2007;120(7):561-2.

57. Moulin K, Croisille P, Feiweier T, Delattre BM, Wei H, Robert B, Beuf O, Viallon M. In vivo free-breathing DTI and IVIM of the whole human heart using a real-time slice-followed SE-EPI navigator-based sequence: A reproducibility study in healthy volunteers. Magn Reson Med. 2015.

58. Mekkaoui C, Reese TG, Jackowski MP, Cauley SF, Setsompop K, Bhat H, Sosnovik DE. Diffusion Tractography of the Entire Left Ventricle by Using Free-breathing Accelerated Simultaneous Multisection Imaging. Radiology. 2017;282(3):850-6.

59. Rapacchi S, Wen H, Viallon M, Grenier D, Kellman P, Croisille P, Pai VM. Low b-value diffusion-weighted cardiac magnetic resonance imaging: initial results in humans using an optimal time-window imaging approach. Invest Radiol. 2011;46(12):751-8.

60. Pai VM, Rapacchi S, Kellman P, Croisille P, Wen H. PCATMIP: enhancing signal intensity in diffusion-weighted magnetic resonance imaging. Magn Reson Med. 2011;65(6):1611-9.

61. Aliotta E, Rapacchi S, Hu P, Ennis D, editors. In Vivo Spin Echo EPI Cardiac Diffusion Tensor MRI Using Ultrahigh Gradient Amplitudes. ISMRM; 2015; Toronto, ON, CA.

62. Dou J, Reese TG, Tseng WY, Wedeen VJ. Cardiac diffusion MRI without motion effects. Magn Reson Med. 2002;48(1):105-14.

63. Sosnovik DE, Wang R, Dai G, Reese TG, Wedeen VJ. Diffusion MR tractography of the heart. J Cardiovasc Magn Reson. 2009;11:47.

64. Nielles-Vallespin S, Mekkaoui C, Gatehouse P, et al. In vivo diffusion tensor MRI of the human heart: reproducibility of breath-hold and navigator-based approaches. Magn Reson Med. 2013;70(2):454-65.

65. Nguyen C, Fan Z, Sharif B, He Y, Dharmakumar R, Berman DS, Li D. In vivo three-dimensional high resolution cardiac diffusion-weighted MRI: A motion compensated diffusion-prepared balanced steady-state free precession approach. Magn Reson Med. 2013;72(5):1257-67.

66. Nguyen C, Fan Z, Xie Y, Pang J, Speier P, Bi X, Kobashigawa J, Li D. In vivo diffusion-tensor MRI of the human heart on a 3 tesla clinical scanner: An optimized second order (M2) motion compensated diffusion-preparation approach. Magn Reson Med. 2016.

67. Babcock EE, Brateman L, Weinreb JC, Horner SD, Nunnally RL. Edge artifacts in MR images: chemical shift effect. J Comput Assist Tomogr. 1985;9(2):252-7.

68. Rosen BR, Wedeen VJ, Brady TJ. Selective saturation NMR imaging. J Comput Assist Tomogr. 1984;8(5):813-8.

69. Hauger O, Dumont E, Chateil JF, Moinard M, Diard F. Water excitation as an alternative to fat saturation in MR imaging: preliminary results in musculoskeletal imaging. Radiology. 2002;224(3):657-63.

70. Ferreira PF, Gatehouse PD, Mohiaddin RH, Firmin DN. Cardiovascular magnetic resonance artefacts. J Cardiovasc Magn Reson. 2013;15:41.

71. Gruetter R. Automatic, localized in vivo adjustment of all first- and second-order shim coils. Magn Reson Med. 1993;29(6):804-11.

72. Finsterbusch J. High-resolution diffusion tensor imaging with inner field-of-view EPI. J Magn Reson Imaging. 2009;29(4):987-93.

73. Feinberg DA, Hoenninger JC, Crooks LE, Kaufman L, Watts JC, Arakawa M. Inner volume MR imaging: technical concepts and their application. Radiology. 1985;156(3):743-7.

74. Potet J, Rahmouni A, Mayer J, Vignaud A, Lim P, Luciani A, Dubois-Rande JL, Kobeiter H, Deux JF. Detection of myocardial edema with low-b-value diffusion-weighted echo-planar imaging sequence in patients with acute myocarditis. Radiology. 2013;269(2):362-9.

75. Naganawa S, Kawai H, Fukatsu H, Sakurai Y, Aoki I, Miura S, Mimura T, Kanazawa H, Ishigaki T. Diffusion-weighted imaging of the liver: technical challenges and prospects for the future. Magn Reson Med Sci. 2005;4(4):175-86.

76. Demir OI, Obuz F, Sagol O, Dicle O. Contribution of diffusion-weighted MRI to the differential diagnosis of hepatic masses. Diagn Interv Radiol. 2007;13(2):81-6.

77. Bruegel M, Holzapfel K, Gaa J, Woertler K, Waldt S, Kiefer B, Stemmer A, Ganter C, Rummeny EJ. Characterization of focal liver lesions by ADC measurements using a respiratory triggered diffusion-weighted single-shot echo-planar MR imaging technique. Eur Radiol. 2008;18(3):477-85.

78. Gourtsoyianni S, Papanikolaou N, Yarmenitis S, Maris T, Karantanas A, Gourtsoyiannis N. Respiratory gated diffusion-weighted imaging of the liver: value of apparent diffusion coefficient measurements in the differentiation between most commonly encountered benign and malignant focal liver lesions. Eur Radiol. 2008;18(3):486-92.

79. Norris DG. Implications of bulk motion for diffusion-weighted imaging experiments: effects, mechanisms, and solutions. J Magn Reson Imaging. 2001;13(4):486-95.

80. Gamper U, Boesiger P, Kozerke S. Diffusion imaging of the in vivo heart using spin echoes--considerations on bulk motion sensitivity. Magn Reson Med. 2007;57(2):331-7.

81. Kwee TC, Takahara T, Niwa T, Ivancevic MK, Herigault G, Van Cauteren M, Luijten PR. Influence of cardiac motion on diffusion-weighted magnetic resonance imaging of the liver. MAGMA. 2009;22(5):319-25.

82. Murtz P, Flacke S, Traber F, van den Brink JS, Gieseke J, Schild HH. Abdomen: diffusion-weighted MR imaging with pulse-triggered single-shot sequences. Radiology. 2002;224(1):258-64.

83. Kwee TC, Takahara T, Koh DM, Nievelstein RA, Luijten PR. Comparison and reproducibility of ADC measurements in breathhold, respiratory triggered, and free-breathing diffusion-weighted MR imaging of the liver. J Magn Reson Imaging. 2008;28(5):1141-8.

84. Chen X, Qin L, Pan D, Huang Y, Yan L, Wang G, Liu Y, Liang C, Liu Z. Liver diffusion-weighted MR imaging: reproducibility comparison of ADC measurements obtained with multiple breath-hold, free-breathing, respiratory-triggered, and navigator-triggered techniques. Radiology. 2014;271(1):113-25.

85. Edelman RR, Gaa J, Wedeen VJ, Loh E, Hare JM, Prasad P, Li W. In vivo measurement of water diffusion in the human heart. Magn Reson Med. 1994;32(3):423-8.

86. Kwee TC, Takahara T, Ochiai R, Nievelstein RA, Luijten PR. Diffusion-weighted whole-body imaging with background body signal suppression (DWIBS): features and potential applications in oncology. Eur Radiol. 2008;18(9):1937-52.

87. Ozaki M, Inoue Y, Miyati T, Hata H, Mizukami S, Komi S, Matsunaga K, Woodhams R. Motion artifact reduction of diffusion-weighted MRI of the liver: use of velocity-compensated diffusion gradients combined with tetrahedral gradients. J Magn Reson Imaging. 2013;37(1):172-8.

88. Hargreaves BA, Nishimura DG, Conolly SM. Time-optimal multidimensional gradient waveform design for rapid imaging. Magn Reson Med. 2004;51(1):81-92.

89. Middione MJ, Wu HH, Ennis DB. Convex gradient optimization for increased spatiotemporal resolution and improved accuracy in phase contrast MRI. Magn Reson Med. 2014;72(6):1552-64.

90. Gel'fand IM, Fomin SV. Calculus of variations. Rev. English ed. Englewood Cliffs, N.J.,: Prentice-Hall; 1963.

91. Lofberg J. Automatic robust convex programming. Optimization Methods & Software. 2012;27(1):115-29.

92. Zhou XJ, Du YP, Bernstein MA, Reynolds HG, Maier JK, Polzin JA. Concomitant magnetic-field-induced artifacts in axial echo planar imaging. Magn Reson Med. 1998;39(4):596-605.

93. Zhou XJ, Tan SG, Bernstein MA. Artifacts induced by concomitant magnetic field in fast spin-echo imaging. Magn Reson Med. 1998;40(4):582-91.

94. King KF, Ganin A, Zhou XJ, Bernstein MA. Concomitant gradient field effects in spiral scans. Magn Reson Med. 1999;41(1):103-12.

95. Sica CT, Meyer CH. Concomitant gradient field effects in balanced steady-state free precession. Magn Reson Med. 2007;57(4):721-30.

96. Meier C, Zwanger M, Feiweier T, Porter D. Concomitant field terms for asymmetric gradient coils: consequences for diffusion, flow, and echo-planar imaging. Magn Reson Med. 2008;60(1):128-34.

97. Baron CA, Lebel RM, Wilman AH, Beaulieu C. The effect of concomitant gradient fields on diffusion tensor imaging. Magn Reson Med. 2012;68(4):1190-201.

98. Lauenstein TC, Sharma P, Hughes T, Heberlein K, Tudorascu D, Martin DR. Evaluation of optimized inversion-recovery fat-suppression techniques for T2-weighted abdominal MR imaging. J Magn Reson Imaging. 2008;27(6):1448-54.

99. Holm S. A simple sequentially rejective multiple test procedure. Scandinavian journal of statistics. 1979:65-70.

100. Storey P, Frigo FJ, Hinks RS, Mock BJ, Collick BD, Baker N, Marmurek J, Graham SJ. Partial k-space reconstruction in single-shot diffusion-weighted echo-planar imaging. Magn Reson Med. 2007;57(3):614-9.

101. Wedeen VJ, Weisskoff RM, Poncelet BP. Mri Signal Void Due to Inplane Motion Is All-or-None. Magnetic Resonance in Medicine. 1994;32(1):116-20.

102. Gahm JK, Kindlmann G, Ennis DB. The effects of noise over the complete space of diffusion tensor shape. Med Image Anal. 2014;18(1):197-210.

103. Schulte RF, Noeske R. Peripheral nerve stimulation-optimal gradient waveform design. Magn Reson Med. 2015;74(2):518-22.

104. Aliotta E, Rapacchi S, Hu P, Ennis D, editors. Increased maximum gradient amplitude improves robustness of spin-echo cardiac diffusion-weighted MRI. SCMR; 2015; Nice, Fr.: JCMR.

105. Aliotta E, Rapacchi S, Hu P, Ennis D, editors. In Vivo Spin Echo EPI Cardiac Diffusion Tensor MRI Using Ultra-High Gradient Amplitudes. ISMRM; 2015; Toronto, ON, Canada.

106. Freidlin RZ, Kakareka JW, Pohida TJ, Komlosh ME, Basser PJ. A spin echo sequence with a single-sided bipolar diffusion gradient pulse to obtain snapshot diffusion weighted images in moving media. J Magn Reson. 2012;221:24-31.

107. Wehrli FW, Saha PK, Gomberg BR, Song HK, Snyder PJ, Benito M, Wright A, Weening R. Role of magnetic resonance for assessing structure and function of trabecular bone. Topics in Magnetic Resonance Imaging. 2002;13(5):335-55.

108. Aliotta E, Wu HH, Ennis D. Convex Optimized Diffusion Encoding (CODE) Gradient Waveforms for Minimum Echo Time and Bulk Motion Compensated Diffusion Weighted MRI. Magnetic Resonance in Medicine. 2016.

109. Higgins CB, Herfkens R, Lipton MJ, Sievers R, Sheldon P, Kaufman L, Crooks LE. Nuclear magnetic resonance imaging of acute myocardial infarction in dogs: alterations in magnetic relaxation times. Am J Cardiol. 1983;52(1):184-8.

110. Guo H, Au WY, Cheung JS, et al. Myocardial T2 quantitation in patients with iron overload at 3 Tesla. J Magn Reson Imaging. 2009;30(2):394-400.

111. Kali A, Cokic I, Kumar A, Tsaftaris S, Tang RL, Friedrich MG, Dharmakumar R. Acute reperfusion intramyocardial hemorrhage leads to regional chronic iron deposition in the heart. Journal of Cardiovascular Magnetic Resonance. 2013;15(Suppl 1):P174-P.

112. McGill LA, Scott AD, Ferreira PF, et al. Heterogeneity of Fractional Anisotropy and Mean Diffusivity Measurements by In Vivo Diffusion Tensor Imaging in Normal Human Hearts. PLoS One. 2015;10(7):e0132360.

113. Hargreaves BA. Bloch Equation Simulator 2002. Available from: http://mrsrl.stanford.edu/~brian/mritools.html.

114. Fleysher L, Fleysher R, Liu S, Zaaraoui W, Gonen O. Optimizing the precision-per-unit-time of quantitative MR metrics: examples for T1, T2, and DTI. Magn Reson Med. 2007;57(2):380-7.

115. Zhang Z, Aliotta E, Ennis D, editors. Optimized Acquisition for Joint T2 and ADC mapping in the Heart. ISMRM; 2016; Singapore, SN.

116. Nguyen C, Lu M, Fan Z, Bi X, Kellman P, Zhao S, Li D. Contrast-free detection of myocardial fibrosis in hypertrophic cardiomyopathy patients with diffusion-weighted cardiovascular magnetic resonance. J Cardiovasc Magn Reson. 2015;17(1):107.

117. Huang TY, Liu YJ, Stemmer A, Poncelet BP. T2 measurement of the human myocardium using a T2-prepared transient-state TrueFISP sequence. Magn Reson Med. 2007;57(5):960-6.

118. Salerno M, Kramer CM. Advances in parametric mapping with CMR imaging. JACC Cardiovasc Imaging. 2013;6(7):806-22.

119. Majumdar S, Orphanoudakis SC, Gmitro A, O'Donnell M, Gore JC. Errors in the measurements of T2 using multiple-echo MRI techniques. II. Effects of static field inhomogeneity. Magn Reson Med. 1986;3(4):562-74.

120. Majumdar S, Orphanoudakis SC, Gmitro A, O'Donnell M, Gore JC. Errors in the measurements of T2 using multiple-echo MRI techniques. I. Effects of radiofrequency pulse imperfections. Magn Reson Med. 1986;3(3):397-417.

121. Crawley AP, Henkelman RM. Errors in T2 estimation using multislice multiple-echo imaging. Magn Reson Med. 1987;4(1):34-47.

122. Sussman MS, Vidarsson L, Pauly JM, Cheng HL. A technique for rapid single-echo spin-echo T2 mapping. Magn Reson Med. 2010;64(2):536-45.

123. He T, Gatehouse PD, Anderson LJ, Tanner M, Keegan J, Pennell DJ, Firmin DN. Development of a novel optimized breathhold technique for myocardial T2 measurement in thalassemia. J Magn Reson Imaging. 2006;24(3):580-5.

124. Manrique A, Gerbaud E, Derumeaux G, Cribier A, Bertrand D, Lebon A, Dacher JN. Cardiac magnetic resonance demonstrates myocardial oedema in remote tissue early after reperfused myocardial infarction. Arch Cardiovasc Dis. 2009;102(8-9):633-9.

125. Kung GL, Nguyen TC, Itoh A, Skare S, Ingels NB, Miller DC, Ennis DB. The Presence of Two Local Myocardial Sheet Populations Confirmed by Diffusion Tensor MRI and Histological Validation. Journal of Magnetic Resonance Imaging. 2011;34(5):1080-91.

126. Teh I, McClymont D, Burton RA, Maguire ML, Whittington HJ, Lygate CA, Kohl P, Schneider JE. Resolving Fine Cardiac Structures in Rats with High-Resolution Diffusion Tensor Imaging. Sci Rep. 2016;6:30573.

127. Le Bihan D, Poupon C, Amadon A, Lethimonnier F. Artifacts and pitfalls in diffusion MRI. J Magn Reson Imaging. 2006;24(3):478-88.

128. Jones DK. Determining and visualizing uncertainty in estimates of fiber orientation from diffusion tensor MRI. Magn Reson Med. 2003;49(1):7-12.

129. Pajevic S, Basser PJ. Parametric and non-parametric statistical analysis of DT-MRI data. J Magn Reson. 2003;161(1):1-14.

130. Heim S, Hahn K, Samann PG, Fahrmeir L, Auer DP. Assessing DTI data quality using bootstrap analysis. Magn Reson Med. 2004;52(3):582-9.

131. Jones DK. The effect of gradient sampling schemes on measures derived from diffusion tensor MRI: a Monte Carlo study. Magn Reson Med. 2004;51(4):807-15.

132. Jones DK. Precision and accuracy in diffusion tensor magnetic resonance imaging. Top Magn Reson Imaging. 2010;21(2):87-99.

133. Olivetti G, Cigola E, Maestri R, Corradi D, Lagrasta C, Gambert SR, Anversa P. Aging, Cardiac Hypertrophy and Ischemic Cardiomyopathy Do Not Affect the Proportion of Mononucleated and Multinucleated Myocytes in the Human Heart. Journal of Molecular and Cellular Cardiology. 1996;28(7):1463-77.

134. Liewald D, Miller R, Logothetis N, Wagner HJ, Schuz A. Distribution of axon diameters in cortical white matter: an electron-microscopic study on three human brains and a macaque. Biol Cybern. 2014;108(5):541-57.

135. Aliotta E, Wu HH, Ennis DB. Convex Optimized Diffusion Encoding (CODE) Gradient Waveforms for Minimum Echo Time and Bulk Motion Compensated Diffusion Weighted MRI. Magnetic Resonance in Medicine. 2016.

136. Reese TG, Weisskoff RM, Smith RN, Rosen BR, Dinsmore RE, Wedeen VJ. Imaging myocardial fiber architecture in vivo with magnetic resonance. Magn Reson Med. 1995;34(6):786-91.

137. McGill LA, Ferreira PF, Scott AD, Nielles-Vallespin S, Giannakidis A, Kilner PJ, Gatehouse PD, de Silva R, Firmin DN, Pennell DJ. Relationship between cardiac diffusion tensor imaging parameters and anthropometrics in healthy volunteers. J Cardiovasc Magn Reson. 2016;18(1):2.

138. von Deuster C, Stoeck CT, Genet M, Atkinson D, Kozerke S. Spin echo versus stimulated echo diffusion tensor imaging of the in vivo human heart. Magn Reson Med. 2015.

139. Whitcher B, Tuch DS, Wisco JJ, Sorensen AG, Wang L. Using the wild bootstrap to quantify uncertainty in diffusion tensor imaging. Hum Brain Mapp. 2008;29(3):346-62.

140. Mansfield P, Chapman B. Active Magnetic Screening of Coils for Static and Time-Dependent Magnetic-Field Generation in Nmr Imaging. Journal of Physics E-Scientific Instruments. 1986;19(7):540-5.

141. Mansfield P, Chapman B. Active Magnetic Screening of Gradient Coils in Nmr Imaging. J Magn Reson. 1986;66(3):573-6.

142. Mansfield P, Chapman B. Multishield Active Magnetic Screening of Coil Structures in Nmr. J Magn Reson. 1987;72(2):211-23.

143. Trakic A, Liu F, Lopez HS, Wang H, Crozier S. Longitudinal gradient coil optimization in the presence of transient eddy currents. Magn Reson Med. 2007;57(6):1119-30.

144. Jensen DJ, Brey WW, Delayre JL, Narayana PA. Reduction of pulsed gradient settling time in the superconducting magnet of a magnetic resonance instrument. Med Phys. 1987;14(5):859-62.

145. Boesch C, Gruetter R, Martin E. Temporal and spatial analysis of fields generated by eddy currents in superconducting magnets: optimization of corrections and quantitative characterization of magnet/gradient systems. Magn Reson Med. 1991;20(2):268-84.

146. Koch M, Norris DG. An assessment of eddy current sensitivity and correction in single-shot diffusion-weighted imaging. Phys Med Biol. 2000;45(12):3821-32.

147. Reese TG, Heid O, Weisskoff RM, Wedeen VJ. Reduction of eddy-current-induced distortion in diffusion MRI using a twice-refocused spin echo. Magn Reson Med. 2003;49(1):177-82.

148. Finsterbusch J. Double-spin-echo diffusion weighting with a modified eddy current adjustment. Magn Reson Imaging. 2010;28(3):434-40.

149. Finsterbusch J. Eddy-current compensated diffusion weighting with a single refocusing RF pulse. Magn Reson Med. 2009;61(3):748-54.

150. Pajevic S, Pierpaoli C. Color schemes to represent the orientation of anisotropic tissues from diffusion tensor data: application to white matter fiber tract mapping in the human brain. Magn Reson Med. 1999;42(3):526-40.

151. Truong TK, Song AW, Chen NK. Correction for Eddy Current-Induced Echo-Shifting Effect in Partial-Fourier Diffusion Tensor Imaging. Biomed Res Int. 2015;2015:185026.

152. Haselgrove JC, Moore JR. Correction for distortion of echo-planar images used to calculate the apparent diffusion coefficient. Magn Reson Med. 1996;36(6):960-4.

153. Jones DK, Cercignani M. Twenty-five pitfalls in the analysis of diffusion MRI data. NMR Biomed. 2010;23(7):803-20.